

PHASE 2 INITIAL BOREHOLE DRILLING AND TESTING, IGNACE AREA

*WP10 – Geological Integration Report for Borehole
IG_BH03*

APM-REP-01332-0266

February 2022

Nuclear Waste Management Organization

nwmo

NUCLEAR WASTE
MANAGEMENT
ORGANIZATION

SOCIÉTÉ DE GESTION
DES DÉCHETS
NUCLÉAIRES

Nuclear Waste Management Organization

22 St. Clair Avenue East, 4th Floor

Toronto, Ontario

M4T 2S3

Canada

Tel: 416-934-9814

Web: www.nwmo.ca

**Phase 2 Initial Borehole Drilling and Testing, Ignace
Area**

**WP10 – Geological Integration Report for Borehole
IG_BH03**

APM-REP-01332-0266

December 2022

Nuclear Waste Management Organization

Document History

Title:	Phase 2 Initial Borehole Drilling and Testing, Ignace Area. WP10 – Geological Integration Report for Borehole IG_BH03		
Report Number:	APM-REP-01332-0266		
Revision:	R1	Date:	December 2022
Author Company(s):	Nuclear Waste Management Organization		
Authored by:	Aaron DesRoches, Lindsay Waffle and Andrew Parmenter (NWMO)		
Verified by:	Eric Sykes, Mostafa Khorshidi and Raymond Munier		
Accepted by:	Sarah Hirschorn (Geoscience Director)		

Revision Summary		
Revision Number	Date	Description of Changes/Improvements
R0	2022-02	Initial issue
R1	2022-12	Minor editorial revisions

ABSTRACT

Title: Phase 2 Initial Borehole Drilling and Testing, Ignace Area.
WP10 – Geological Integration Report for Borehole IG_BH03

Report No.: APM-REP-01332-0266

Author(s): Aaron DesRoches, Lindsay Waffle and Andrew Parmenter (NWMO)

Company: Nuclear Waste Management Organization

Date: December 2022

The Initial Borehole Drilling and Testing project in the Ignace Area, Ontario is part of Phase 2 Geoscientific Preliminary Field Investigations of the Nuclear Waste Management Organization's (NWMO) Adaptive Phased Management (APM) Site Selection Phase. This project involves the drilling and testing of the first of several deep boreholes within the northern portion of the Revell batholith. The second drilled borehole, IG_BH03, is located a direct distance of approximately 35 km southeast of the Wabigoon Lake Ojibway Nation and a direct distance of 42 km west of the Town of Ignace. Access to the IG_BH03 drill site is via Highway 17 and logging roads. This Geological Integration Report serves as the primary reference of the findings from the borehole drilling and testing activities at IG_BH03.

The objective of the Geological Integration Report is to summarize all findings and provide an initial interpretation of the lithological and structural characteristics of the geosphere intersected by borehole IG_BH03, including delineation of rock units and structural units. In addition, distinct intervals of higher fracture frequency identified along the length of the borehole are documented. These components represent the initial geological model for IG_BH03 which can be further used in developing a site-scale 3D geological model.

Findings and uncertainties are summarized at the end of the report. One primary consideration is the understanding that the available information *is from a single borehole*. Whether or not the characteristics of the bedrock interpreted in this report will be representative of characteristics in other boreholes remains uncertain.

TABLE OF CONTENTS

ABSTRACT	iii
1 INTRODUCTION	1
1.1 Technical Objectives and Scope of Report	1
2 Background Information	2
2.1 Geological Setting.....	2
2.2 Background and Overview of Borehole Drilling and Testing.....	5
2.2.1 Site Description	5
2.3 Borehole Construction Details for IG_BH03.....	7
2.3.1 Borehole Deviation Analysis	8
3 Integrated Geological Interpretation	10
3.1 Data Used for Geological Interpretation	11
3.1.1 Terminology	12
3.2 Geological Results	13
3.2.1 Lithological Interpretation	13
3.2.2 Alteration Interpretation	30
3.2.3 Rock Unit Classification.....	33
3.2.4 Structural Interpretation.....	37
3.2.4.1 Structures.....	40
3.2.4.2 Interpreted Fracture Sets.....	57
3.2.4.3 Fracture Infill Minerals	62
3.2.5 Structural Unit Classification.....	68
3.2.6 High Fracture Frequency Intervals (HFFI)	70
4 Summary of Findings and Uncertainties	83
4.1 Findings	83
4.2 Uncertainties	86
5 References	88
Appendix A: Summary List of Work Packages Completed for IG_BH03.....	91
Appendix B: Petrography and lithogeochemistry data	93

Appendix C:	Geophysical Near and Far Density Log Correction	99
Appendix D:	Structure log integration methodology.....	101
Appendix E:	Stereonets of Fractures by Structural Unit.....	105
Appendix F:	Stereonets of IG_BH03 High Fracture Frequency Intervals (HFFI)	108
Appendix G:	Summary of borehole logs at 1:1,000 scale.....	112

LIST OF TABLES

Table 1: Details of Casing and Coring Rods used for IG_BH03.....	7
Table 2: Details of Borehole Diameter for IG_BH03	8
Table 3: Summary of rock types encountered in IG_BH03.	13
Table 4: Summary average of major oxides in the rock types of IG_BH03. Note that only 6 rock types were sampled for lithogeochemical analysis and there are no results for pegmatite, quartz, and biotite granodiorite-tonalite dykes. Aphanitic and Feldspar-phyric tonalite dykes are combined as they are compositionally the same.....	14
Table 5: Mean geophysical response values for each logged rock type.	27
Table 6. Summary of alteration assemblages observed in IG_BH03 during geological core logging.....	31
Table 7: Summary of Classified Rock Units.....	35
Table 8: Summary of structures observed in the borehole.....	37
Table 9: Summary of interpreted fracture sets in the borehole. Presents the general description of the orientation with a mean dip and dip direction.	60
Table 10: Ranges of position along borehole and standard statistics for fracture frequencies captured within the defined structural units (SU) within the borehole.	70
Table 11. High fracture frequency intervals (HFFI)	73

LIST OF FIGURES

Figure 1: Location and Geological setting of borehole IG_BH03 in the northern portion of the Revell batholith.	3
Figure 2: Location of the drilling site for borehole IG_BH03.....	6
Figure 3. View of IG_BH03 Drill Site facing south.....	7
Figure 4: Final IG_BH03 Schematic. The final average trajectory of the borehole path is 67° from the horizontal (Golder, 2020a).	8
Figure 5. Compilation of borehole IG_BH03 deviation measurements. Data sets include up and downward televiwers surveys and gyro surveys. Average and standard deviation of survey measurements are presented. Final borehole path (easting, northing, TVD) is defined based on final gyro measurements from the Sprint-IQ survey.	9
Figure 6. a) Borehole deviation presented as the total borehole closure versus true vertical depth; and b) bullseye plot showing the planned borehole trajectory (black) compared to the final SPRINT-IQ™ survey trajectory (red).	10
Figure 7: Input datasets used to correlate geophysical log response with core logged rock types to derive final alteration and lithology logs. Key continuous geophysical logs include elements of the spectral gamma log, the natural gamma log, near and far gamma-gamma density logs, and long-spacing (LS) and short-spacing (SS) Neutron logs.	15
Figure 8: Classification/nomenclature of felsic granitoid phases according to the normalized modal mineral content (Quartz + Alkali-feldspar + Plagioclase = 100 Vol%) as determined	

- from investigation of 15 samples taken for lithogeochemical analysis. Average modal mineralogy for each sample was determined semi-quantitatively using polished thin sections and plotted on a simplified ternary Streckeisen diagram after Le Bas and Streckeisen (1991)..... 16
- Figure 9: Plutonic Rock Classification (Debon and Le Fort, 1983). Diagram axes correspond to proportions of K-feldspar and plagioclase to quartz. P is calculated from $(K-(Na+Ca))$ and Q is calculated from $((Si/3) - (K+Na+(2*Ca)/3))$. Parameters calculated as oxide percentages converted to millications. Crosses show the mean composition for each rock type..... 17
- Figure 10: Representative examples of biotite granodiorite-tonalite (sample IG_BH03_LG020). a) Hand-sample photograph. b) Billet photograph showing yellow staining of potassium feldspars (billet size is 25 x 40 mm; large A and B are differentiating different grain size domains in the sample). c) Thin section photomicrograph with rock-forming minerals plagioclase (pl) and quartz (qz). Sericite (white mica) alteration can be seen in cores of plagioclase crystals. Minor biotite is present (dark greenish/brown mineral); crossed polarizers transmitted light..... 18
- Figure 11: Representative examples of amphibolite (sample IG_BH03_LG010). a) Hand-sample photograph. b) Billet photograph (billet size is 25 x 40 mm). c) Thin section photomicrograph with main rock-forming minerals amphibole (am; tremolite-actinolite), biotite (bt) and epidote (ep); plane polarized transmitted light..... 20
- Figure 12: Representative examples of feldspar-phyric tonalite dyke (sample IG_BH03_LG005). a) Hand-sample photograph. b) Billet photograph showing yellow staining of alkali feldspar (billet size is 25 x 40 mm). c) Thin section photomicrograph with plagioclase (pl) phenocrysts, in a very fine-grained matrix of quartz (qz), plagioclase (pl), and biotite (bt); crossed polarized transmitted light..... 22
- Figure 13: Representative examples of an aplite dyke (sample IG_BH03_LG007). a) Hand-sample photograph. b) Billet photograph showing yellow staining of alkali feldspar (billet size is 25 x 40 mm). c) Thin section photomicrograph with rock-forming minerals plagioclase (pl), alkali feldspar (af) and quartz (qz); crossed polarized transmitted light. .. 23
- Figure 14: A leucogranite dyke from 735 m along borehole (sample IG_BH03_LG015). a) Hand-sample photograph. b) Billet photograph showing yellow staining of alkali feldspar (billet size is 25 x 40 mm). c) Thin section photomicrograph with rock-forming minerals plagioclase (pl), alkali feldspar (af) and quartz (qz); crossed polarized transmitted light. .. 25
- Figure 15: Chondrite-normalized rare-earth element (REE) plot (after Taylor and McLennan, 1985) of rock types from IG_BH03 and a representative average of 2.8 Ga low-heavy REE (HREE) tonalite-trondhjemite-granodiorite (TTG) from the Fennoscandian shield (black squares; Halla, 2018). Y-axis shows concentrations (expressed as logarithm to the base 10 of the value) of REE (x-axis, by atomic number) in IG_BH03 samples normalized to a reference Chondrite standard. REE patterns of biotite granodiorite-tonalite, aphanitic tonalite dykes, and feldspar-phyric tonalite dykes demonstrate steep fractionation and significant depletion of HREE. Aplite and granite dykes demonstrate a less steep fractionation and significant europium anomalies, suggesting they are from a later stage, evolved granite source..... 26
- Figure 16: Violin plots show the distribution of geophysical log responses associated with the logged rock types. Each violin shows the distribution of the data values with the median (thick dashed line), and quartiles (thin dashed lines) marked. Rock types are ordered based on total data counts from left to right in each graph..... 29

- Figure 17: Distribution of Neutron and Density Values of all Rock Types encountered in IG_BH03. Colored points represent mean values of the geophysical response and the error bars represent standard deviation..... 30
- Figure 18: Common alteration assemblages logged in IG_BH03. a) Sample IG_BH03_LG017, biotite granodiorite-tonalite logged with potassic and hematite alteration. b) Photomicrograph of sample IG_BH03_LG017 showing plagioclase crystals (pl) heavily altered by white mica and epidote, biotite (bt) weakly altered by chlorite and iron oxide, and quartz (qz); crossed-polarized transmitted light. c) Sample IG_BH03_LG006, biotite granodiorite-tonalite logged as silicified. d) Sample IG_BH03_LG006 showing quartz grains (qz), alkali feldspar (af), plagioclase (pl) with white mica (wm) altered plagioclase and filling interstitial space; crossed-polarized transmitted light. e) Sample IG_BH03_LG019, biotite granodiorite-tonalite logged as bleached. f) Sample IG_BH03_LG019 showing plagioclase (pl) moderately altered by white mica, and quartz grains; crossed-polarized transmitted light. g) Hematite and chlorite alteration coating a fracture at a contact between biotite granodiorite-tonalite and amphibolite at 773.83 m. These alteration styles are commonly found at amphibolite contacts. h) Sample IG_BH03_LG017 showing the association of biotite (bt), chlorite (ch), and iron oxide (interpreted as hematite (he)); crossed-polarized transmitted light. *Note this is not from the same interval as the hand sample in (g) but demonstrates the relationship commonly seen in thin section..... 32
- Figure 19: Alteration types and distribution along the borehole based on geological core logging and analysis of the optical televiewer log resulting in a final alteration log. A2 indicates intervals with slight alteration and A3 indicates intervals with moderate alteration. 33
- Figure 20: Summary of final logged rock type, alteration and key geophysical logs presented alongside interpreted rock units for IG_BH03..... 36
- Figure 21: Equal Area Lower Hemisphere Projections (stereonet) showing poles to planar structural measurements, unweighted (n = 2088). 38
- Figure 22: Equal Area Lower Hemisphere Projections (stereonet) showing density contours of the poles to all planar structural measurements. Top: all data – contours, unweighted (n = 2088). Bottom: all data – contours, Terzaghi-weighted. 39
- Figure 23: Stereonet showing poles to the planes of Primary Igneous Structures (IPS; n = 24).40
- Figure 24: Stereonet showing poles and unweighted contours for all geological contacts (n = 59). 41
- Figure 25: Stereonet showing poles to oriented amphibolite contacts (n = 22). Open symbols identify broken contacts (CO-BR) and filled symbols identify partially intact/intact contacts (CO-PIN/IN)..... 42
- Figure 26: Stereonet showing the distribution of poles to the contacts of logged felsic dykes (n = 38), including, aphanitic tonalite dykes (n= 6), aplite dykes (n = 8), biotite granodiorite-tonalite dykes (n = 4), feldspar-phyric tonalite dykes (n = 14), granite dykes (n = 4), and pegmatite dykes (n = 2). 43
- Figure 27: Examples of primary igneous and ductile structure in IG_BH03: a) A change in biotite concentration interpreted as primary igneous layering in biotite granodiorite-tonalite (158 m along borehole). b) Muscovite and biotite-defined foliation trending at a moderate angle to the core axis, parallel to the white dashed line, in a small interval of biotite granodiorite-tonalite between two amphibolites (548 m along borehole). c) Shear zone developed at a moderate angle to the core axis within and along the margin of amphibolite at its contact with biotite granodiorite-tonalite (553 m along borehole)..... 44

- Figure 28: Summary log showing the frequency per metre of brittle structures (left) in comparison to stick plots that show the distribution of all brittle structures (Joints – JN, Veins – VN and Faults - FLT) and all ductile structures (Shear Zones – SHR + SHRD and Foliation – FO)..... 45
- Figure 29: Stereonets showing orientation information for Foliation (FO). Top: All data – poles and contours, unweighted (n = 33). Filled symbols identify partially intact/intact Foliation (FO-PIN/IN). Bottom: All Foliation data, Terzaghi-weighted contours (n = 54). 46
- Figure 30: Stereonets showing orientation information for Shear Zones (SHR). Top: All data – poles and contours, unweighted (n = 95). Open symbols identify broken Shear Zones (SHR-BR) and filled symbols identify partially intact/intact Shear Zones (SHR-PIN/IN). Bottom: All Shear Zone data, Terzaghi-weighted contours (n = 149). 48
- Figure 31: Examples of brittle structures observed in IG_BH03: A) A broken, clean, hairline (no visible geological aperture) joint in biotite granodiorite-tonalite (403 m). B) A broken joint with soft gouge-like infill and a geological aperture of 17 mm in amphibolite (547 m). C) A broken, mm-scale quartz vein in biotite granodiorite-tonalite (460 m). D) An intact, mm-scale epidote vein in biotite granodiorite-tonalite with associated alteration (883 m). E) A broken fault with 2 mm geological aperture and an associated cm-scale halo of sericitization in biotite granodiorite-tonalite (375 m). F) A lineation defined by aligned quartz (parallel to white arrow) on broken fault plane in biotite granodiorite-tonalite (83.5 m). 49
- Figure 32: Stereonets showing orientation information for Joints (JN). Top: All data – poles and contours, unweighted (n = 1388). Open symbols identify broken Joints (JN-BR) and filled symbols identify partially intact/intact Joints (JN-PIN/IN). Bottom: All Joint data, Terzaghi-weighted contours (n = 3091). 51
- Figure 33: Stereonets showing orientation information for all Veins (VN). Top: All data – poles and contours, unweighted (n = 398). Open symbols identify broken Veins (VN-BR) and filled symbols identify partially intact/intact Veins (VN-PIN/IN). Bottom: All Vein data, Terzaghi-weighted contours (n = 840). 52
- Figure 34: Stereonets showing orientation information for Faults (FLT). Top: All data – poles (n = 90). Bottom: All Fault data, Terzaghi-weighted contours (n = 174)..... 54
- Figure 35: Stereonets showing orientation information for all Lineations. Top: All lineations (n = 93) plotted by associated plane type (Fault – FLT, Foliation – FO, Shear – SHR). Bottom: Poles to all oriented planes with identified lineations (n = 93). 55
- Figure 36: Stereonet plot showing poles to all fracture planes logged as broken (n = 226), with unweighted contours..... 56
- Figure 37: Stereonet plot showing poles to all fracture planes logged as intact or partially intact (n = 1650), with unweighted contours. 57
- Figure 38: Stereonets of all oriented fractures, including all joints, veins and faults. Top: All fractures – poles, unweighted (n = 1876). Identified pole clusters are colour-coded by initial fracture set designation. Middle: All fractures – contours (n = 1876), unweighted. Bottom: All fractures – contours, Terzaghi-weighted (n = 4105). Middle and bottom stereonet are overlain by final fracture set interpretation. See text and Table 9 for additional summary. 59
- Figure 39: Summary log showing the frequency per metre of all brittle structures (left) in comparison to stick plots that show the distribution of all fractures assigned to defined fracture sets 1, 2, 3a/3b, 4a/4b, 5a/5b and 6, as well as unassigned random fractures..... 61

- Figure 40: Summary log showing the frequency per metre of all brittle structures (left) in comparison to stick plots that show the distribution of the most common infill mineral phases including quartz (Qz), chlorite (Chl), iron oxide stain (Fe), epidote (Ep), calcite (Ca), a granitic (Gt) assemblage that includes some combination of alkali-feldspar (Afs) with quartz, plagioclase and biotite, and, fractures that exhibit either clay (Cl), broken rock (Br), soft clay gouge (Go_So) or stiff clay gouge (Go_St). 62
- Figure 41: Stereonet plot showing poles to all fracture planes logged with quartz (n = 1181) +/- chlorite, calcite, epidote, biotite, phlogopite, muscovite, iron oxide stain and/or pyrite..... 63
- Figure 42: Stereonet plot showing poles to all fracture planes logged with chlorite (n = 253).... 63
- Figure 43: Stereonet plot showing poles to all fracture planes logged with calcite (n = 233). 64
- Figure 44: Stereonet plot showing poles to all fracture planes logged with epidote (n = 209). .. 65
- Figure 45: Stereonet plot showing poles to all fracture planes logged with iron oxide stain (n = 156). 65
- Figure 46: Stereonet plot showing poles to all fracture planes logged with clay, broken rock, or hard or soft gouge (n = 47). 66
- Figure 47: Stereonet plot showing poles to all fracture planes logged with granitic infill (n = 43), including alkali-feldspar +/- quartz, plagioclase and biotite..... 67
- Figure 48: Stereonet showing poles to all fractures logged as having no identifiable mineral infill phase (n = 230). Fractures logged in 'viewer' datasets only, geological 'core' logging only, or identified in 'both' datasets, are distinguished. 68
- Figure 49: Fracture frequency histogram (left) and cumulative fracture frequency curve (right) showing vertical distribution of all logged joints, faults, and veins along the borehole. The cumulative fracture frequency curve shows the changes in slope where boundaries in structural units (SU) are defined. Structural units and their top and bottom positions along borehole are labelled on the figure..... 69
- Figure 50. High fracture frequency intervals (HFFI) interpretation based on fracture intensity from borehole fracture frequency log. Five high fracture frequency intervals are outlined by their yellow bands. The red dashed line represents the peak location..... 71
- Figure 51. Terzaghi-weighted stereonet plot of fractures (JN, VN, FLT) within high fracture frequency interval 1 (HFFI_1) from 142.3 – 157.7 m. Two peaks are defined, a major peak with a mean orientation of 145/52 (best fit plane shown as black dashed great circle) and a minor peak with a mean orientation of 292/19 (best fit plane shown as grey dashed great circle; DipDirection/Dip convention). 74
- Figure 52. Core from an interval of HFFI_1 (143.69 – 155.0 m). Biotite granodiorite-tonalite above and below the amphibolite unit is characterized by well spaced, fairly shallow-dipping fractures. Fracture intensity increases around and within the amphibolite, including a fault logged with stiff gouge infill at 148.75 m. Intersections of shallow and steeply dipping fractures create intervals of broken core. 75
- Figure 53. Core from an interval of HFFI_2 (401.59 – 413.14 m). Biotite granodiorite-tonalite with moderate to strong silicification associated with well-spaced, steeply dipping fractures. 76
- Figure 54. Core from an interval of HFFI_3 (483.62 – 495.25 m). Biotite granodiorite-tonalite with moderately pervasive potassic alteration logged. An aphanitic tonalite dyke with steeply dipping contacts is visible at 489.91 m and is not associated with an increase in fracture frequency..... 77

- Figure 55. Core from an interval of HFFI_4 (765.86 – 777.08 m). There is a feldspar-phyric dyke at the top of the zone and then biotite granodiorite-tonalite, with increasing alteration and fracture intensity approaching the amphibolite units starting at 773.65 m. 78
- Figure 56. Core from HFFI_5 (a: 859.1 – 870.19 m; b: 870.19 – 881.51 m). Biotite granodiorite-tonalite at the top of the interval with well-spaced fractures. Increasing fracture and alteration (silicification) intensity approaching the top contact of a feldspar-phyric tonalite dyke at 869.76 m (bottom of a). Increased alteration and fracture intensity continue through to ca. 875 m (b) where the biotite granodiorite-tonalite is less altered and fracture intensity decreases to the bottom of the interval. 79
- Figure 57: Lineament traces near IG_BH03 interpreted from LiDAR DEM and airborne geophysics data (DesRoches et al., 2018). Lineament traces are dominated by short length NE trending structures and fewer long NW trending structures. 81
- Figure 58: Rose diagram of the lineaments (N = 76) around IG_BH03 (see Figure 57) interpreted from LiDAR DEM and airborne geophysics data (DesRoches et al., 2018). Lineament orientations are plotted using a bin size of 5 degrees. 82
- Figure 59. Rose diagrams of the borehole logged fracture orientations using a minimum dip angle of 45 degrees, and bin size of 5 degrees. Left: Unweighted (N = 1342). Right: Terzaghi-weighted to account for directional bias of the borehole path (weighted N = 2701). 82
- Figure 60: Summary log presenting final logged rock type, classification of rock units, fracture frequency per metre, and structural units. Data is plotted as position along borehole and elevation. This log represents the 1-dimensional geological model for IG_BH03. 84

1 INTRODUCTION

The Initial Borehole Drilling and Testing project in the Ignace Area, Ontario is part of Phase 2 Geoscientific Preliminary Field Investigations of the Nuclear Waste Management Organization's (NWMO) Adaptive Phased Management (APM) Site Selection Phase.

Following the first stage of the Phase 2 Initial Field Studies summarized by Golder (2015) and in consultation with the community, an area located in the northern portion of the Revell batholith was selected by the NWMO for further investigation through an initial borehole drilling campaign which involves the drilling and testing of several deep boreholes.

Borehole IG_BH03 is located a direct distance of approximately 35 km southeast of the Wabigoon Lake Ojibway Nation and a direct distance of 42 km west of the Town of Ignace. Access to the IG_BH03 drill site is via Highway 17 and primary logging roads (Figure 1 and Figure 2). This single borehole integration report serves as the primary reference of the geological findings from the borehole drilling and testing activities at IG_BH03.

The project fieldwork was carried out by a team led by Golder Associates Ltd. (Golder) on behalf of the NWMO. The overall program, described in the Initial Borehole Characterization Plan (Golder, 2017) includes activities divided into work packages related to: the mobilization and set up of the borehole drilling site, the recovery and logging of the bedrock core, drilling water management and groundwater sampling, borehole geophysical and hydraulic testing, and laboratory testing. All activities are documented in work package data reports that describe test methods, collected data, and calculations, where applicable. The full list of work packages and associated data reports is included in Appendix A.

This report, which represents the tenth work package (WP10 Integration and Synthesis), presents an integrated summary of geological and geophysical information collected primarily during the completion of three work packages, including:

- **WP02 Borehole Drilling and Coring:** Borehole deviation surveys and borehole construction details.
- **WP03 Geological and Geotechnical Core Logging, Photography and Sampling:** Borehole core logging, including lithological, structural, and alteration characteristics, preserved core samples for laboratory testing, and core photographs.
- **WP05 Geophysical Well Logging and Interpretation:** Continuous geophysical logs, including Caliper, Fluid Temperature/Resistivity, Flowing Fluid Electrical Conductivity (FFEC), Acoustic Televiwer, Optical Televiwer, Natural Gamma, Electromagnetic Induction (Apparent Conductivity), Magnetic Susceptibility, Neutron, Gamma-Gamma Density, Full Waveform Sonic, Resistivity/Spontaneous Potential/Single Point Resistance, Heat Pulse Flow Meter, Spectral Gamma and Borehole Deviation.

1.1 Technical Objectives and Scope of Report

The objective of this Single Borehole Data Integration report is to summarize all geological findings that aid in providing an initial interpretation of the lithological and structural characteristics of the geosphere intersected by borehole IG_BH03. This initial interpretation will be revised as further boreholes are drilled to form a holistic interpretation for the geosphere.

Additional information related to developing an understanding of the petrophysical and transport properties of the bedrock of the Revell batholith, as well as the geomechanical, hydrogeological, geochemical, and thermal properties will be reported on separately in a Descriptive Geosphere Site Model (DGSM) report. The DGSM report will summarize the additional borehole- and laboratory-derived data related to all of these additional topics listed above. The DGSM report will present this information along with a geological model that integrates the WP10 results for all drilled boreholes.

The information presented in this report, which focuses on IG_BH03, represents the first step in this integration process.

The scope of this Single Borehole Data Integration report is summarized in the following sections:

- Section 1 provides the report introduction and includes the summary of technical objectives and scope of the sections in the report.
- Section 2 first briefly describes the geological setting for the area around the borehole location and then provides an overview of the borehole drilling and testing activity. This includes a brief site description, a summary of the borehole construction, and deviation surveys of the borehole.
- Section 3 presents the integrated summaries of the lithological, alteration, and structural characteristics of the bedrock intersected by the borehole, including interpretation of fracture zones (Sections 3.2 and 3.3). Using this information, an initial geological model with interpretation of rock units and structural units for the borehole is presented.
- Section 4 summarizes findings and addresses uncertainties.
- Appendix A lists all Work Packages and Work Package report names produced as part of the full suite of activities associated with IG_BH03.
- Appendix B presents the petrographic, modal mineralogy, and lithogeochemical data, which are summarized in Section 3.
- Appendix C presents a table of values summarizing the correction applied to the geophysical near and far density log.
- Appendix D contains the methodology for integrating the un-oriented structural dataset generated during WP03 with the televiewer geophysical logs collected during WP05 to produce a final log of oriented structures. The integrated structural dataset is presented in Section 3.
- Appendix E presents lower hemisphere equal area projections (stereonet) summarizing the brittle fractures for each structural unit (SU) in the borehole, defined in Section 3.2.5.
- Appendix F presents lower hemisphere equal area projections (stereonet) summarizing the structural orientation information for all high fracture frequency intervals (HFFI) in the borehole, defined in Section 3.2.6.
- Appendix G presents a summary of the borehole logs for IG_BH03 at 1:1,000 scale.

2 BACKGROUND INFORMATION

2.1 Geological Setting

The approximately 2.7-billion-year-old Revell batholith is located in the western part of the Wabigoon Subprovince of the Archean Superior Province. The batholith is roughly elliptical in shape trending northwest, is approximately 40 km in length, 15 km in width, and covers an area of approximately 455 km². Based on initial geophysical modelling, the batholith is approximately 2 km to 3 km thick through the center of the northern portion (SGL, 2015). The batholith is surrounded by supracrustal rocks of the Raleigh Lake (to the north and east) and Bending Lake (to the southwest) greenstone belts (Figure 1).

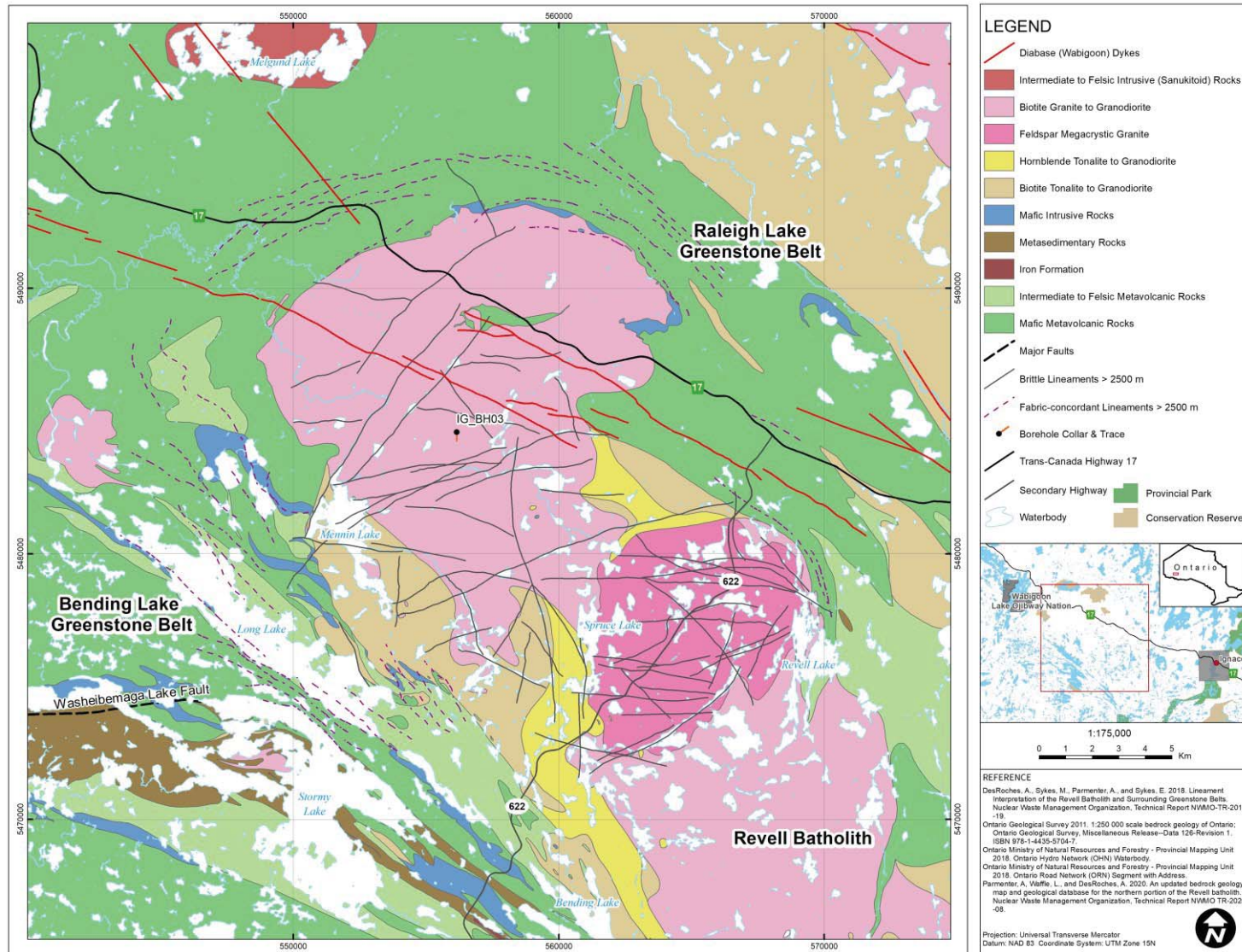


Figure 1: Location and Geological setting of borehole IG_BH03 in the northern portion of the Revell batholith.

Four main rock units are identified in the supracrustal rock group: mafic metavolcanic rocks, intermediate to felsic metavolcanic rocks, metasedimentary rocks, and mafic intrusive rocks (Figure 1). Sedimentation within the supracrustal rock assemblage was largely synvolcanic, although sediment deposition in the Bending Lake area may have continued past the volcanic period (Stone, 2009; Stone, 2010a; Stone, 2010b). All supracrustal rocks are affected, to varying degrees, by penetrative brittle-ductile to ductile deformation under greenschist- to amphibolite-facies metamorphic conditions (Blackburn and Hinz, 1996; Stone et al., 1998). In some locations, primary features, such as pillow basalt or bedding in sedimentary rock units is preserved, in other locations, primary relationships are completely masked by penetrative deformation. Uranium-lead (U-Pb) geochronological analysis of the supracrustal rocks produced ages that range between 2734.6 +/- 1.1 Ma and 2725 +/- 5 Ma (Stone et al. 2010).

Three main suites of plutonic rock are recognized in the Revell batholith (Figure 1), including, from oldest to youngest: a Biotite Tonalite to Granodiorite suite, a Hornblende Tonalite to Granodiorite suite, and a Biotite Granite to Granodiorite suite. Plutonic rocks of the Biotite Tonalite to Granodiorite suite occur along the southwestern and northeastern margins of the Revell batholith. The principal type of rock within this suite is a white to grey, medium-grained, variably massive to foliated or weakly gneissic, biotite tonalite to granodiorite. One sample of foliated and medium-grained biotite tonalite produced a U-Pb age of 2734.2 +/- 0.8 Ma (Stone et al., 2010). The Hornblende Tonalite to Granodiorite suite occurs in two irregularly shaped zones surrounding the central core of the Revell batholith. Rocks of the Hornblende Tonalite to Granodiorite suite range compositionally from tonalite through granodiorite to granite and also include significant proportions of quartz diorite and quartz monzodiorite. One sample of coarse-grained grey mesocratic hornblende tonalite produced a U-Pb age of 2732.3 +/- 0.8 Ma (Stone et al., 2010). Rocks of the Biotite Granite to Granodiorite suite underlie most of the northern, central and southern portions of the Revell batholith. Rocks of this suite are typically coarse-grained, massive to weakly foliated, and white to pink in colour. The Biotite Granite to Granodiorite suite ranges compositionally from granite through granodiorite to tonalite. This suite includes the oval-shaped potassium-feldspar megacrystic granite body in the central portion of the Revell batholith. One sample of coarse-grained, pink, massive potassium feldspar megacrystic biotite granite produced a U-Pb age of 2694.0 +/- 0.9 Ma (Stone et al., 2010).

Borehole IG_BH03 is located in the northern portion of the Revell batholith (Figure 1). Bedrock exposure within and around this part of the batholith is generally very good due to minimal overburden, few water bodies, and relatively recent forestry activities. The bedrock surrounding IG_BH03 is composed mainly of massive to weakly foliated felsic intrusive rocks that vary in composition between granodiorite and tonalite. Bedrock identified as tonalite transitions gradationally into granodiorite and no distinct contact relationships between these two rock types are typically observed (SRK and Golder, 2015; Golder and PGW, 2017). Massive to weakly foliated granite is identified at the ground surface to the southeast of the investigation area. The granite is observed to intrude into the granodiorite-tonalite bedrock, indicating that it is a distinct, younger, intrusion (Golder and PGW, 2017).

A west-northwest trending mafic dyke interpreted from aeromagnetic data and observed during detailed mapping to be approximately 15-20 m wide, extends across the northern portion of the Revell batholith (Figure 1; Golder and PGW, 2017). This dyke is associated with several other similarly orientated mafic dykes that stretch across the northern portion of the Revell batholith and into the surrounding greenstone belts. All of these mafic dykes have a similar character and are interpreted to be part of the Wabigoon dyke swarm. One sample from the same Wabigoon swarm produced a U-Pb age of 1887 +/- 13 Ma (Stone et al., 2010), indicating that these mafic dykes are Proterozoic in age. It is assumed based on surface measurements that these mafic dykes are sub-vertical (Golder and PGW, 2017).

Long, narrow valleys are located along the western and southern limits of the area of investigation (Figure 2). These local valleys host creeks and small lakes that drain to the southwest and may represent the surface expression of structural features that extend into the bedrock. A broad valley is located along the eastern limits of the area of investigation and hosts a more continuous, unnamed water body that flows to the south. The linear and segmented nature of this waterbody's shorelines may also represent the surface expression of structural features that extend into the bedrock (DesRoches et al., 2018).

Regional observations from mapping have indicated that structural features are widely spaced (typical 30 to 500 cm spacing range) and dominantly comprised of sub-vertical joints with two dominant orientations, northeast and northwest trending (SRK and Golder, 2015; Golder and PGW, 2017). Interpreted bedrock lineaments generally follow these same dominant orientations in the northern portion of the Revell batholith (DesRoches et al., 2018). Minor subhorizontal joints have been observed with minimal alteration, suggesting they are younger and perhaps related to glacial unloading. One mapped regional-scale fault, the Washeibemaga Lake fault, trends east and is located to the west of the Revell batholith (Figure 1). Additional details of the lithological units and structures found at surface in the northern portion of the Revell batholith are provided in Golder and PGW (2017).

2.2 Background and Overview of Borehole Drilling and Testing

2.2.1 Site Description

The drilling site for borehole IG_BH03 is located approximately 35 km southeast of the Wabigoon Lake Ojibway Nation and 42 km west of the Town of Ignace. Access to the IG_BH03 drill site is via Highway 17 and a network of logging roads. Access to the site was established by clearing approximately 1.15 km of new road branching off of Dyment road towards the south (Figure 2). The drilling site is approximately 70 m by 50 m and has an area of 3,500 m² (Figure 3). The borehole is located at the southern end of the drilling site. The drilling site was constructed to minimize the need for ground clearing and reduce the effects of erosion from water runoff. A large percentage of the site was rock outcrop, and a compacted aggregate pad was constructed to level off the area. An oblique aerial view of the site looking south is shown in Figure 3.

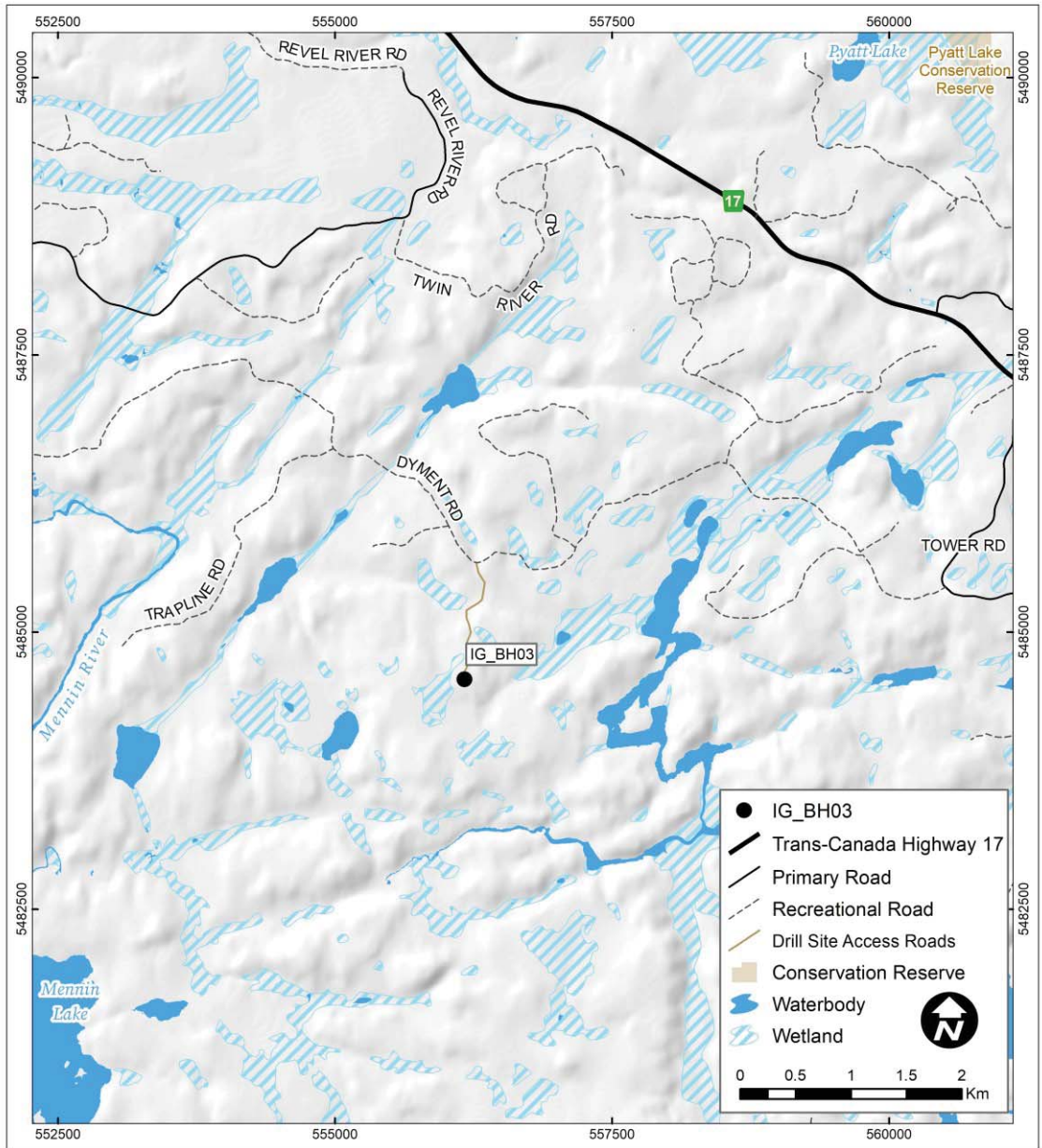


Figure 2: Location of the drilling site for borehole IG_BH03.



Figure 3. View of IG_BH03 Drill Site facing south.

2.3 Borehole Construction Details for IG_BH03

Borehole IG_BH03 was drilled at an inclination of -70° towards an azimuth of 180° using a diamond drill. Two sets of casing were installed in the upper parts of the borehole to ensure borehole stability and reduce mixing of shallow and deep groundwaters. The borehole construction is shown in the borehole schematic (Figure 4). The down-axis position along the borehole is measured in metres from surface.

PWT conductor casing was installed and cemented to a position of 5.81 m (along hole), to prevent drill fluid from escaping through the fractured upper bedrock. In particular, this casing isolates the upper 1.21 m of the borehole, comprising overburden material overlying the bedrock. The borehole was drilled to 102.12 m along borehole and evaluated to determine a location to install the PQ casing. The borehole was reamed, and PQ casing was installed to a desired length of 71 m.

The PQ casing was cemented in place using a high sulphate resistant cement (LaFarge) and the cement was left to cure for 48 hours. Drilling and coring activities resumed for the remainder of the borehole down to a drilled extent, along the borehole axis, of 1000.54 m. The final IG_BH03 casing diameters and positions, borehole and core diameters are shown in Table 1 and Table 2.

Table 1: Details of Casing and Coring Rods used for IG_BH03.

Casing Type	Outer Diameter (mm)	Inner Diameter (mm)	Position (m)
Conductor (PWT) Casing	139.7	127.0	5.81
Surface (PQ) Casing	114.3	101.6	71.0
HQ3 Drill Bit	96.0 ¹	61.1 ²	N/A

¹Open borehole diameter. ²HQ3 core diameter size.

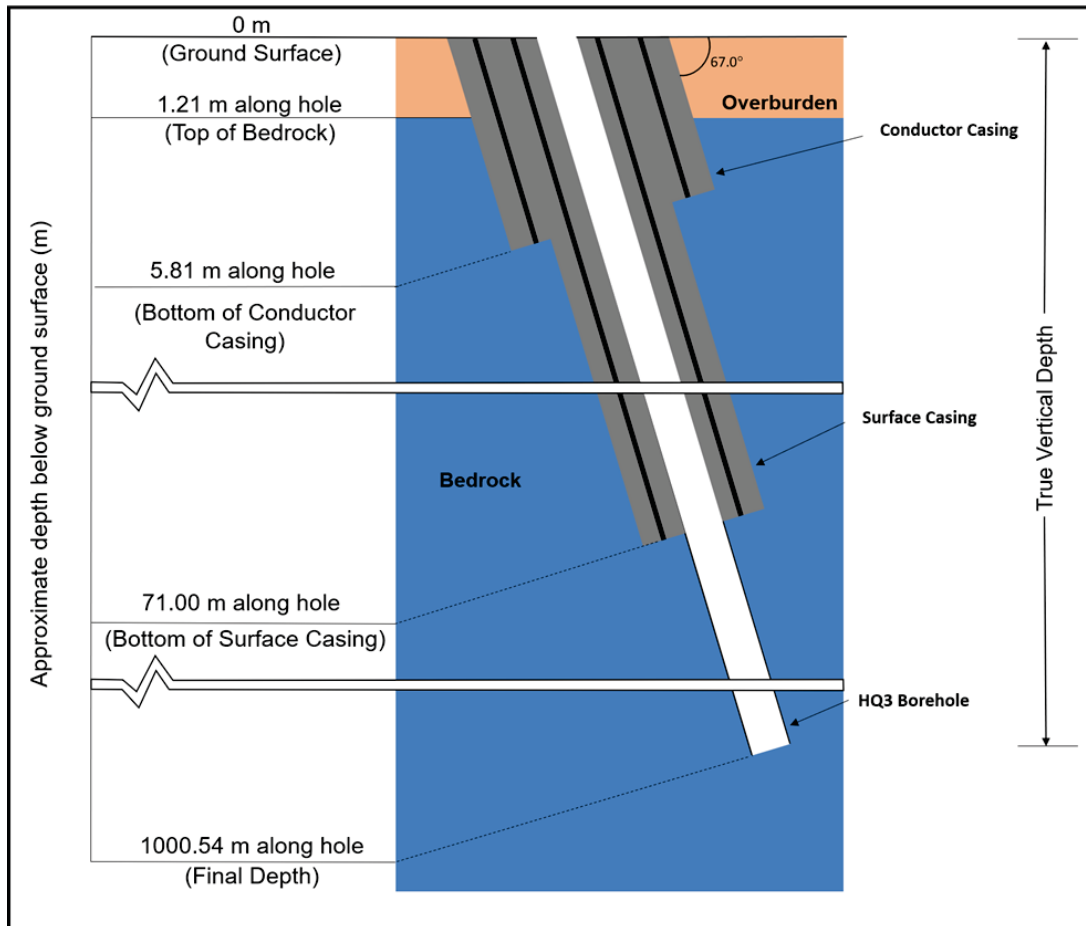


Figure 4: Final IG_BH03 Schematic. The final average trajectory of the borehole path is 67° from the horizontal (Golder, 2020a).

Table 2: Details of Borehole Diameter for IG_BH03

Position from (m)	Position to (m)	Diameter Type	Borehole Diameter (mm)
0	5.81	Conductor (PWT) Casing and Surface (PQ) Casing	143.76
5.81	71	Surface (PQ) Casing	121.0
71	1000.54	Open Borehole (HQ size)	96

2.3.1 Borehole Deviation Analysis

Borehole IG_BH03 was planned to be drilled with an inclination of -70° (equivalent tilt is 70°) towards an azimuth of 180°. No deviations corrections were made during drilling. Two downhole deviation surveys were conducted; one at 50 m intervals (downhole – multiple probe trips) to monitor deviation during drilling using the Reflex TrueShot probe, and the other at 10 m intervals at the end of drilling using the Reflex Sprint-IQ gyro (up hole – single trip; Golder, 2020a).

During the geophysical logging, four additional borehole deviation logs were continuously recorded using the onboard 3-axis magnetometer and accelerometers within the acoustic and optical

televiwer probes (Figure 5). These surveys provided continuous inclination and declination data at ~2 mm intervals (Golder, 2020b). Due to the steel casing, the majority of the televiwer surveys were terminated at the base of the casing and are missing data from the first 71 m. Therefore, a single televiwer survey conducted prior to installing the casing was used for this section of the borehole. Data from these surveys were mainly used to confirm and support the results of the final deviation survey using the Sprint-IQ probe. Figure 5 presents individual azimuth and tilt profiles plotted from each televiwer run and the Sprint-IQ gyro run. The standard deviation for the azimuth and tilt profiles is calculated between each of the profiles to show the variability amongst the different profile runs. The upper ~71 m of the borehole presents reduced variability between measurements because the gyro is only compared to the single televiwer run (run prior to installing casing). The mean profiles for the televiwer runs are calculated and compared to interpolated profiles derived from the Sprint-IQ gyro measurements at 10 metre increments. Although the gyro survey is used for the final borehole deviation, the televiwer surveys provided an estimate of the magnitude of variability between different runs, as well as an average for comparison with the gyro survey. Overall, the standard deviation for the azimuth and tilt is shown to be less than 2 degrees and 0.5 degrees, respectively.

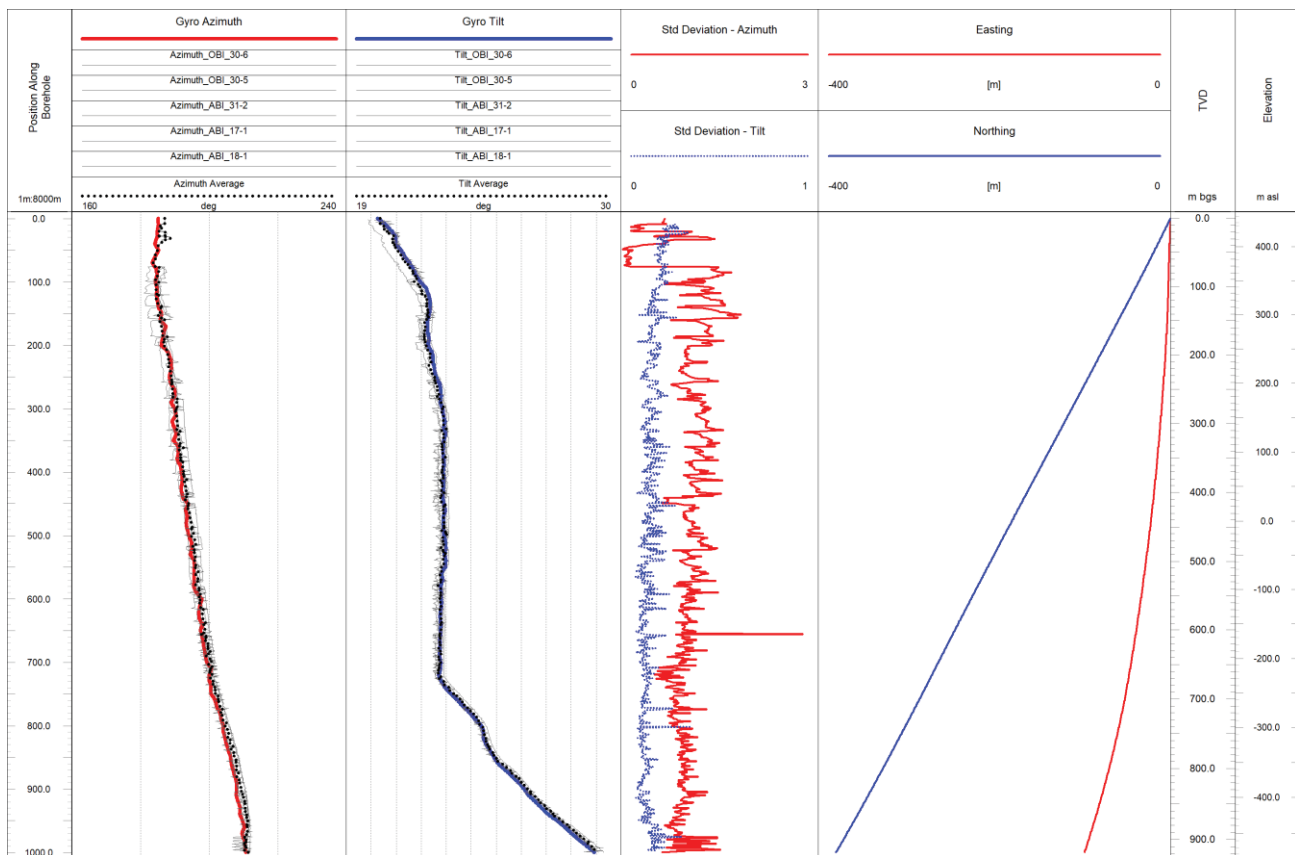


Figure 5. Compilation of borehole IG_BH03 deviation measurements. Data sets include up and downward televiwers surveys and gyro surveys. Average and standard deviation of survey measurements are presented. Final borehole path (easting, northing, TVD) is defined based on final gyro measurements from the Sprint-IQ survey.

By comparing manufacturer specifications between the Reflex Sprint-IQ Gyro and the two televiwer probes, the Sprint-IQ gyro is considered more accurate. Additionally, data recorded using the Sprint-IQ was performed in stationary mode, compared to the continuous mode of the televiwer probes. Despite the differences between the probes, the results indicated there is strong

consistency between the average of the televiewers azimuth and tilt profiles and the Sprint-IQ survey data.

As a result, borehole positioning was calculated using the Sprint-IQ gyro survey data based on the Minimum Curvature Method, which based on API (1985) yields the most accurate location. The three components of the location along the borehole (easting, northing, and the true vertical depth (TVD)) were calculated for the Sprint-IQ survey (10 m stations) and presented in Figure 5 and Figure 6. The borehole collar is located at Easting and Northing coordinates of 556,171.46 m and 5,484,534.33 m, respectively, using the local UTM coordinate system (NAD83 UTM Z15N). The elevation of 441.56 masl (metres above sea level) represents the ground surface based on the CGVD2013 vertical datum. The final true vertical depth of the borehole, calculated using the measured actual orientation of the borehole, is 918.29 mbgs (Golder, 2020a). Figure 6 shows the borehole deviating 106.5 m to the West and 40.6 m to the South from the planned end location.

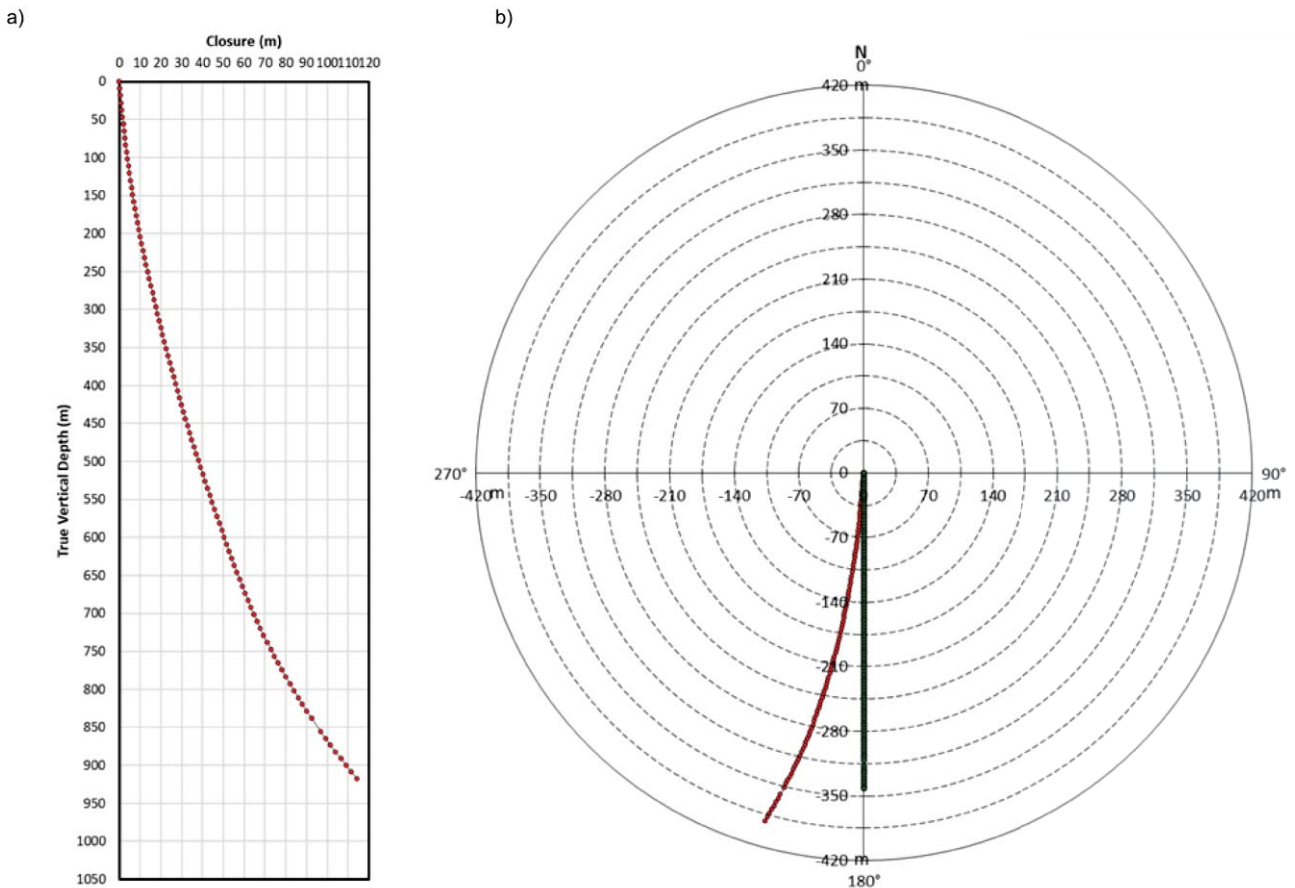


Figure 6. a) Borehole deviation presented as the total borehole closure versus true vertical depth; and b) bullseye plot showing the planned borehole trajectory (black) compared to the final SPRINT-IQ™ survey trajectory (red).

3 INTEGRATED GEOLOGICAL INTERPRETATION

The following section presents an integrated geological interpretation for IG_BH03 using the data collected during both geological core (WP03) and geophysical (WP05) logging activities, as well as

applicable data from the laboratory analyses of core samples. The data sources and terminology used in order to develop the geological interpretation presented herein are described first in Section 3.1. The lithological interpretation, including final lithology and alteration logs is presented in Sections 3.2.1 and 3.2.2, respectively, resulting in the development of an integrated rock unit model described in Section 3.2.3. A structural interpretation is presented in Section 3.2.4, resulting in a structural unit model, described in Section 3.2.5, and a description of identified high fracture frequency intervals in Section 3.2.6.

3.1 Data Used for Geological Interpretation

The bedrock lithological, alteration, and structural features were logged continuously over a total borehole length of 1000.54 m (999.33 m recovered core; Golder, 2020c). This initial analysis was largely based on visual inspection of the core to describe the unique rock and alteration types and associated characteristics including texture, fabric, and grain size. Variations in bedrock radiometric components were evaluated with the use of a handheld gamma-ray spectrometer to help distinguish between the various felsic granitoid phases encountered. The spot analysis was performed once per three metre core run if there was no lithological variation.

Structural features in the borehole were initially collected by geological core logging to evaluate unique structure types, mineral infillings, and other associated characteristics. Orientations of the logged structures were initially measured relative to an arbitrary reference line drawn along the length of the core axis.

Following completion of the drilling and logging activities, continuous borehole geophysical logs were acquired and the results from some of these logs were used to enhance the analysis of lithology, alteration and structure (Golder, 2020b). The arbitrary orientations of logged structures were corrected through analysis of the continuous downhole optical and acoustic televiewer surveys, following the method described in Appendix C.

Geological core logging data determined to be relevant to geological interpretation include the following, as presented in the geological and geotechnical core logging report (Golder, 2020c):

- Lithology
 - Rock Class and Type
 - Rock Fabric
 - Textures (Igneous, Metamorphic)
 - Grain Size (Ground Mass, Phenocryst/Porphyroblast)
 - Defining Minerals
 - Colours and Intensity
- Alteration
 - State
 - Mineral Assemblage
- Weathering
 - State
- Structure
 - Position along borehole
 - Type and Sub-type
 - Broken/Intact/Partially Intact
 - Infilling or Defining Mineral Details
 - Rock Wall Strength
 - Shape
 - Roughness
 - Dip and Dip-Direction
 - Alpha, Beta, Gamma, and Delta Angles
 - Geological Aperture
 - Width (where applicable)

Note that geological aperture is an estimated measurement of the open space between two adjacent fracture surfaces determined visually during geological core logging, during interpretation of downhole televiewer logs, or during the integration of data from these two sources. For our purposes, geological apertures are estimated values only because there are multiple possible sources of uncertainty in how a reported aperture value relates to the true aperture of a fracture identified as broken. There are uncertainties related to measurement inaccuracy, including where the opening is very small, where the opposing fracture planes are not parallel or fit poorly together, or due to limits in televiewer resolution. In addition, effects due to drilling or decompression may create or enhance the visible open space identified as aperture. Finally, aperture measured in core or on a borehole wall is only a local aperture that is not necessarily representative over the entire fracture.

To further understand the bedrock lithology, alteration, and structure along the length of the borehole, the following geophysical log results were determined to be most relevant:

- Optical Televiewer
- Acoustic Televiewer
- Natural Gamma
- Spectral Gamma
- Gamma-Gamma Density
- Neutron

All geophysical logging results are summarized in a separate geophysical logging report (Golder, 2020b). Prior to interpreting the geophysical log responses associated with distinct rock types from the borehole, minor positional adjustments were made to the geophysical log data to match log responses to key lithological markers identified in geological core logging, such as amphibolites which produce strong anomalies in density and neutron logs. Positional adjustments were minor, typically less than 10 cm.

To further increase the lithological understanding of IG_BH03, 22 core samples were collected for whole-rock major and trace element lithochemistry; qualitative thin section analysis was also performed on 18 of the 22 samples. Core samples were crushed, sieved, and separated for three different analyses. A portion of each sample was subjected to a lithium metaborate/tetraborate fusion, with the resulting bead digested in a weak nitric acid solution. Analyses were carried out by inductively coupled plasma optical emission spectrometry (ICP-OES) and inductively coupled plasma mass spectrometry (ICP-MS). A second portion of each sample was subjected to multi-acid digestion and analysis by ICP-MS and the third portion was sent for Instrumental Neutron Activation Analysis (INAA). Results from this analysis are integrated below to present a final interpretation of the lithological and alteration characteristics of IG_BH03. The lithochemical data are included in Appendix B.

3.1.1 Terminology

Several terms are introduced throughout this section to aid in describing the integration process. This includes:

- | | | |
|-----------------|---|---|
| Rock Unit | - | A borehole length comprising a dominant rock type and/or a combination of rock types (and, if applicable, alteration and weathering types) that are considered distinct from adjacent parts of the borehole. A minimum unit thickness of five (5) m is used herein to define each rock unit. Each rock unit is uniquely labelled and can be repeated with a sub-label at different positions along borehole if appropriate. |
| Structural Unit | - | A borehole length comprising a relatively uniform per metre fracture frequency that is distinct from adjacent parts of the borehole. Each |

structural unit is uniquely labelled and can be repeated with a sublabel at different positions along borehole if appropriate.

- Rock Type - A rock having a unique, identifiable set of characteristics.
- High Fracture Frequency Interval - A cluster of fractures (i.e., faults, joints and or veins) that exceeds a minimum relative fracture frequency threshold along a distinct borehole length.

3.2 Geological Results

This section presents the results from the integration of the geological core logging (WP03) and geophysical logging (WP05) datasets along with integration of the results from an additional 22 samples selected for petrographic and lithochemical analysis. Through the process of data integration, a total of eight distinct rock types are identified for IG_BH03 (Table 3). A final log of lithology is presented which shows their distribution along the length of the borehole (Figure 7).

3.2.1 Lithological Interpretation

The main rock type intersected by borehole IG_BH03 is a biotite granodiorite-tonalite. Additional, subordinate, rock types identified in IG_BH03 include distinct metre-scale packages of amphibolite and several suites of sub-metre thick dykes of varying felsic composition (Table 3 and Table 4). A total of 999.3 m of core was recovered, starting at 1.21 m along borehole. This final interpretation of the rock types encountered in IG_BH03, shown in Figure 7, presents an updated understanding relative to the information that was initially reported in the WP03 data report (Golder, 2020c). A short summary of this evolution of understanding is included along with the lithological descriptions below that summarize the main characteristics of the rock types identified in IG_BH03.

Table 3: Summary of rock types encountered in IG_BH03.

Rock Type	Texture	Fabric	Grain Size (mm)	Total Logged Length (m)	% of Recovered Core
Biotite granodiorite-tonalite	Equigranular	Massive to weakly foliated	0.2-7.5	973.95	97.5
Amphibolite	Equigranular	Foliated to massive	0.2-2	11.70	1.2
Feldspar-phyric tonalite dyke	Porphyritic	Foliated to massive	<0.3* 1.5-4**	4.66	0.5
Aplite dyke	Equigranular	Massive	<0.5	0.88	<0.5
Pegmatite dyke	Inequigranular	Massive	5-50	0.09	<0.01
Aphanitic tonalite dyke	Equigranular	Foliated	<1	5.93	0.6
Biotite granodiorite-tonalite dyke	Equigranular	Massive	0.1-5	0.24	<0.02
Granite dyke	Equigranular	Massive	0.2-2	1.89	<0.5

* Groundmass ** Phenocrysts

Table 4: Summary average of major oxides in the rock types of IG_BH03. Note that only 6 rock types were sampled for lithogeochemical analysis and there are no results for pegmatite, quartz, and biotite granodiorite-tonalite dykes. Aphanitic and Feldspar-phyric tonalite dykes are combined as they are compositionally the same.

Rock Type	Major Oxide Composition (average, %)									
	SiO ₂	Al ₂ O ₃	Fe ₂ O ₃	MnO	MgO	CaO	Na ₂ O	K ₂ O	TiO ₂	P ₂ O ₅
Biotite granodiorite-tonalite	73.57	14.16	1.82	0.03	0.41	1.99	4.64	2.26	0.19	0.05
Amphibolite	49.99	11.97	9.22	0.15	11.23	8.89	2.20	2.47	0.75	0.28
Aphanitic and Feldspar-phyric tonalite dykes	71.34	14.62	2.84	0.04	0.75	3.11	4.44	1.71	0.35	0.09
Aplite dyke	76.45	12.87	0.75	0.02	0.12	0.51	4.28	4.45	0.06	0.01
Granite dyke	77.12	12.87	0.59	0.02	0.05	0.52	4.50	3.99	0.04	0.01

Main Rock Type: Biotite Granodiorite-tonalite

IG_BH03 is dominated by a medium-grained felsic granitoid rock with biotite as the primary mafic mineral. This felsic granitoid rock represents a total of 97.5 % of the recovered core. The general consistency in character of the recovered core with the bedrock identified on the ground surface indicates that the biotite granodiorite-tonalite encountered in IG_BH03 is part of the same granodiorite-tonalite bedrock unit that was mapped at ground surface in the vicinity of the borehole (Golder and PGW, 2017). A total of 353 measurements were collected from a hand-held gamma ray spectrometer in the biotite granodiorite-tonalite during core logging, and the results are:

- Potassium content ranges from 0.5 – 1.2 % with an average of 0.86 %
- Uranium content ranges from 0 – 6.1 parts per million (ppm) with an average of 1.05 ppm
- Thorium content ranges from 0.1 – 8.7 ppm with an average of 5.28 ppm

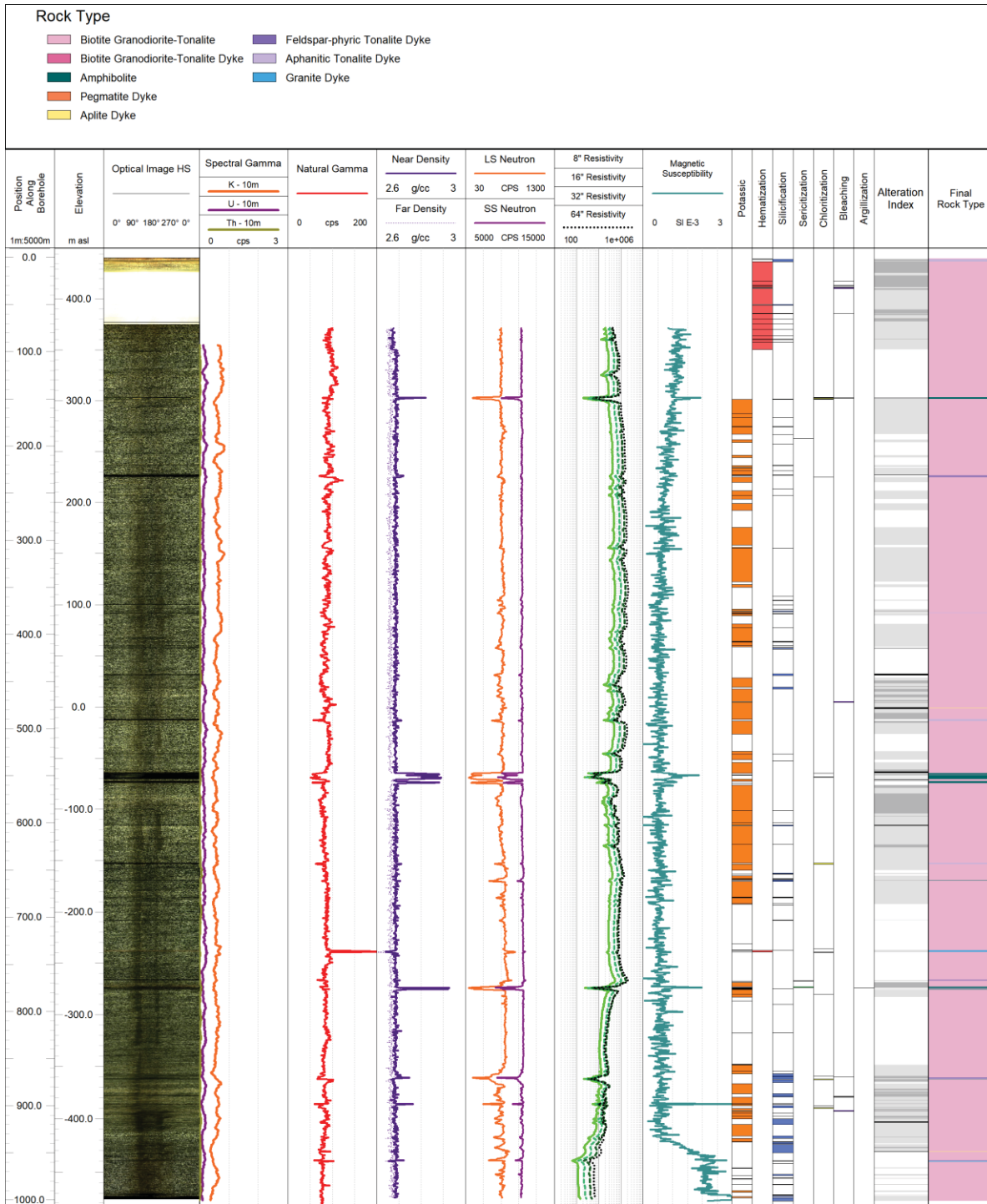


Figure 7: Input datasets used to correlate geophysical log response with core logged rock types to derive final alteration and lithology logs. Key continuous geophysical logs include elements of the spectral gamma log, the natural gamma log, near and far gamma-gamma density logs, and long-spacing (LS) and short-spacing (SS) Neutron logs.

Lithogeochemistry and petrography results from IG_BH01 indicate that the main rock type identified during geological core exhibits a range in composition that spreads across the tonalite to granodiorite boundary on a QAP ternary diagram (modal mineralogy) and plutonic rock classification diagram (lithogeochemistry; Parmenter et al., 2022). The modal mineralogy and lithogeochemistry data for samples from IG_BH03 support this interpretation (Figure 8 and Figure 10). Therefore, 'biotite granodiorite-tonalite' will continue to be used as the name for the main rock type. The lithogeochemical data and modal mineral composition of the samples, determined semi-quantitatively using polished thin sections, is presented in Appendix B.

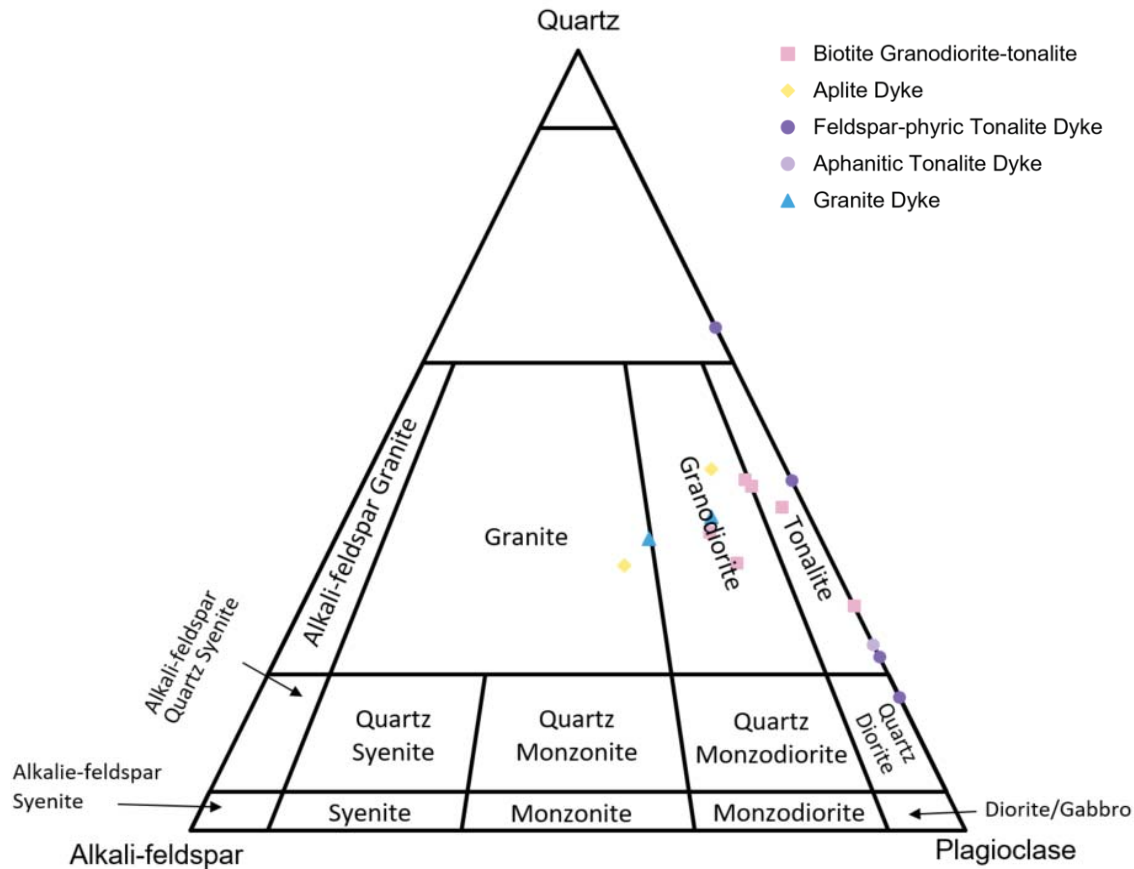


Figure 8: Classification/nomenclature of felsic granitoid phases according to the normalized modal mineral content (Quartz + Alkali-feldspar + Plagioclase = 100 Vol%) as determined from investigation of 15 samples taken for lithogeochemical analysis. Average modal mineralogy for each sample was determined semi-quantitatively using polished thin sections and plotted on a simplified ternary Streckeisen diagram after Le Bas and Streckeisen (1991).

The biotite granodiorite-tonalite unit is light to medium white-grey and mainly equigranular with mineral size tending towards the upper range of medium-grained (0.3-4.0 mm average) for all mineral phases (Figure 10). Its main mineral phases are quartz, plagioclase, potassium feldspar, and biotite, with the latter comprising 1-8 % of the matrix. This rock is predominantly massive although a weak biotite-defined foliation is locally apparent. There were 6 samples from IG_BH03 sent for optical petrography, and they plot across the tonalite to granodiorite field on the QAP diagram (after Le Bas and Streckeisen, 1991; Figure 8) based on visually-determined area coverage of visible minerals in the polished thin section using a known scale grid. Ten samples were sent for bulk lithogeochemical analysis and the major oxides demonstrate a felsic composition

(Table 4) and plot across the tonalite to granodiorite fields on the plutonic rock classification diagram (after Debon and Le Fort, 1983; Figure 9).

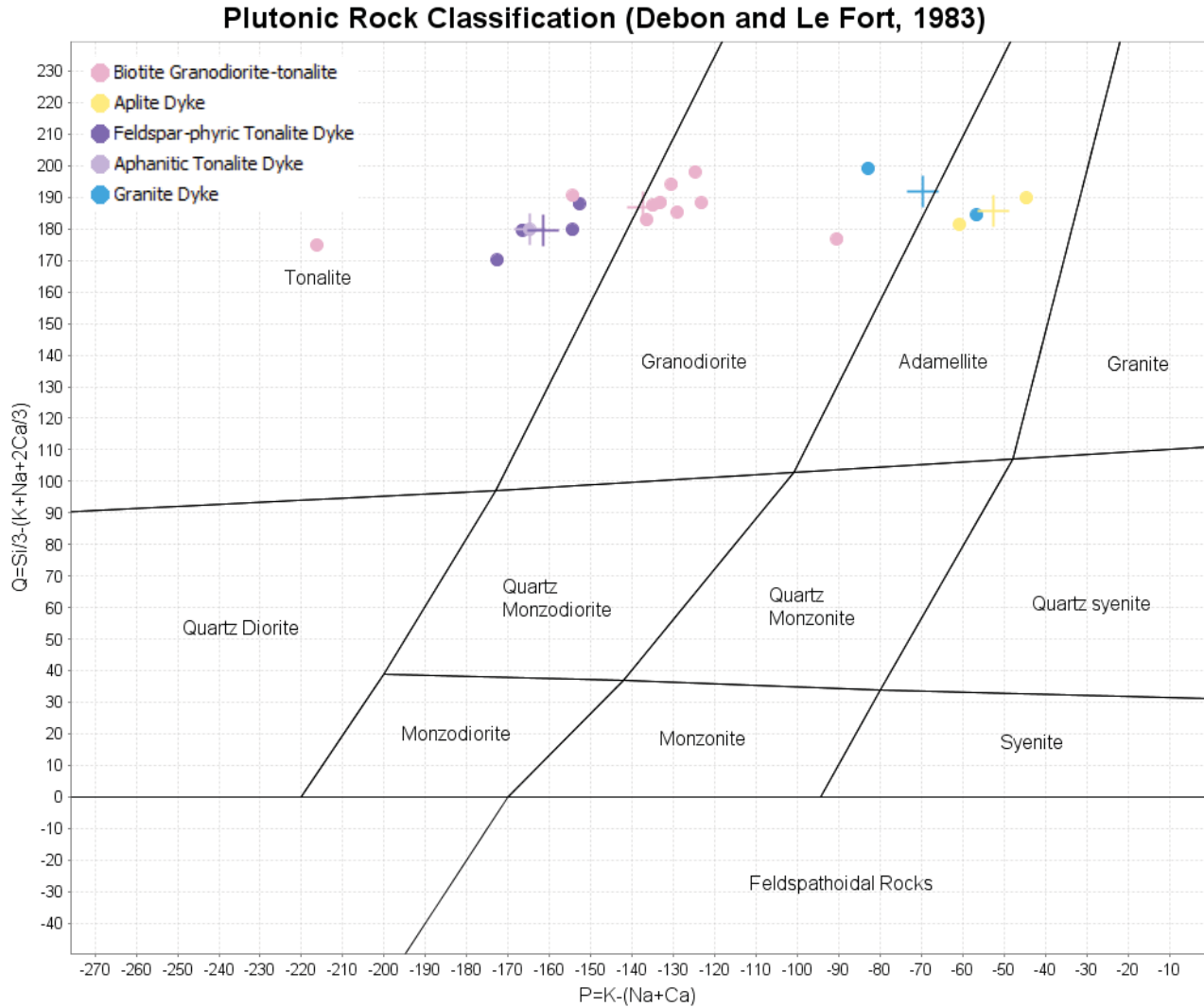


Figure 9: Plutonic Rock Classification (Debon and Le Fort, 1983). Diagram axes correspond to proportions of K-feldspar and plagioclase to quartz. P is calculated from $(\text{K} - (\text{Na} + \text{Ca}))$ and Q is calculated from $((\text{Si}/3) - (\text{K} + \text{Na} + (2 \cdot \text{Ca})/3))$. Parameters calculated as oxide percentages converted to millications. Crosses show the mean composition for each rock type.

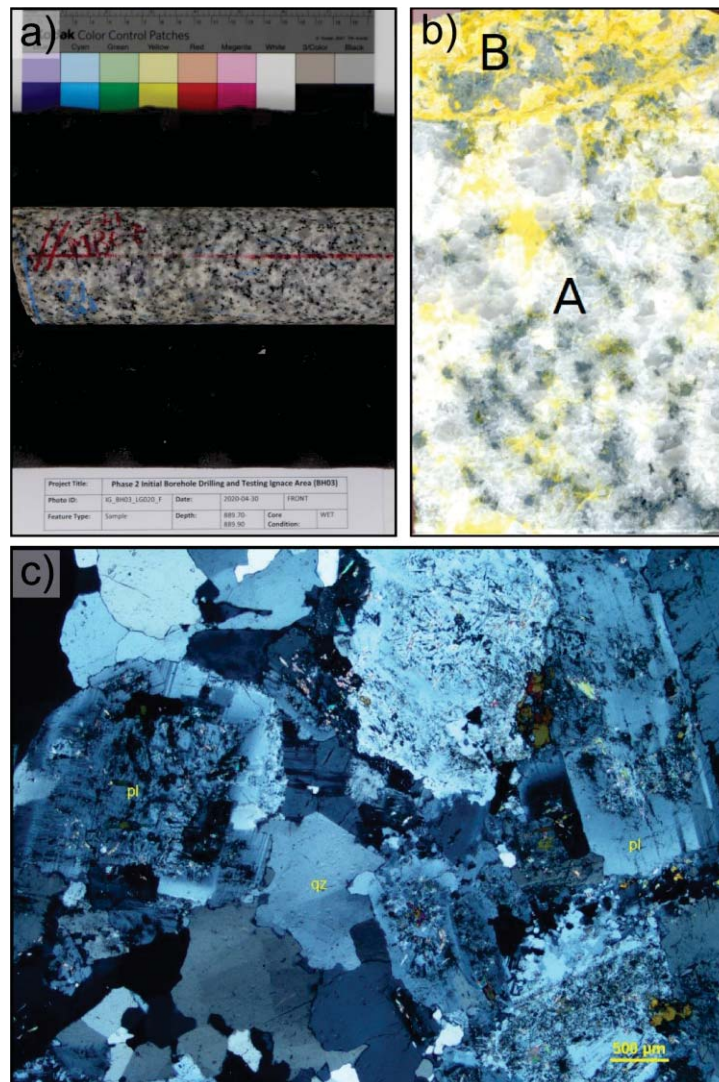


Figure 10: Representative examples of biotite granodiorite-tonalite (sample IG_BH03_LG020). a) Hand-sample photograph. b) Billet photograph showing yellow staining of potassium feldspars (billet size is 25 x 40 mm; large A and B are differentiating different grain size domains in the sample). c) Thin section photomicrograph with rock-forming minerals plagioclase (pl) and quartz (qz). Sericite (white mica) alteration can be seen in cores of plagioclase crystals. Minor biotite is present (dark greenish/brown mineral); crossed polarizers transmitted light.

Subordinate Rock Types

In IG_BH03, the subordinate rock types encountered (amphibolite, aphanitic tonalite dykes, feldspar-phyric tonalite dykes, aplite dykes, pegmatite dykes, biotite granodiorite-tonalite dykes, and granite dykes) represent a combined total of 2.5 % of the recovered core (Table 3). A new subordinate rock type was identified during logging of IG_BH03. Two dykes, at 735 and 958 m, were initially classified as tonalite dykes. It was unclear from hand sample whether these dykes were altered versions of a known, or newly encountered, rock type. Samples were sent for optical petrography and bulk lithogeochemistry and were classified as granite according to the petrography. Lithogeochemically, they are closer to quartz monzonite or granodiorite, but as there are only two samples, we have opted to keep the granite name assigned during petrographic analysis, which is discussed further below.

Amphibolite: Twelve occurrences of amphibolite were originally logged in IG_BH03, accounting for 13.1 m (1.3 %) of the total recovered core. Lithogeochemical results suggested that one interval at 642 m was incorrectly logged as an amphibolite and was actually an aphanitic tonalite dyke. The aphanitic tonalite dykes are very dark in colour and do look similar to the amphibolites, but the lithogeochemistry results were definitive and this interval was reclassified, changing the total amphibolite logged to 11.7 m (1.2 %) of the total recovered core (Table 3). It is unclear whether the amphibolite units are dykes or xenoliths from the surrounding greenstone belts, or a combination, because primary contact relationships such as chilled margins are obscured by penetrative deformation localized along the amphibolite contacts. They will be referred to as *amphibolites* in this report and refine this term as more information is received from future boreholes. The amphibolites range in width from 0.13 m to 2.43 m. One amphibolite was identified at approximately 148 m along borehole, while the remainder of the occurrences were observed below 500 m along borehole (Figure 7). The identified amphibolites consistently exhibit sharp increases in density values and decreases in neutron values. Amphibolites are dark grey-green, equigranular, and generally fine- to medium-grained (0.2 – 2 mm; Figure 11). The mineral assemblages include tremolite/actinolite, biotite, quartz, epidote, albite, and chlorite +/- pyrite. The mineral assemblages are suggestive of albite-epidote hornfels facies metamorphism of basic rocks (Raymond, 2002).

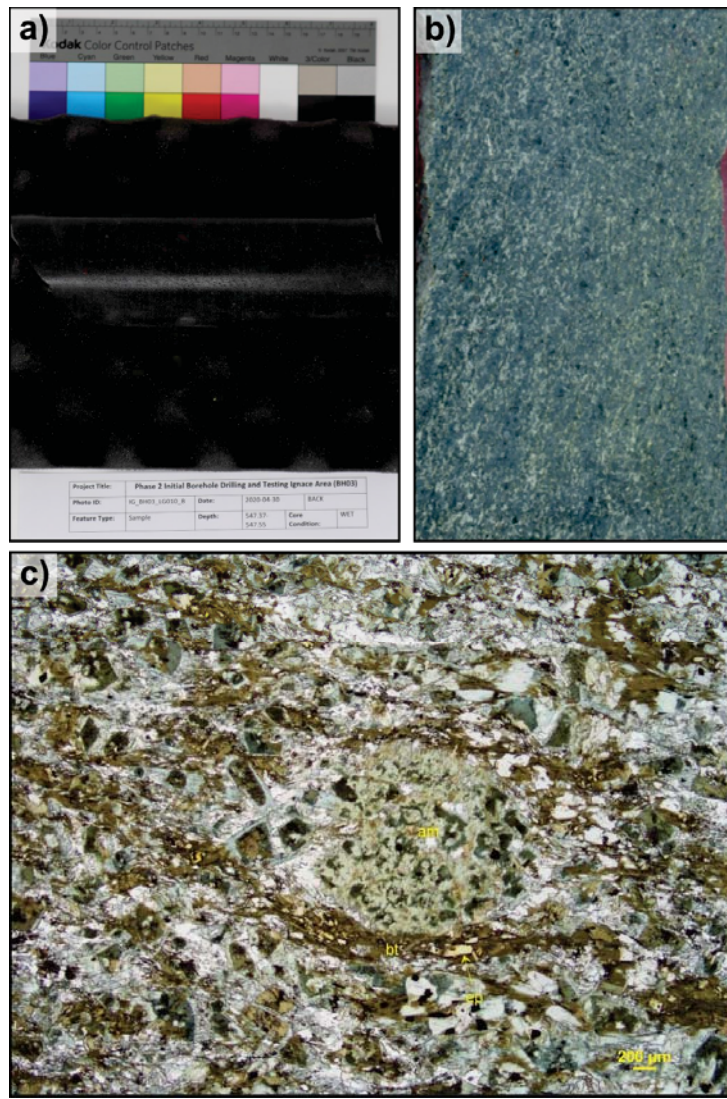


Figure 11: Representative examples of amphibolite (sample IG_BH03_LG010). a) Hand-sample photograph. b) Billet photograph (billet size is 25 x 40 mm). c) Thin section photomicrograph with main rock-forming minerals amphibole (am; tremolite-actinolite), biotite (bt) and epidote (ep); plane polarized transmitted light.

Lithogeochemistry shows an increase in iron and magnesium and a decrease in silica relative to the felsic units, which is expected in a mafic unit (Table 4). The amphibolites consistently exhibit a well-defined foliation and sharp contact where they contact the adjacent biotite granodiorite-tonalite; six of the contacts were logged as broken (6/28, 21 %). As will be discussed later in the summary of structural information (Section 3.2.4), the contacts between individual amphibolite occurrences and the adjacent biotite granodiorite-tonalite primarily dip shallowly-moderately towards the north-northwest. Within the amphibolite occurrences themselves, transitions between massive and strongly foliated domains are common and often observed to be sharp.

The internal foliation is generally observed to align with the orientation of the contacts. A decimetre- to metre-scale hematite +/- potassic alteration halo commonly envelops the amphibolite in the surrounding biotite granodiorite-tonalite. In addition, some fracture surfaces within the amphibolites are coated by chlorite.

Aphanitic and feldspar-phyric tonalite dykes: A suite of distinct felsic dykes was initially logged in ten occurrences along the length of the borehole (Figure 7). Dykes range in width from 0.15 m to

2.35 m and have a combined total length of 9.19 m, representing 0.9 % of the recovered core. After reclassifying one of the amphibolite units as an aphanitic tonalite dyke during integration of the lithogeochemical data, there are 11 occurrences with a combined total length of 10.59 m, representing 1.1 % of the recovered core (Table 3). These dykes are characteristically dark grey-black with an aphanitic matrix (Figure 12). Petrographic analysis identified the mineral composition of the dykes as quartz, plagioclase, and biotite with minor alkali feldspar and major oxides suggest a felsic composition (Table 4). Nine of the occurrences also exhibit distinct, medium-grained albite phenocrysts within a matrix that is otherwise compositionally and texturally similar to the other six occurrences (Figure 12). During logging, these dykes were termed felsic or feldspar-phyric felsic dykes. Petrographic and lithogeochemical analyses of five samples from this suite of felsic dykes plot entirely within the tonalite field on the plutonic classification diagram (Figure 9). Based on this additional information, these names are refined to *aphanitic tonalite* and *feldspar-phyric tonalite* dykes. One hand-held gamma spectrometry measurement from an aphanitic tonalite dyke yielded results of 0.9 % potassium, 5.5 ppm thorium, and 0.4 ppm uranium.

All of the aphanitic tonalite and feldspar-phyric tonalite dykes exhibit sharp contacts with the adjacent biotite granodiorite-tonalite and, in some occurrences, a well-defined foliation is also present. In thin section, this foliation is a weak to moderate schistosity defined by the alignment of biotite and quartz. Contacts were primarily intact with only a small number of occurrences (2/28; 7 %) identified as broken. Internally, these aphanitic tonalite and feldspar-phyric tonalite dykes vary between massive and foliated (schistose).

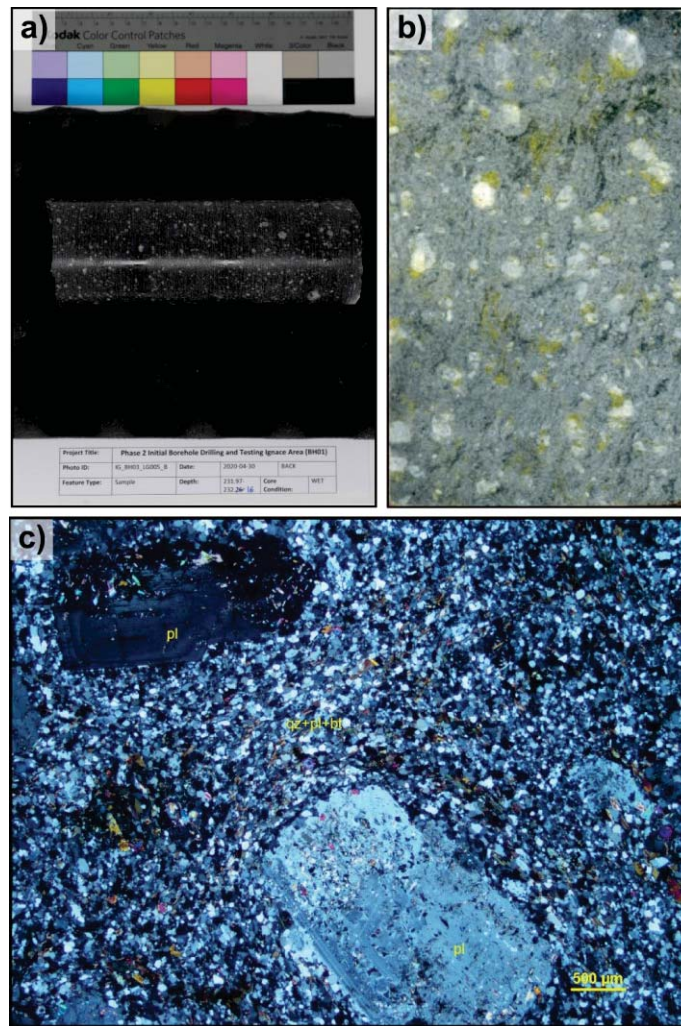


Figure 12: Representative examples of feldspar-phyric tonalite dyke (sample IG_BH03_LG005). a) Hand-sample photograph. b) Billet photograph showing yellow staining of alkali feldspar (billet size is 25 x 40 mm). c) Thin section photomicrograph with plagioclase (pl) phenocrysts, in a very fine-grained matrix of quartz (qz), plagioclase (pl), and biotite (bt); crossed polarized transmitted light.

Aplite dykes: Aplite dykes, ranging in width between 0.07 m and 0.36 m, were observed in four occurrences, and represent a combined total length of 0.88 m (<0.5 %) of the recovered core (Table 3). The aplite dykes are light white-grey, equigranular and very fine-grained (<0.5 mm). The aplite dykes are granitic in composition (Figure 9 and Table 4) with main mineral phases of plagioclase, potassium feldspar, quartz and minor biotite (Figure 13). Three hand-held gamma ray spectrometry measurements were taken in aplite dykes; potassium values ranged from 0.8 – 1.2 % (0.97 % average), thorium values ranged from 4 – 7.3 ppm (5.2 ppm average), and uranium values ranged from 0.4 – 1.8 ppm (0.97 ppm average). Contact between the aplite dykes and the adjacent biotite granodiorite-tonalite are consistently sharp and intact.

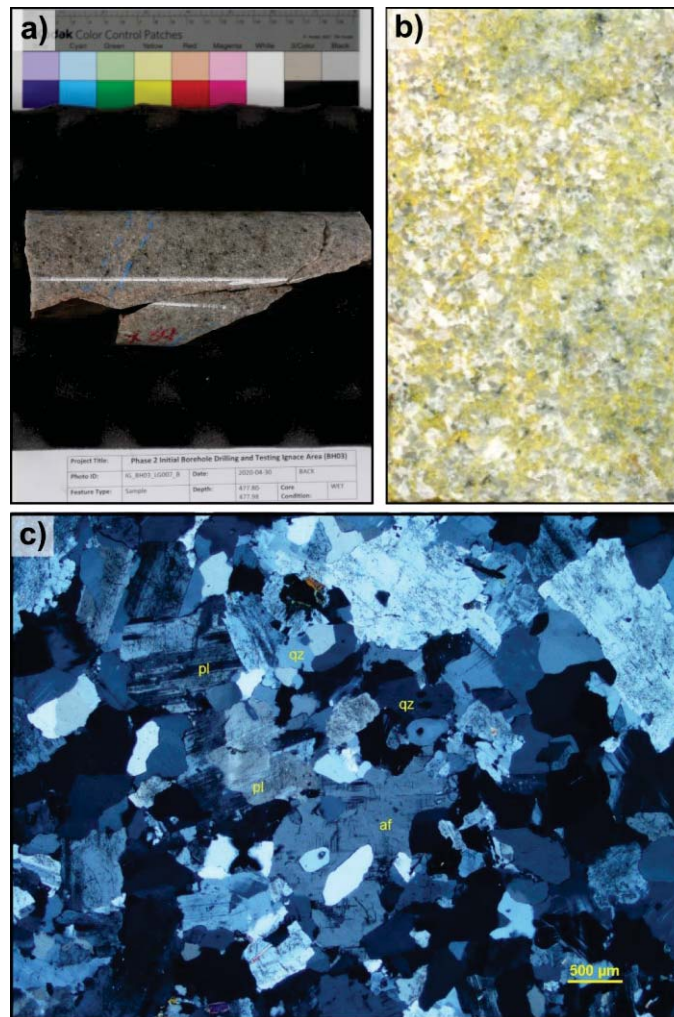


Figure 13: Representative examples of an aplite dyke (sample IG_BH03_LG007). a) Hand-sample photograph. b) Billet photograph showing yellow staining of alkali feldspar (billet size is 25 x 40 mm). c) Thin section photomicrograph with rock-forming minerals plagioclase (pl), alkali feldspar (af) and quartz (qz); crossed polarized transmitted light.

Pegmatite Dykes: One 0.09 m thick pegmatite dyke was logged at 920 m, representing <0.1 % of the recovered core (Table 3). The dyke is light grey-pink, massive, and inequigranular with distinct, very coarse-grained (10-50 mm), square-edged feldspar crystals within a medium-grained (5-10 mm) matrix of quartz, feldspar, and biotite. The pegmatite dyke exhibits a sharp, chilled, intact contact with the adjacent granodiorite-tonalite. One hand-held gamma spectrometry measurement from the dyke yielded results of 0.9 % potassium, 5.4 ppm thorium, and 2.1 ppm uranium.

Biotite granodiorite-tonalite dykes: Two biotite granodiorite-tonalite dykes, with widths of 0.1 and 0.14 m, were logged, representing < 0.1 % of total recovered core (Table 3). One dyke was observed at 157 m along borehole and other at 984 m along borehole (Figure 7). These occurrences are identified as dykes herein as they appear to crosscut the main bedrock units. These dykes are light grey-off white, and massive. The dyke at 157 m is equigranular and medium-grained (5-10 mm). The dyke at 984 m is coarser grained at the upper contact with 8-10 mm quartz and biotite crystals. The grain size decreases to fine grained at the lower contact. These two dykes exhibit sharp and consistently intact contacts with the adjacent biotite granodiorite-tonalite. The shallower of the two, at 157.64 m, is moderately dipping to the northeast. The deeper dyke, at

984.09 m, is shallowly dipping to the east-southeast. These units have been identified as dykes based on visible intrusive contacts and narrow width.

Granite dykes: Two dykes of unknown rock type were initially identified during geological core logging as tonalite dykes. The first dyke was logged at 735 m with a width of 1.51 m and the second was logged at 958 m with a width of 0.38 m, representing < 0.5 % of total recovered core (Table 3). Both occurrences exhibit sharp, intact contacts with the adjacent biotite granodiorite-tonalite. Samples were taken of each dyke for petrography and lithogeochemistry and both were identified as equigranular, medium-grained leucogranites (Figure 14 and Table 4). The same intrusive relationship, between a younger granite and older granodiorite-tonalite, is observed at the surface. Based on this, and the petrography and lithogeochemistry results (Figure 9), these dykes are collectively termed granite dykes. These granite dykes may be associated with the potassium-feldspar megacrystic granite phase of the Revell batholith.

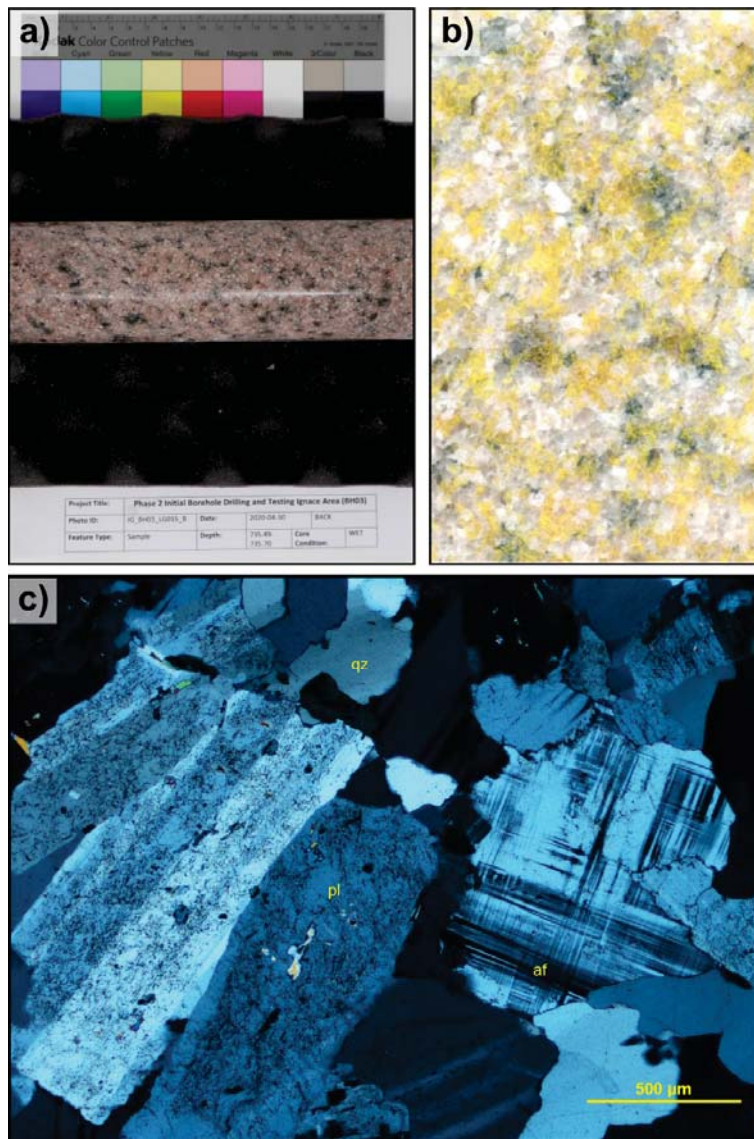


Figure 14: A leucogranite dyke from 735 m along borehole (sample IG_BH03_LG015). a) Hand-sample photograph. b) Billet photograph showing yellow staining of alkali feldspar (billet size is 25 x 40 mm). c) Thin section photomicrograph with rock-forming minerals plagioclase (pl), alkali feldspar (af) and quartz (qz); crossed polarized transmitted light.

Summary of rare-earth element data for IG_BH03

Rare-earth element data, collected as part of the lithogeochemistry analysis, is plotted for samples from IG_BH03 (Figure 15). Rare-earth element (REE) chondrite-normalized plots of amphibolite are moderately-steeply fractionated [average $(La/Yb)_4 = 32.7$] with a significant depletion in heavy rare-earth elements [HREE; average $(Gd/Er)_4 = 3.3$]. Biotite granodiorite-tonalite and the aphanitic and feldspar-phyric tonalite dykes are steeply fractionated [average $(La/Yb)_{14} = 58.8$] with significant depletion of HREE [average $(Gd/Er)_{14} = 3.7$]. The similar pattern of the amphibolite and biotite granodiorite-tonalite phases may indicate that they are from the same magmatic source, though the origin of the amphibolite inclusions is still being investigated. The aplite and granite dykes are much less steeply fractionated [average $(La/Yb)_4 = 7.6$] and are less depleted in HREE [average $(Gd/Er)_4 = 1.5$]. The aplite and granite dykes, which are possibly the same unit with different grain sizes,

show a sharply negative europium anomaly and are enriched in potassium compared to the other units ($K_2O = 3.4-4.6\%$), suggesting they are later stage, evolved granite intrusions. Our biotite granodiorite-tonalite samples plot with other Neoproterozoic low-HREE granitoids of the tonalite-trondhjemite-granodiorite (TTG) suite, which carry a basaltic crust signature (Halla, 2018 and references therein). The origin of low-HREE TTG's is thought to be high-pressure melting of deep, thick oceanic crust during subduction. One reason for a depletion of HREE is residual garnets are retaining the HREE in the source basalt (Halla et al., 2009). There is limited spread in the biotite granodiorite-tonalite and tonalite dyke samples even though some intervals specifically targeted alteration, suggesting the alteration is generally weak.

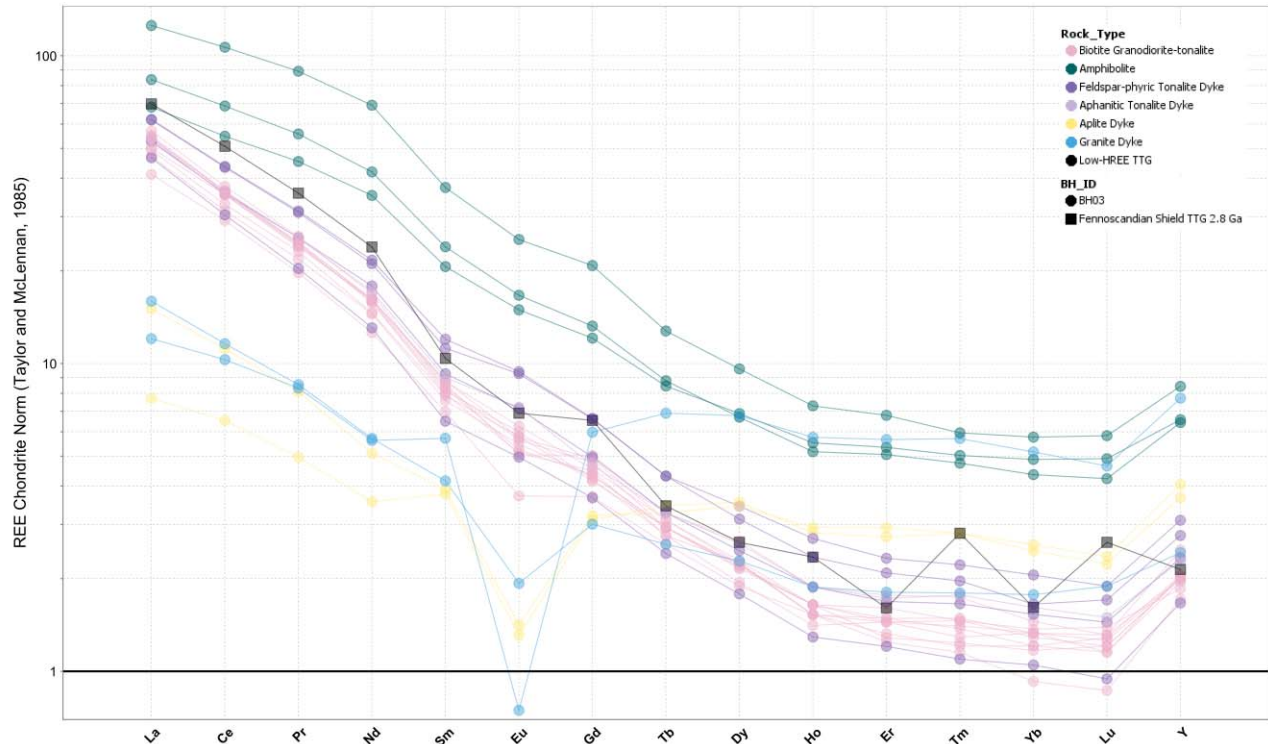


Figure 15: Chondrite-normalized rare-earth element (REE) plot (after Taylor and McLennan, 1985) of rock types from IG_BH03 and a representative average of 2.8 Ga low-heavy REE (HREE) tonalite-trondhjemite-granodiorite (TTG) from the Fennoscandian shield (black squares; Halla, 2018). Y-axis shows concentrations (expressed as logarithm to the base 10 of the value) of REE (x-axis, by atomic number) in IG_BH03 samples normalized to a reference Chondrite standard. REE patterns of biotite granodiorite-tonalite, aphanitic tonalite dykes, and feldspar-phyric tonalite dykes demonstrate steep fractionation and significant depletion of HREE. Aplite and granite dykes demonstrate a less steep fractionation and significant europium anomalies, suggesting they are from a later stage, evolved granite source.

Geophysical characteristics of the identified rock types

A suite of geophysical logs, including natural gamma, spectral gamma, gamma-gamma density and neutron are widely used both for identifying rock types and delineating contacts (e.g., Keys, 1997). Such subtle boundaries could reflect sharp or gradational changes in mineralogical composition, such that any variability not observed in the initial stage of geological core logging could be identified by assessment in comparison with these geophysical logs (Figure 7). The discussion below describes each of these geophysical logs to characterize the bedrock, in general, and applies this information to evaluate the specific rock types encountered in the borehole. A summary table of mean geophysical responses is included in Table 5.

Table 5: Mean geophysical response values for each logged rock type.

Rock Type (N=number of data points)	Natural Gamma (cps)	Neutron* (cps)	Density** (g/cc)	K (cps)	Th (cps)	U (cps)
Amphibolite (N = 234)	67.12	153.69	2.81	0.52	0.04	0.14
Aphanitic tonalite dyke (N = 67)	65.57	465.42	2.69	0.58	0.05	0.14
Aplite dyke (N = 19)	98.24	627.83	2.66	0.54	0.04	0.16
Biotite granodiorite-tonalite (N = 17934)	86.71	553.81	2.67	0.61	0.03	0.16
Biotite granodiorite-tonalite dyke (N = 5)	92.70	572.85	2.66	0.55	0.03	0.13
Feldspar-phyric tonalite dyke (N = 87)	70.89	481.42	2.70	0.62	0.02	0.19
Granite dyke (N = 38)	176.61	664.89	2.64	0.60	0.03	0.24
Pegmatite dyke (N = 2)	97.44	598.41	2.67	0.58	0.04	0.19

* long spacing neutron sensor values are presented.

** mean gamma-gamma density values, from near and far measurements, are presented.

The natural gamma log quantifies the amount of radioactive isotopes occurring naturally within the bedrock typically corresponding to mineralogy, however, does not identify the responsible radioisotopes. However, results from the spectral gamma log can be useful to differentiate the relative amount of radioisotopes, such as potassium, uranium and thorium (herein presented in counts per second - cps). Although data from natural gamma and spectral gamma logs do not correlate directly to specific rock types, their relative variabilities along the length of the borehole are used to assess mineralogical variation that indicate the change from one rock type to the next.

Data measured from both the gamma-gamma density and neutron logs were used to quantify petrophysical properties of the bedrock (e.g., bulk rock density), and were correlated to specific rock types. Measurement of these logs are, however, sensitive to variations in pore space in the bedrock. The gamma-gamma log measures the backscatter and attenuation of gamma photons emitted at a near and far sensor from the logging gamma source where the measured response is converted to bulk density through calibration prior to recording data.

The neutron log uses a neutron source and detector to measure the relative neutron counts in the bedrock along the borehole wall. Most neutron interactions can be inversely related to hydrogen ion concentrations in the bedrock, such that, responses can be generally related to water content or porosity of the bedrock (e.g., Daniels et al., 1984; Keys, 1997). In some instances, neutron counts can be influenced by relative changes in bedrock mineralogy, primarily the presence of hydrous minerals (e.g., biotite, amphiboles, and chlorite).

Although electrical resistivity, single point resistance and induction logs can be used as a diagnostic tool to interpret rock types and contacts, within the rocks identified in this borehole there is no indication of there being changes associated with varying rock types. Evidence suggests that discrete variations in electrical resistivity or single point resistance may be largely correlated to the presence of fractures (e.g., fracture frequency) and particularly fractures with measured geological aperture or secondary porosity (e.g., fracture porosity).

Description of borehole geophysical data acquisition and processing are detailed in Golder (2020b). For this report, data underwent additional positional corrections, and for this analysis have been exported at a uniform spacing of 5 cm along the length of the borehole from bottom of casing to end of borehole. Continuously measured natural gamma, spectral gamma, neutron (long-spacing sensor), and density responses are presented in Figure 7 and were used to highlight variations in physical bedrock properties along the borehole. For analysis, a mean density profile is calculated based on the average of the near and far density values along the length of the borehole.

The biotite granodiorite-tonalite phase make up the majority of the measured geophysical response values (see Table 5) and can be attributed as the base-line values for the bedrock. Any deviations away from this response tend to be associated with various factors, including changes in rock type and associated mineralogy, presence of fractures and associated infillings, and/or presence of alteration types and associated intensities.

The distributions of natural gamma, density and neutron responses present observable differences in the geophysical responses between each rock type. As shown in Figure 16, a suite of felsic dykes (granite, aplite, biotite-granodiorite-tonalite and pegmatite dykes) present a subtle increase in natural gamma relative to the main rock type logged in the borehole, the biotite granodiorite-tonalite. Whereas the amphibolite, feldspar-phyric tonalite dyke and aphanitic tonalite dyke present a slight reduction in natural gamma response. Overall, natural gamma, neutron, and density distributions shown in Figure 16 display considerable similarities between all felsic rocks, with the exception of two granite dykes. These dykes show significant increases in measured natural gamma radiation, which present themselves as clearly distinct with their mean response is typically 2 to 3 times higher than values measured for other rock types (Table 5 and Figure 16). Such a responses in granite or pegmatitic dykes can be associated with enrichment in radioactive elements such as uranium (e.g., Hewitt 1967), however, the spectral gamma uranium counts for the granite dykes are not significantly enriched (see Table 5: mean uranium counts 0.24 cps). The relative increase in natural gamma response for these granite dykes are very similar to the increase measured for the aplite dyke suite within IG_BH01 (Parmenter et al., 2022). The overall spectral gamma log response (potassium, uranium and thorium) for the entire borehole suggests that the rock types encountered are generally depleted in these radioactive isotopes.

The amphibolite occurrences in the borehole present a characteristic reduction in neutron counts and an increase in bulk density relative to the biotite granodiorite-tonalite. The increased bulk density of amphibolites can be directly related to the presence of tremolite-actinolite which is a relatively dense mineral, especially in comparison to the main mineral phases comprising the felsic units (i.e., plagioclase, alkali feldspar and quartz). The reduced neutron counts of the amphibolites can possibly be associated with an increase in apparent primary porosity, however, it is more likely related to secondary (e.g., fracture) porosity or the hydrous nature of their mineral assemblage (e.g., chlorite, amphibole).

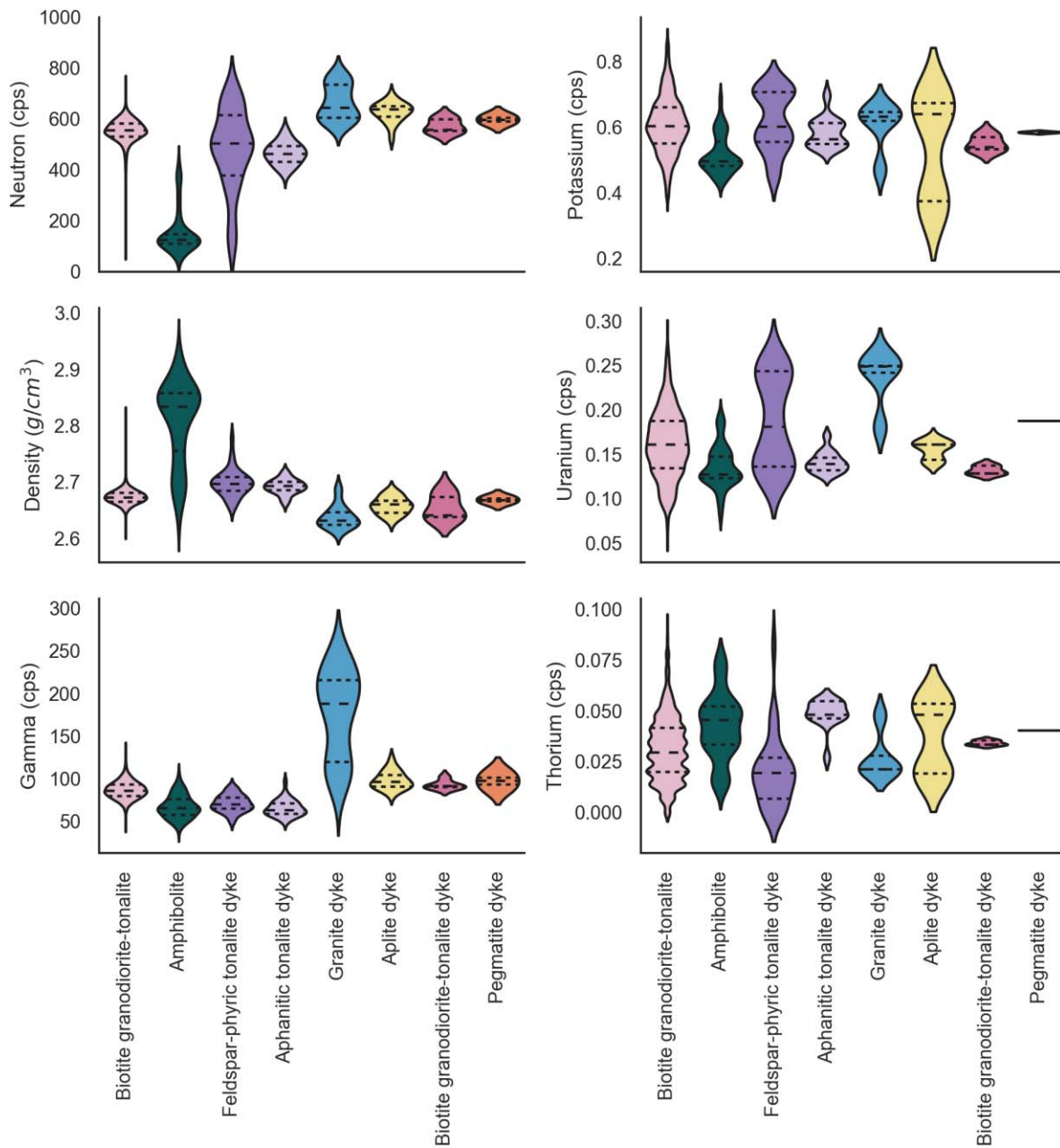


Figure 16: Violin plots show the distribution of geophysical log responses associated with the logged rock types. Each violin shows the distribution of the data values with the median (thick dashed line), and quartiles (thin dashed lines) marked. Rock types are ordered based on total data counts from left to right in each graph.

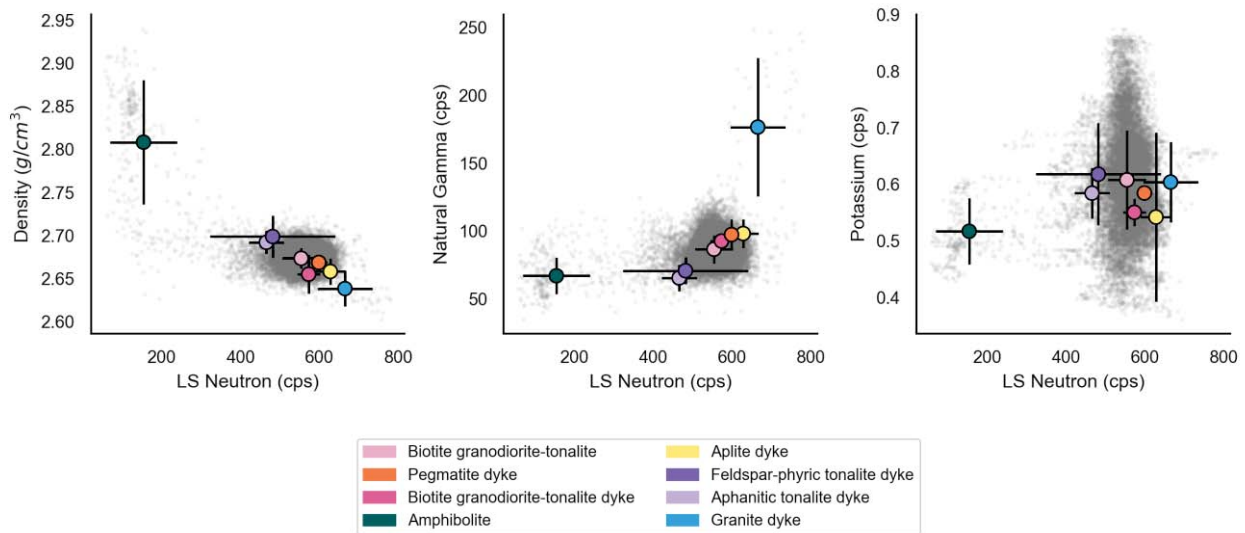


Figure 17: Distribution of Neutron and Density Values of all Rock Types encountered in IG_BH03. Colored points represent mean values of the geophysical response and the error bars represent standard deviation.

Cross-plots are presented in Figure 17 showing the cross-correlation between the selected geophysical log data and corresponding rock types. Scattered data points are plotted for the entire length of the borehole at 5 cm intervals. The larger data points represent mean centroid values of the geophysical responses and the error bars represent the standard deviation.

Overall, the distributions of biotite granodiorite-tonalite, pegmatite and aplite dykes, feldspar-phyrlic tonalite dykes, and aphanitic tonalite dykes largely overlap making distinguishing between them using geophysical comparison plots alone difficult. However, the granite dykes tend to be uniquely characterized by a high natural gamma (Figure 7). Amphibolites are uniquely characterized by low neutron counts, and high bulk densities and can be distinguished from the other felsic units in all cross-plots (Figure 17). Most of the density values over approximately 2.75 g/cm³ are attributed to amphibolites.

3.2.2 Alteration Interpretation

Seven alteration types were logged in IG_BH03 over a total length of 623.35 m (62.3 %). The alteration types logged, in order of prevalence, were: potassic alteration, hematization, silicification, chloritization, bleaching, sericitization, and argillization. Descriptions for each alteration type are included below (Table 6), hand sample and thin section examples are shown in Figure 18, and the distribution is shown in the final alteration log (Figure 19). Detailed descriptions of alterations observed during geological core logging are also included in the IG_BH03 WP03 report (Golder, 2020c).

The final alteration log displays the summary of the data integrated to define the log, including the WP03 alteration log and the additions from assessment of the optical televiewer log. During geological core logging, 478.46 m (47.8 %) of the recovered core was assigned as slightly altered (A2), where the alteration is generally confined to fractures with little or no penetration beyond the fracture plane. 133.8 m (13.4 %) was assigned as moderately altered (A3), where alteration may penetrate into the wall rock and create an envelope or halo of alteration around a fracture plane. 11.09 m (1.1 %) was assigned as highly altered (A4), where alteration is pervasive causing a significant decrease in rock strength.

Table 6. Summary of alteration assemblages observed in IG_BH03 during geological core logging.

Alteration Type	Total length (m) of logged core	Position along borehole	Hand Sample Description	Associated secondary alterations
Potassic	446.49 m	Below 150 m	Pink colour; individual occurrences range from hairline to 82.6 m	Silicification and chloritization
Hematization	94.85 m	Predominantly in the top 100 m	Red, brown, or rusty staining of rock or coating around mineral grains; occurrences range from hairline to 93.1 m	None
Silicification	63.42 m	Spread throughout borehole, increase below 850 m	Grey discoloration and reduction in clarity of grain boundaries (esp. quartz); occurrences range from hairline to 9.1 m	Sericitization, chloritization, and potassic
Chloritization	11.54 m	Spread throughout borehole	Appearance of green chlorite; occurrences range from hairline to 4.0 m. Associated with dykes.	Potassic
Bleaching	6.08 m	Spread throughout borehole	Whitening of the altered rock mass; occurrences range from hairline to 1.42 m	None
Sericitization	0.97 m	200 m and 770 m	White to grey colour; occurrences range from 0.06 – 0.48 m	Hematization
Argillization	0.01 m	774 m	White colour, softening of altered rock; occurrence was 0.01 m	None

Six samples sent for optical petrography from IG_BH03 specifically targeted logged alteration assemblages. Overall, the samples exhibited weak alteration to the general rock mass with moderate alteration to some individual minerals. All plagioclase feldspar grains recorded some degree of sericitization (white mica), often associated with chloritization of biotite +/- epidote. This white mica alteration was present in dykes as well as the rock mass, suggesting it is a result of hydrothermal alteration that took place after or contemporaneous to emplacement of all rock types. Two samples originally logged as tonalite dykes with potassic alteration and silicification were re-classified as granite dykes with no significant alteration. What was originally logged as potassic alteration in these dykes turned out to be primary potassium feldspar.

In some intervals of biotite granodiorite-tonalite, hematite was found to partially replace magnetite grains (Figure 18). These intervals were originally identified as potassic alteration during geological core logging; none of the intervals logged with potassic alteration show evidence of true hydrothermal potassic alteration (secondary alkali feldspar, biotite, sulphides) when examined petrographically. The pink colour is a product of magmatic (primary) alkali feldspar or replacement of very fine-grained sulphides or magnetite by iron oxides. These iron oxides (e.g., hematite) stain the surrounding crystals red, causing the entire interval to look pink.

Two intervals with alteration logged as bleaching showed weak to moderate alteration of plagioclase by white mica with some associated epidote (Figure 18). This suggests that what is called bleaching during core logging is actually the alteration of plagioclase feldspar to white mica (sericite) causing a whitening of the grains and, therefore, the overall rock.

In amphibolite intervals, iron oxide idiomorphic pseudomorphs (potentially hematite) were found to completely replace pyrite and/or other sulphide minerals. Chlorite alteration is also commonly associated with amphibolite (Figure 18).

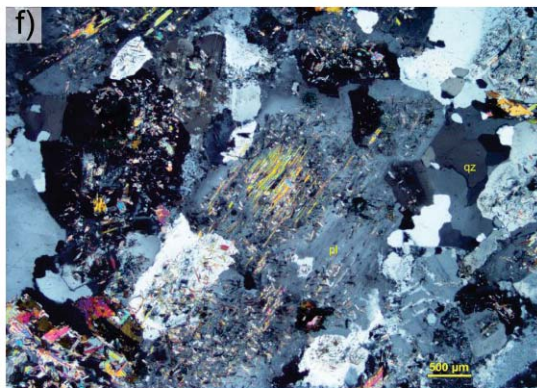
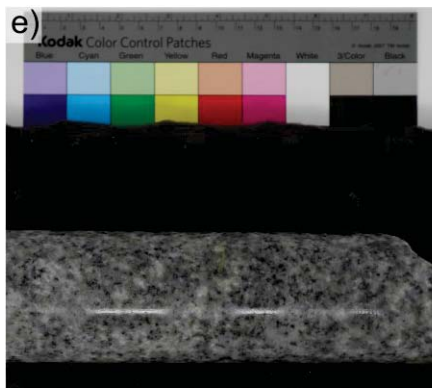
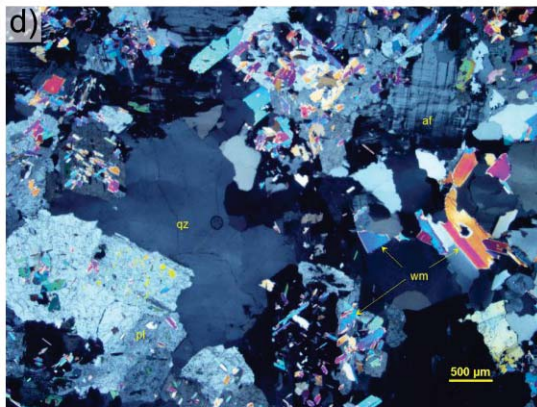
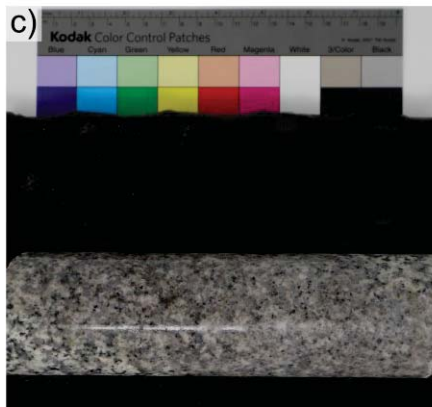
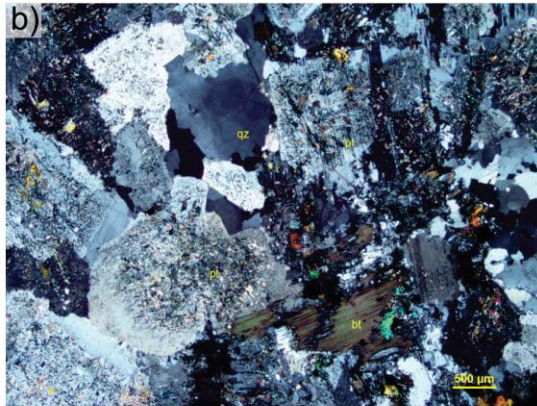
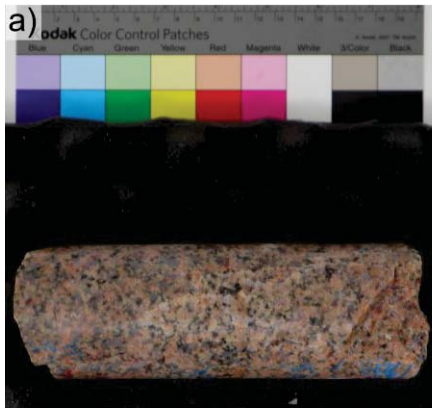


Figure 18: Common alteration assemblages logged in IG_BH03. a) Sample IG_BH03_LG017, biotite granodiorite-tonalite logged with potassic and hematite alteration and iron. b) Photomicrograph of sample IG_BH03_LG017 showing plagioclase crystals (pl) heavily altered by white mica and epidote, biotite (bt) weakly altered by chlorite and iron oxide, and quartz (qz); crossed-polarized transmitted light. c) Sample IG_BH03_LG006, biotite granodiorite-tonalite logged as silicified. d) Sample IG_BH03_LG006 showing quartz grains (qz), alkali feldspar (af), plagioclase (pl) with white mica (wm) altered plagioclase and filling interstitial space; crossed-polarized transmitted light. e) Sample IG_BH03_LG019, biotite granodiorite-tonalite logged as bleached. f) Sample IG_BH03_LG019 showing plagioclase (pl) moderately altered by white mica, and quartz grains; crossed-polarized transmitted light. g) Hematite and chlorite alteration coating a fracture at a contact between biotite granodiorite-tonalite and amphibolite at 773.83 m. These alteration styles are commonly found at amphibolite contacts. h) Sample IG_BH03_LG017 showing the association of biotite (bt), chlorite (ch), and iron oxide (interpreted as hematite (he)); crossed-polarized transmitted light. *Note this is not from the same interval as the hand sample in (g) but demonstrates the relationship commonly seen in thin section.

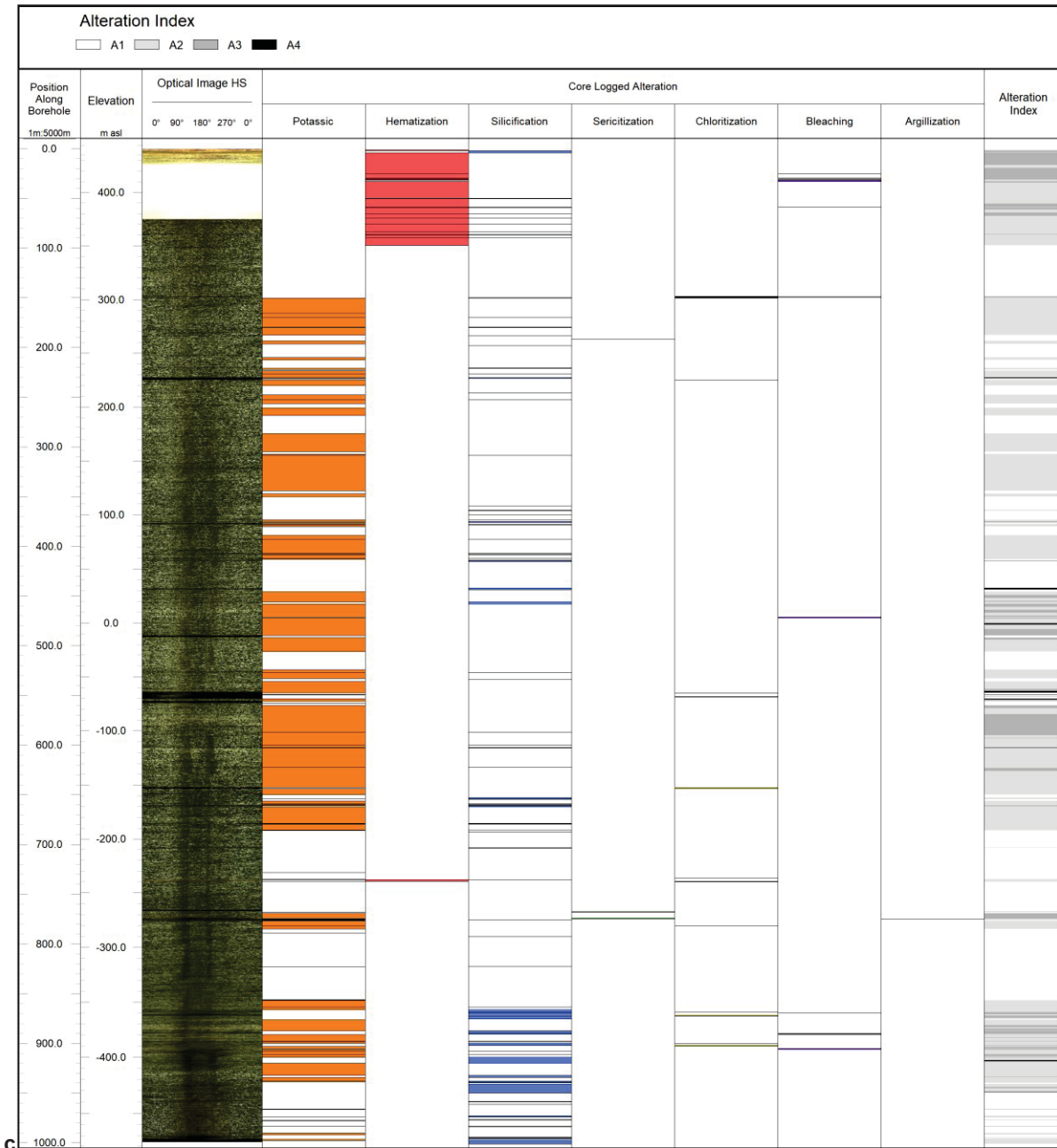


Figure 19: Alteration types and distribution along the borehole based on geological core logging and analysis of the optical televiewer log resulting in a final alteration log. A2 indicates intervals with slight alteration and A3 indicates intervals with moderate alteration.

3.2.3 Rock Unit Classification

Rock units (RU) are defined primarily on the basis of dominant rock type encountered within the borehole and the degree of subordinate rock types encountered in the interval. The core logged rock types, combined with key continuous geophysical datasets were used to distinguish distinct rock types within each RU, and defining the positions of top and bottom intervals. Using the available datasets, three RUs are defined within the borehole (Figure 20).

Rock Unit 1 (RU1) extends from the ground surface (0 m) to a position of 545.60 m along borehole. This interval predominantly consists of biotite granodiorite-tonalite making up 98.2 % of the interval (535.58 m), and an amphibolite, aphanitic and feldspar-phyric tonalite dykes, and aplite dykes making up the remaining 1.8 % of the interval. The single amphibolite unit occurs from 148.65 to 149.8 m along the borehole with sharp contacts dipping moderately towards the north. Throughout RU1 the biotite granodiorite-tonalite is massive, light grey to white in colour, and predominantly medium-grained. The majority of the hematite alteration is recorded in this interval, predominantly in the upper 100 m. The rest of the ca. 445 m is characterized by well-distributed “potassic” (potentially sericitization + weak hematization) alteration and minor occurrences of silicification and bleaching. With the exception of the upper ~80 m of the borehole, where casing is installed, the density, gamma and neutron logs exhibit relatively uniform profiles through this unit. The bottom of RU1 is marked by the presence of three amphibolite units logged over a 10 m interval, where the amphibolites mark the top of the next rock unit (RU2)

Rock Unit 2 (RU2) is 357.37m long extending from 545.60 m to 898.97 m along borehole and was primarily defined based on the increased presence of amphibolite units. This RU is composed primarily of medium-grained, massive, biotite granodiorite-tonalite that is light grey to white in colour making up 95.6 % of the interval (337.63 m) of the interval. The subordinate rock types make up the remaining 4.4 % of the interval comprising, several thin amphibolites, feldspar-phyric and aphanitic tonalite dykes, and granite dykes. The differentiating feature of this RU is the increased presence of ten discrete amphibolite units, consisting of 3 % (10.51 m) of the rock unit, characterized as dark green to grey in colour, fine-grained, and massive to strongly foliated. The alteration in this unit is still dominated by well-distributed “potassic” alteration and minor silicification; in contrast to RU1, there is a slight increase in logged chloritization. Despite the number of amphibolite units, their occurrences tend to cluster within two main zones. These zones of amphibolites show distinct peaks in the density log that are coincident with the logged amphibolites, and a sharp reduction in the neutron counts. Two narrow amphibolites occur near the base of the RU2 interval. Overall, the amphibolite contacts show similar geometry that are dipping shallowly to moderately towards the north, where foliation in the amphibolites are mainly concentrated along the contacts. Both the top and bottom of the RU2 interval are marked by the presence of amphibolite units, where the base of RU2 transitions into a rock unit devoid of logged amphibolites.

Rock Unit 3 (RU3) extends from 898.97 m to 1000.54 m along borehole which is dominated by biotite granodiorite-tonalite making up 98.6 % of its length. The remaining portion of this Rock Unit interval is composed of thin feldspar-phyric, granite, pegmatite and aplite dykes. These subordinate units account for 1.43 m of the 101.49 m interval (1.41 %). Similar to the other defined rock units, the main biotite granodiorite-tonalite is predominantly medium-grained and massive throughout this RU. This unit has well-distributed “potassic” alteration, similar to RU1 and RU2, but it also displays an increase in logged silicification and some minor bleaching toward the bottom of the borehole. Although this rock unit has similar rock types and geophysical log characteristics as RU1, in reviewing a magnetic susceptibility and bulk resistivity log, the RU3 interval displays some unique properties that are not present in the shallower parts of the borehole. Magnetic susceptibility and bulk electrical resistivity show a clear inflection point at a position of 940 m along borehole. The magnetic susceptibility profile shows an order of magnitude increase below the inflection point, which is also coincident with a reduction in the bulk electrical resistivity of the bedrock. Although this interval is not necessarily coincident with rock type or alteration observations in the core, it is suspected that this response corresponds to a subtle mineralogical variation, such as an increase in the amount of magnetic minerals. Despite this assumption, it not entirely clear what is causing this response and therefore this Rock Unit has not been separated into additional rock units.

Table 7 presents a summary of the final RU interpretations, classified according to the dominant rock type encountered therein. The final classification based both on the distribution of the

dominant rock types identified and catalogued in the final lithology log, and summarized in the RU descriptions above, suggest that the RUs can be classified in two dominant domains, including: (1) biotite granodiorite-tonalite, and (2) biotite granodiorite-tonalite with amphibolite.

Similarities observed between each of the RU descriptions, mainly dominant rock type, allow the RU intervals to be grouped by a common rock unit. Rock units RU1 and RU3, are dominated by biotite granodiorite-tonalite, exhibit similar geophysical signatures, and include few occurrences of subordinate rock types, allowing for the reclassification of these RUs as RU1a and RU1b. RU2 represents the only interval dominated by biotite granodiorite-tonalite with the presence of amphibolite units, allowing for singular classification as RU2.

Table 7: Summary of Classified Rock Units

Position Range (m)	RU#	Dominant Rock Type	Classified RU
0 – 545.60 m	RU1	Biotite granodiorite-tonalite	RU1a
545.60 m to 898.97 m	RU2	Biotite granodiorite-tonalite, with amphibolite	RU2
898.97 m – 1000.54 m	RU3	Biotite granodiorite-tonalite	RU1b

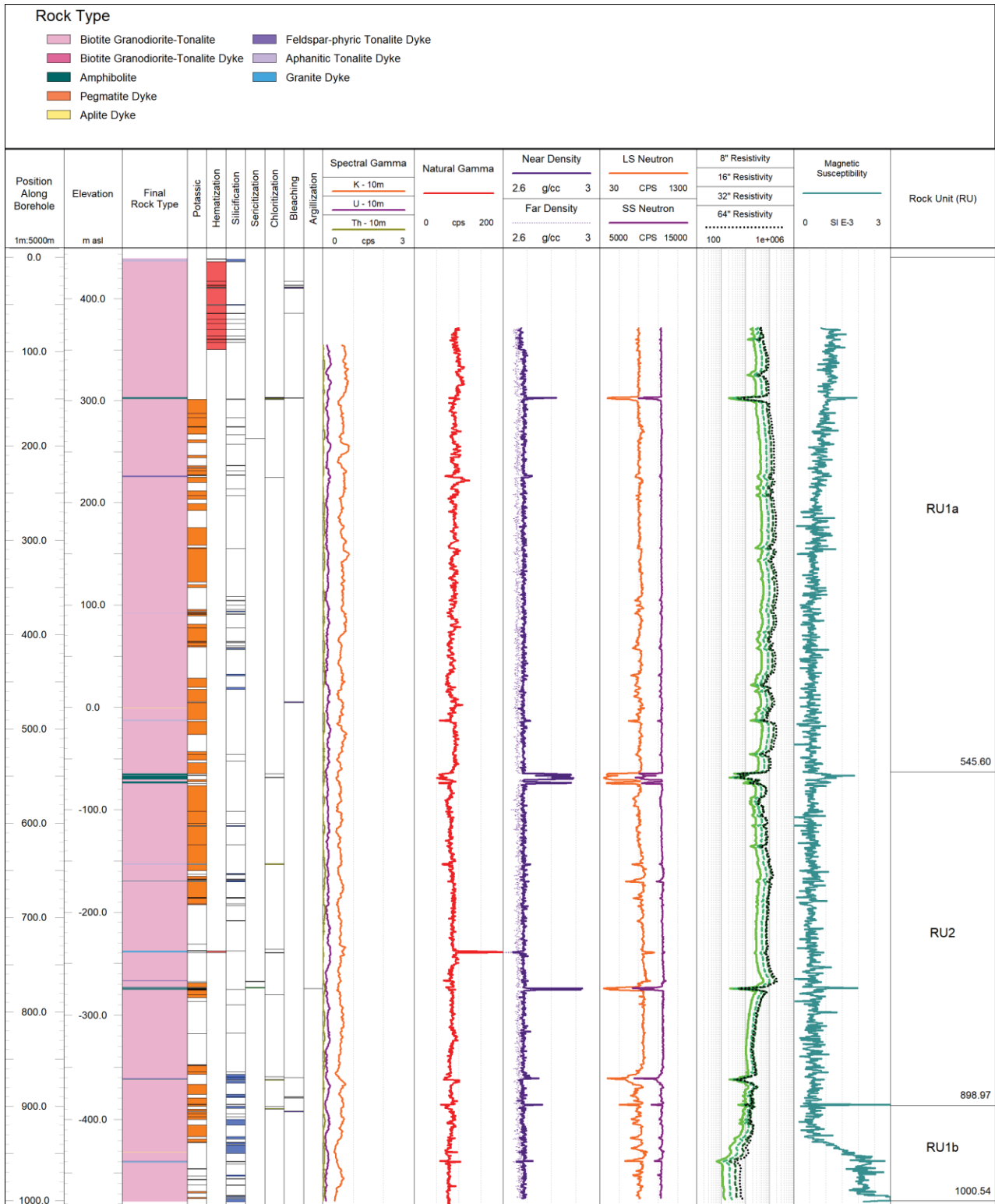


Figure 20: Summary of final logged rock type, alteration and key geophysical logs presented alongside interpreted rock units for IG_BH03.

The main uncertainty associated with this initial rock unit model is whether or not additional borehole information will fit within this same framework or if a completely different picture of the bedrock will emerge. Presently, RU2, comprises multiple similarly oriented amphibolite units dipping, on average, moderately towards the north-northwest, which are consistent with Rock Unit intervals defined in other drilled boreholes (e.g., IG_BH01 and IG_BH02). This unit may have similar enough characteristics to allow it to be correlated to similar rock units in adjacent boreholes. This possible correlation will be addressed in future site-scale geological modelling work.

3.2.4 Structural Interpretation

A description and interpretation of bedrock structural features measured along the borehole are presented in this section. Structural measurements include both geological and geotechnical characteristics captured during geological core logging and geophysical televiewer logging datasets, integrated together into a final structure log. The final integrated structure log contains 2286 natural features (Table 8). This total includes 2193 planar structures, of which 61 are defined as geological contacts between different rock types, and 93 linear structures. Of the total number of natural features, 1377 structures were logged and observed only during geological core logging, 742 structures were logged both in geological core logging and televiewer logging, and 167 structures were logged and observed only by televiewer. A total of 666 non-natural mechanical breaks were identified only during geological core logging which have already been separated from the dataset presented below.

During geological core logging, structures were oriented relative to an arbitrary reference line drawn along the length of the axis of each core run. The methodology for assigning true dip and dip direction to each logged structure, integrating the geological core logging information with the orientation information extracted from the televiewer log datasets, is presented in Appendix C. During this process of structural integration, 95 % of the features, including 2088 out of 2193 planar structures and all 93 linear structures, were oriented and assigned true dip and dip direction (true trend and plunge for linear structures). The remaining 105 (un-oriented) structures could not be assigned a true dip or dip direction as a result of being located within sections of the core that could not be corrected with the televiewer information. Oriented structural data are plotted by structure type and shown on equal area, lower-hemisphere stereographic projections (stereonet) throughout this section. Table 8 provides a summary of the results from the integration, presented by unique structure type.

Table 8: Summary of structures observed in the borehole.

Structure Type	Number of Oriented Structure			Total	Un-oriented Occurrences (Core Logged Only)	Total Structures Logged (n=1964)
	Core Logged Only	Both (Core and Televiewer)	Televiewer Logged Only			
Joint (JN)	853	400	135	1388	76	1464
Vein (VN)	255	123	20	398	15	413
Contact (CO)	10	49	0	59	2	61
Foliation (FO)	21	1	11	33	3	36
Igneous Primary Structure (IPS)	15	9	0	24	0	24
Shear Zones (SHR/SHRD)	55	40	0	95	1	96
Lineation (LIN) ²	32	61	0	93	0	93
Fault (FLT)	31	59	0	90	3	93
Broken Core Zone (BCZ)	0	0	0	0	4	4
Lost Core Zone (LCZ)	0	0	1	1	1	2
Total	1272	742	167	2181	105	2286

Borehole IG_BH03 was drilled at an inclination of -70° towards an azimuth of 180° , introducing a directional bias in the logging of planar structures (e.g., Terzaghi, 1965). To acknowledge this bias and begin to explore the implications of it, the presentation below includes Terzaghi-weighted contoured stereonet along with the unweighted data for all structures except for oriented lithological contacts. The legend associated with each of the weighted stereonet indicates the number of features expected based on the Terzaghi weighting. The minimum bias angle applied for this analysis, using the software DIPS© (Version 7) by Rocscience, is 15° . A summary of orientation information for all 2088 naturally occurring planar structures is presented in Figure 21.

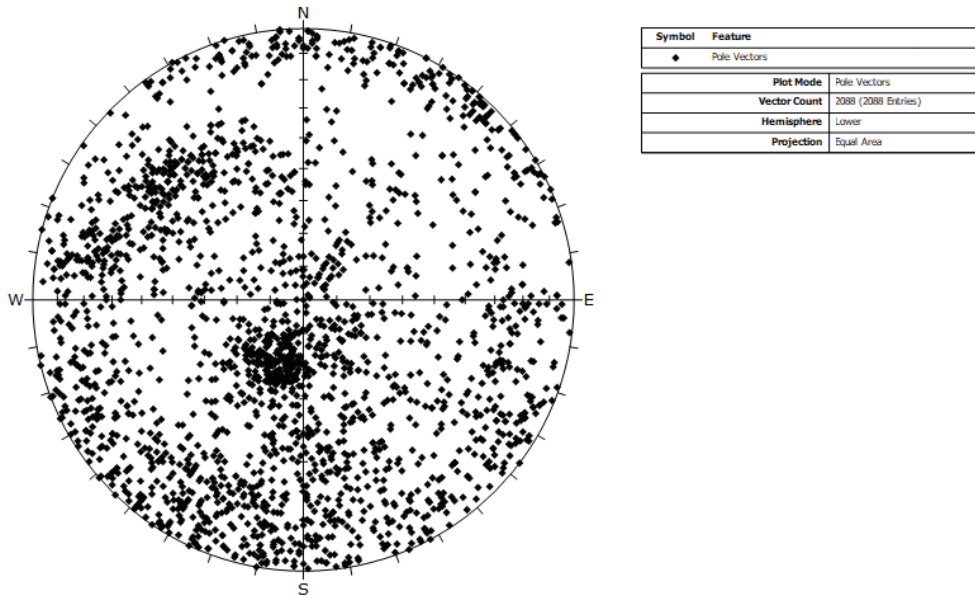


Figure 21: Equal Area Lower Hemisphere Projections (stereonet) showing poles to planar structural measurements, unweighted (n = 2088).

In comparing the unweighted and Terzaghi-weighted contours, in Figure 22, it is clear that the latter emphasizes the pole clusters of steeper dipping structures orientated at a low angle to the core axis and de-emphasizes the gentlest dipping structures orientated at a high angle to the core axis.

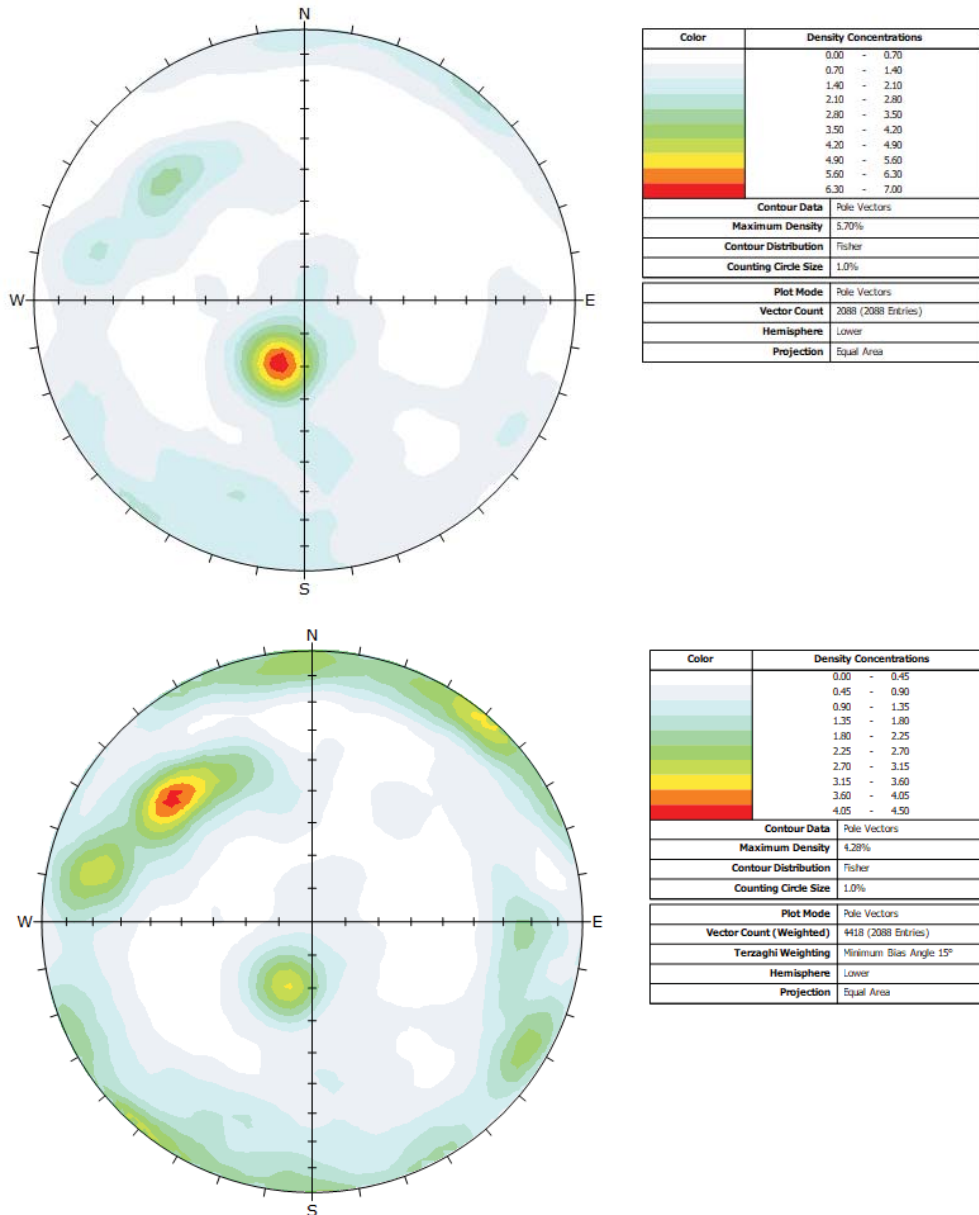


Figure 22: Equal Area Lower Hemisphere Projections (stereonet) showing density contours of the poles to all planar structural measurements. Top: all data – contours, unweighted (n = 2088). Bottom: all data – contours, Terzaghi-weighted.

More recently, advanced procedures for addressing orientation bias have been reported in the literature (e.g., Davy et al., 2006). However, such alternative approaches require not yet available information such as fractures size-distribution for each orientation set. The use of such methods will be made possible, and justified, as additional borehole and surface structural information become available.

3.2.4.1 Structures

The structural information presented below includes discussion of features logged as primarily igneous structures, contacts, ductile structures, brittle structures, including joints, veins and faults, and linear structures.

Primary Igneous Structures

Primary igneous structures include features interpreted to have originated with the formation or emplacement of the igneous rock, including igneous flow foliation and igneous layering. For IG_BH03, a total of 24 primary igneous structures were identified. These features are generally characterized by sharp to gradational changes in grain size or concentration of the main rock forming minerals in the granodiorite-tonalite bedrock, including, biotite, quartz or plagioclase. The transitions that define these occurrences were observed to be weak in 21 of the occurrences. However, all occurrences were intact in the core and all occurrences were successfully oriented. The thicknesses of the primary igneous structures range from mm-scale to a maximum of 25 cm. One feature in the core identified as primary igneous layering is shown on Figure 27a. An alternative interpretation is that the feature shown is an example of mafic schlieren. The true nature of all features logged as primary igneous structures will continue to be assessed as additional information from future boreholes becomes available. Figure 23 presents the stereographic projection of all igneous primary structures, showing significant scatter in their orientations and no clear clustering of poles. There is, however, an overall tendency for planes to dip easterly rather than westerly.

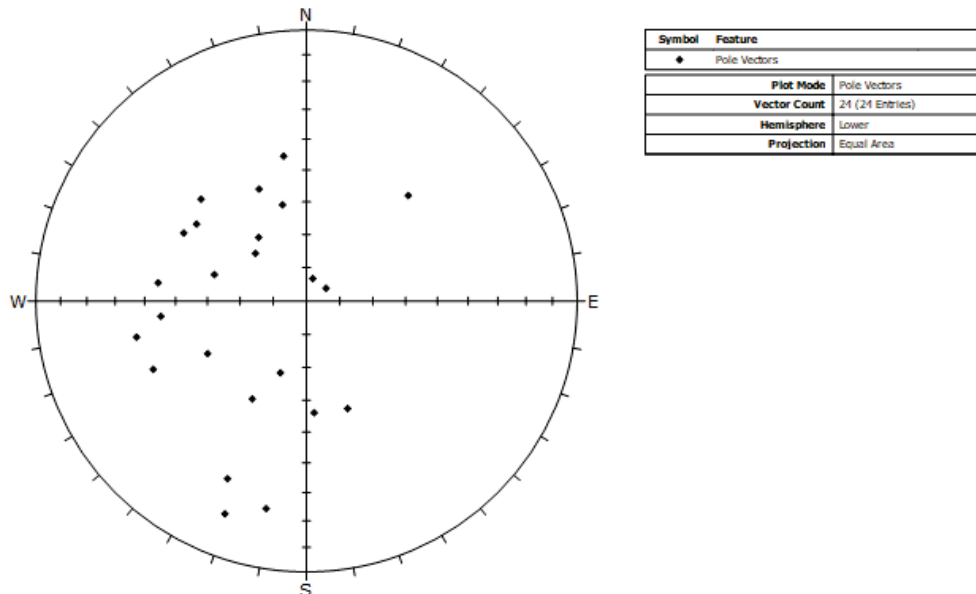


Figure 23: Stereonet showing poles to the planes of Primary Igneous Structures (IPS; n = 24).

Contacts

Top and bottom contact orientations were logged for each change in rock type wherever the transition was sharp enough to confidently identify a contact plane, including a total of 61 instances in IG_BH03. All of the logged geological contacts represent transitions between occurrences of biotite granodiorite-tonalite and subordinate rock types, except in one instance where an amphibolite was logged adjacent to a feldspar-phyric dyke. A total of 59 of the geological contacts were identified as sharp boundaries. In addition, one contact between biotite granodiorite-tonalite

and an aplite dyke was described as gradational and one contact between biotite granodiorite-tonalite and a tonalite dyke was described as having a sharp and chilled margin.

A total of 59 of the geological contacts could be oriented. The two instances where geological contacts could not be oriented were near-surface occurrences, less than five metres deep in the borehole, where televiewer data was not able to be collected. The poles to the planes defining all oriented geological contacts are shown in Figure 24. One prominent pole cluster defines steeply northeast-dipping geological contacts. The majority of the remaining contacts dip moderately or gently towards the north.

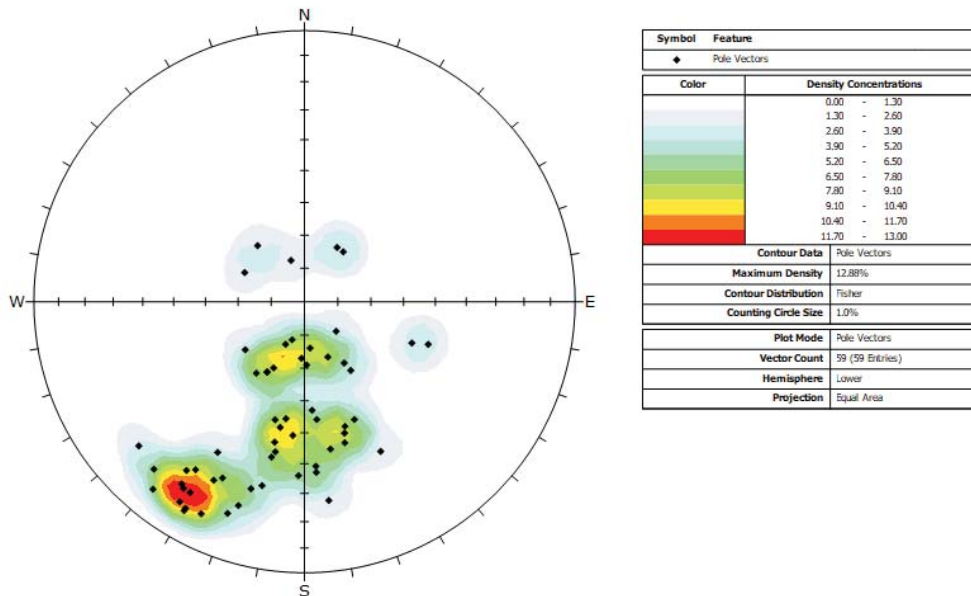


Figure 24: Stereonet showing poles and unweighted contours for all geological contacts (n = 59).

Amphibolite was logged in 11 intervals in the borehole and all of its geological contacts (top and bottom contacts) were oriented (Figure 25), including six instances identified as broken and 16 identified as intact. Too few data are available to merit contouring of the poles to the amphibolite contacts. One subset of two poles (one amphibolite occurrence) defines steeply northeast-dipping contacts and the majority of the remaining amphibolite contacts dip moderately or gently towards the north. In addition, two adjacent poles defined one amphibolite occurrence that dips gently towards the southeast. All amphibolite contacts were described as sharp, defining distinct transitions with the adjacent rock. The amphibolite occurrences generally exhibit evidence of penetrative ductile to brittle-ductile deformation obscuring any indication of their primary relationship with the surrounding bedrock. The deformation manifests as cm- to dm-scale localized shear zones that are developed along, and sub-parallel to, their contacts. A comparison of the amphibolite contact orientations and shear zone orientations, the latter shown below in Figure 30, highlights this relationship.

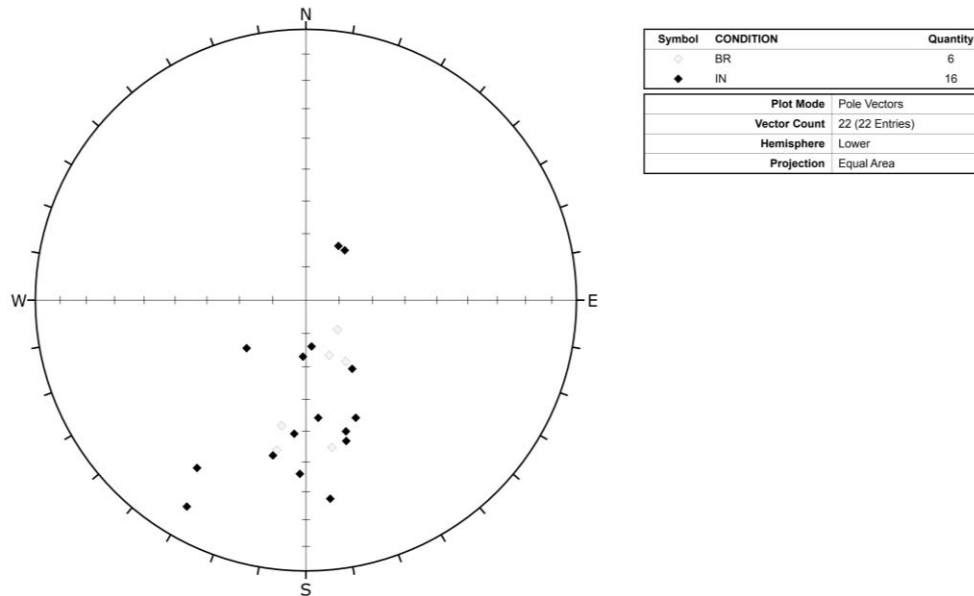


Figure 25: Stereonet showing poles to oriented amphibolite contacts (n = 22). Open symbols identify broken contacts (CO-BR) and filled symbols identify partially intact/intact contacts (CO-PIN/IN).

The poles to the contact orientations for the felsic phases interpreted as dykes are shown on Figure 26. This includes occurrences of aphanitic and felspar-phyric tonalite dykes, aplite dykes, granite dykes, biotite granodiorite-tonalite dykes, and pegmatite dykes. Poles to aphanitic tonalite dyke contacts (n = 6), identified by light purple diamonds, define two occurrences that dip steeply towards the northeast and another one that dips gently towards the north-northeast. All aphanitic tonalite dyke contacts were logged as sharp, and none were identified as broken. Poles to aplite dyke contacts (n = 8), identified by yellow diamonds, define occurrences that dip moderately towards the north-northeast, north and northwest. All aplite dyke contacts were logged as sharp, and none were identified as broken. Poles to granite dyke contacts (n = 4), identified by blue diamonds, define occurrences that dip steeply towards the northeast. All granite dyke contacts were logged as sharp, and none were identified as broken. Poles to biotite-granodiorite tonalite dyke contacts (n = 4), identified by pink diamonds, define occurrences that dip moderately towards the north-northeast and gently towards the southeast. All biotite-granodiorite tonalite dyke contacts were logged as sharp, and none were identified as broken. Poles to feldspar-phyric tonalite dyke contacts (n = 14), identified by dark purple diamonds, define occurrences that are steeply inclined and dip northeast, occurrences that dip moderately to gently north and occurrences that dip gently to the south. All feldspar-phyric tonalite dyke contacts were logged as sharp, and none were identified as broken. Poles to pegmatite dyke contacts (n = 2), identified by orange diamonds, define one steeply inclined occurrence that dips northeast. Both pegmatite dyke contacts were logged as sharp, and none were identified as broken. Notably, the overall distribution of poles to the felsic dyke phases, shown in Figure 26, is very similar to the distribution of poles to the amphibolites, shown in Figure 25.

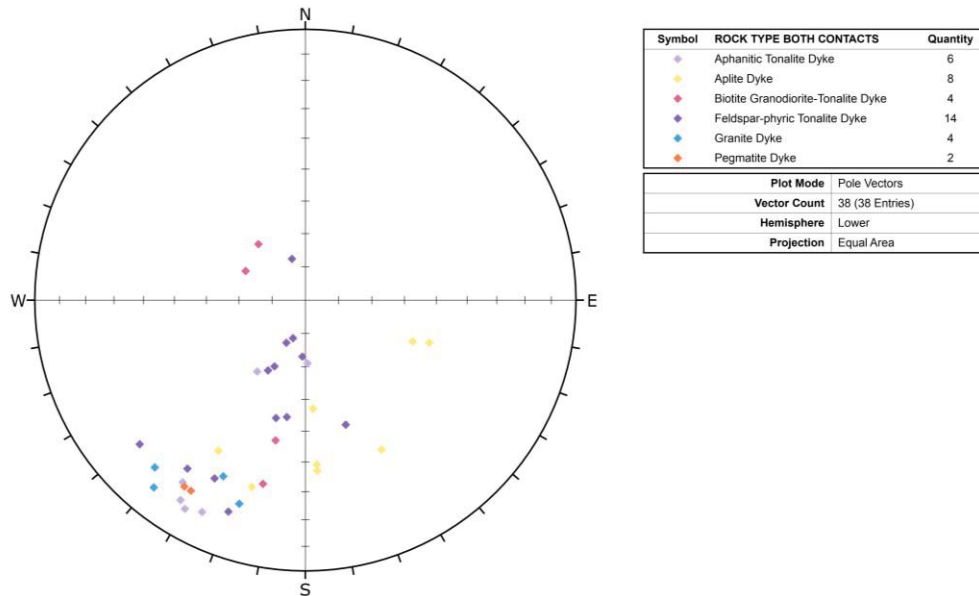


Figure 26: Stereonet showing the distribution of poles to the contacts of logged felsic dykes (n = 38), including, aphanitic tonalite dykes (n= 6), aplite dykes (n = 8), biotite granodiorite-tonalite dykes (n = 4), feldspar-phyric tonalite dykes (n = 14), granite dykes (n = 4), and pegmatite dykes (n = 2).

Ductile Structures

Ductile structures identified in IG_BH03 include foliation (FO) and shear zones (SHR). Examples of these structures are shown in Figure 27b and Figure 27c. Stick plots indicating the distribution of the ductile structures are included in Figure 28. Figure 28 also includes the overall per metre fracture frequency and stick plots for all brittle structures logged in the borehole. The brittle structures will be described in detail after presentation of the ductile structures.

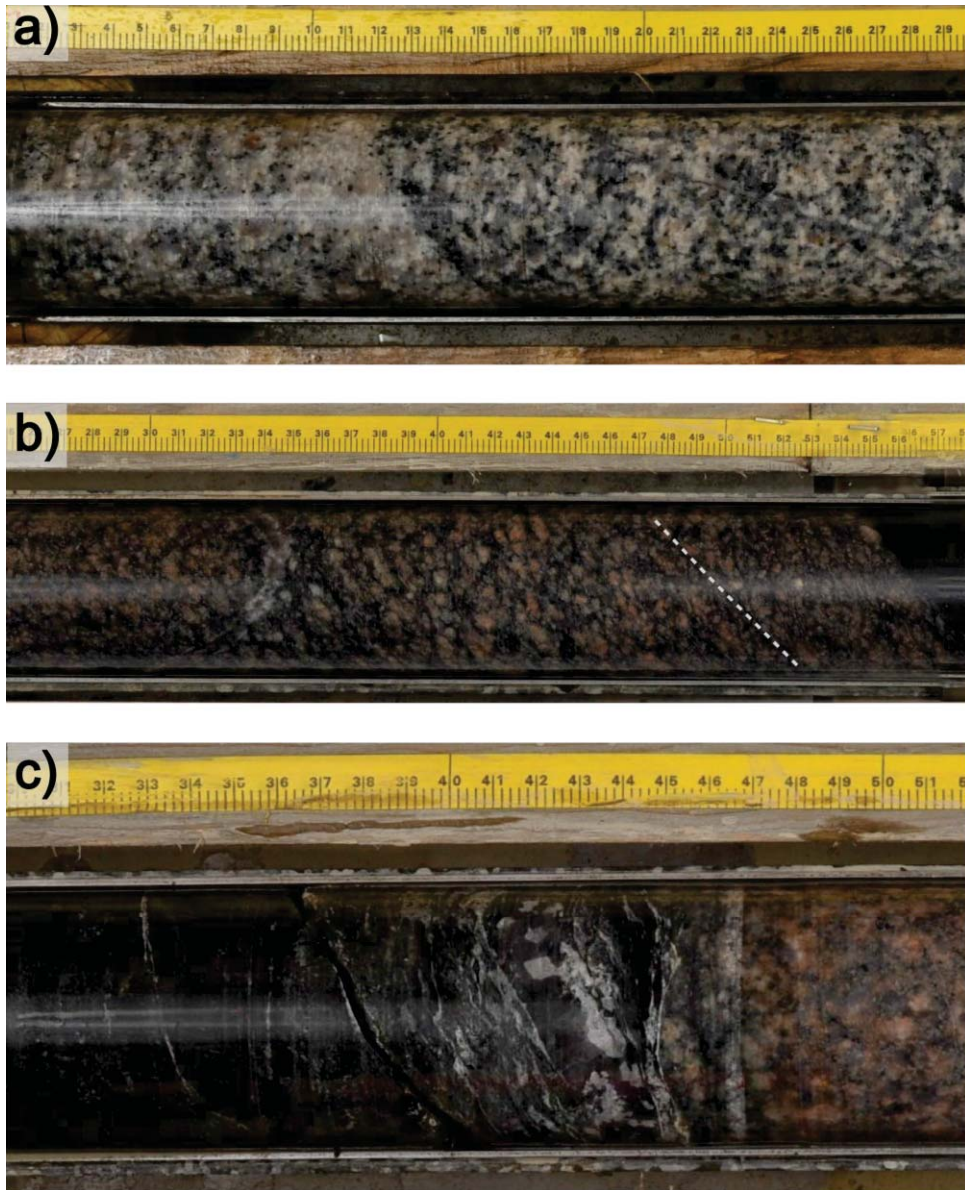


Figure 27: Examples of primary igneous and ductile structure in IG_BH03: a) A change in biotite concentration interpreted as primary igneous layering in biotite granodiorite-tonalite (158 m along borehole). b) Muscovite and biotite-defined foliation trending at a moderate angle to the core axis, parallel to the white dashed line, in a small interval of biotite granodiorite-tonalite between two amphibolites (548 m along borehole). c) Shear zone developed at a moderate angle to the core axis within and along the margin of amphibolite at its contact with biotite granodiorite-tonalite (553 m along borehole).

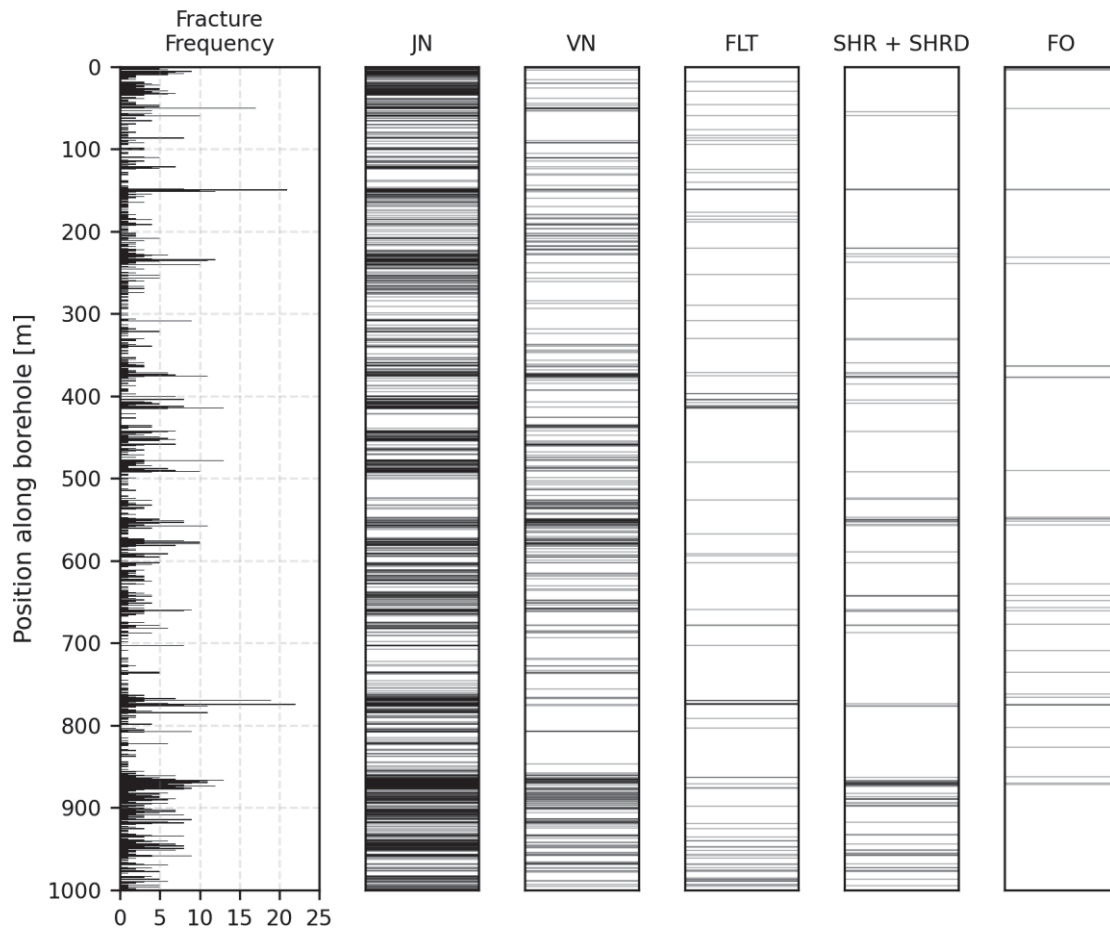


Figure 28: Summary log showing the frequency per metre of brittle structures (left) in comparison to stick plots that show the distribution of all brittle structures (Joints – JN, Veins – VN and Faults - FLT) and all ductile structures (Shear Zones – SHR + SHRD and Foliation – FO).

A total of 36 occurrences of foliation were recorded where preferential orientation of mineral grains was observed. The majority of occurrences of foliation were identified between approximately 650 and 875 m along borehole, with evidence of one additional slightly denser cluster of foliations at around 550 m along borehole (Figure 28). The foliation is described as weakly developed and is characterized by the preferred alignment of biotite. An example of well-developed foliation is shown in Figure 27b. Figure 29 presents the stereonet of poles to foliation orientations. Three foliation occurrences could not be oriented because they occur about five m along the borehole, within the region of the borehole covered by the surface casing. The remaining 33 foliation occurrences exhibit a large degree of scatter in their pole distribution. One main pole cluster defines moderately north dipping foliation planes. Steeply north-dipping and steeply east-dipping foliation planes are slightly less prominent. The Terzaghi-weighted contours emphasizes the pole cluster of the steeply east-dipping foliation.

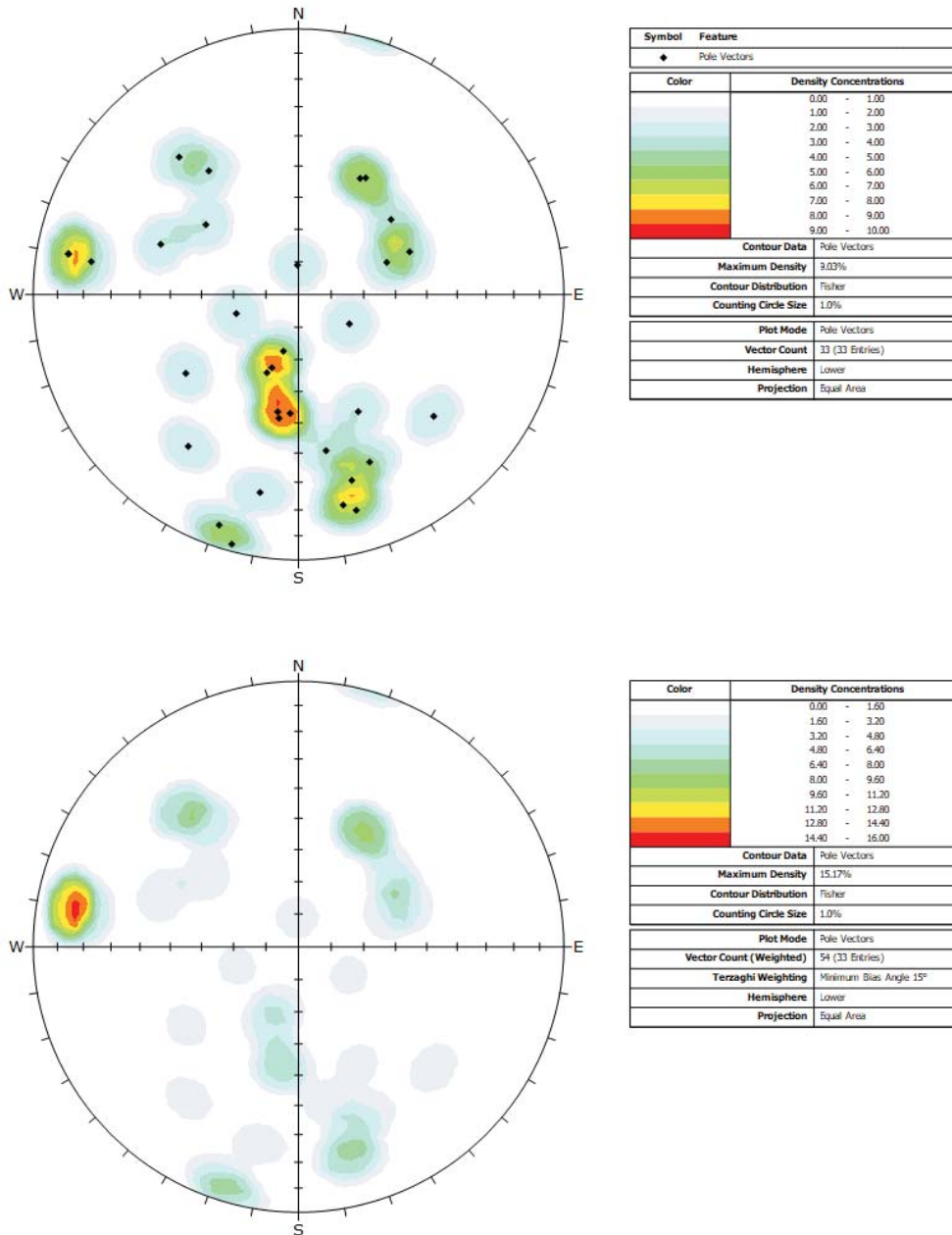


Figure 29: Stereonets showing orientation information for Foliation (FO). Top: All data – poles and contours, unweighted (n = 33). Filled symbols identify partially intact/intact Foliation (FO-PIN/IN). Bottom: All Foliation data, Terzaghi-weighted contours (n = 54).

A total of 96 shear zones were logged in IG_BH03. These structures were initially identified during geological core logging as either ductile or brittle-ductile shear zones. In assessment of the entire shear zone dataset, it was determined that all occurrences more likely represent a continuum of ductile to brittle deformation. Therefore, the presentation herein integrates all occurrences simply as a single shear zone dataset. A typical shear zone example is shown in Figure 27c. Fifty-five of the shear zones are identified in geological core logging only (57 %), with the remaining shear zones identified in both geological core logging and televiewer logs (43 %); 95 of the 96 (99 %) shear zones were successfully oriented. The shear zones range in width (length along core axis)

from hairline to 164 cm. The most common mineral phase associated with shear zones is quartz, with lesser associations of chlorite, epidote, calcite, biotite, plagioclase and alkali-feldspar. Shear zones are commonly observed along the contacts of amphibolite occurrences and, in some cases, feldspar-phyric felsic dykes. Some occurrences are also identified within the biotite granodiorite-tonalite away from these subordinate rock types. The stick plot of shear zone occurrences highlights the observation that they are identified along the entire length of the borehole. There is, however, one relatively distinct cluster of shear zones logged below 850 m along borehole (Figure 28). Figure 30 presents the unweighted and weighted stereonet for all oriented shear zones (95/96; 99 %). One prominent pole cluster in the unweighted dataset defines gently inclined shear zones that dip north-northeast to north. The Terzaghi-weighted dataset emphasizes the same pole cluster and also emphasizes near-vertical shear zones that strike northwest, west and southwest.

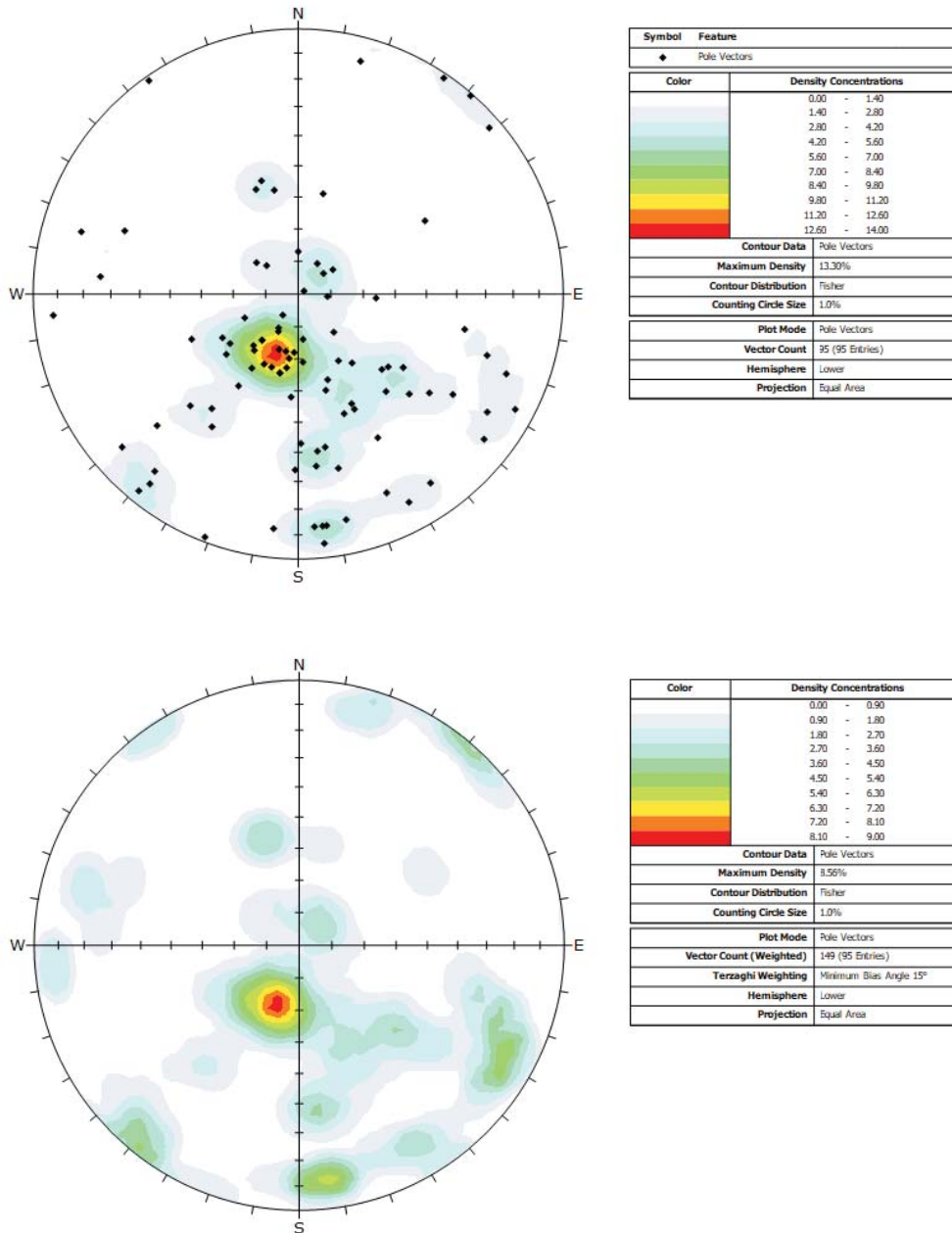


Figure 30: Stereonets showing orientation information for Shear Zones (SHR). Top: All data – poles and contours, unweighted (n = 95). Open symbols identify broken Shear Zones (SHR-BR) and filled symbols identify partially intact/intact Shear Zones (SHR-PIN/IN). Bottom: All Shear Zone data, Terzaghi-weighted contours (n = 149).

Brittle Structures

This section describes the brittle structures, including all joints (JN), veins (VN), and faults (FLT), representing the group of features collectively identified as fractures. A summary of the per metre fracture frequency for all brittle structures, as well as stick plots detailing their distribution in the borehole, is included in Figure 28. Typical examples of brittle structures identified in the borehole are included in Figure 31.

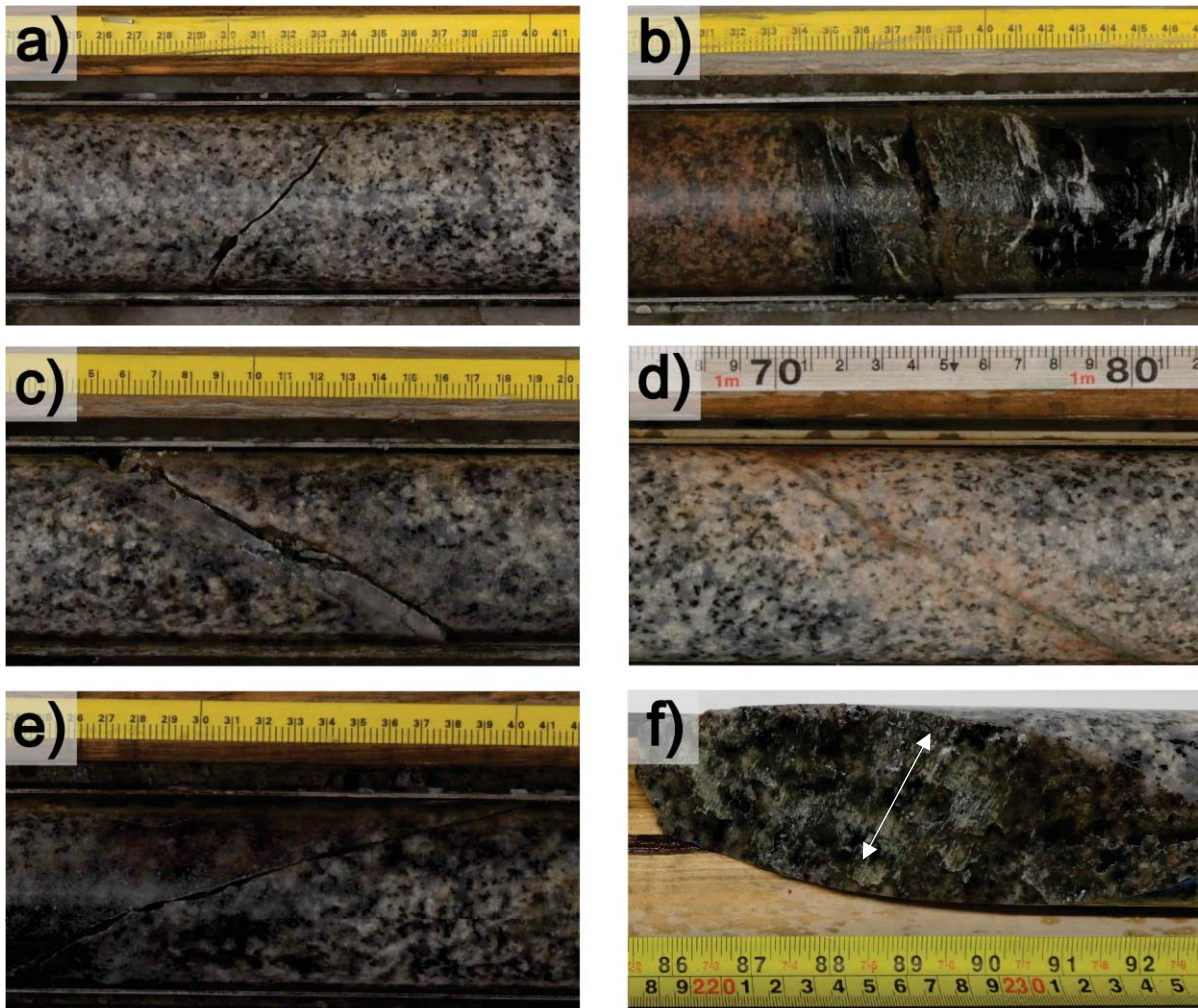


Figure 31: Examples of brittle structures observed in IG_BH03: A) A broken, clean, hairline (no visible geological aperture) joint in biotite granodiorite-tonalite (403 m). B) A broken joint with soft gouge-like infill and a geological aperture of 17 mm in amphibolite (547 m). C) A broken, mm-scale quartz vein in biotite granodiorite-tonalite (460 m). D) An intact, mm-scale epidote vein in biotite granodiorite-tonalite with associated alteration (883 m). E) A broken fault with 2 mm geological aperture and an associated cm-scale halo of sericitization in biotite granodiorite-tonalite (375 m). F) A lineation defined by aligned quartz (parallel to white arrow) on broken fault plane in biotite granodiorite-tonalite (83.5 m).

A total of 1464 joints were logged in IG_BH03. They are distributed along the entire length of the borehole and since they dominate the total brittle structure dataset the peaks in the per metre fracture frequency correlate well with the clusters evident in the stick plot of all joints (Figure 28). A total of 189 joints (13 %), were logged as broken, while the remaining 1275 (87 %) were logged as intact or partially intact. The majority of the logged joints (1429; 98 %) were logged with no visible geological aperture. In the remaining 35 occurrences, mm-scale geological apertures (maximum of 17 mm) were observed. Joint surfaces were logged as clean, with no associated mineral infill, in 217 occurrences (15 %), while the remaining 1247 (85 %) included observation of staining, slight alteration, or coated with a mm-scale infill. The most common mineral phases associated with the joints were quartz, calcite, chlorite, iron oxide (hematite), and epidote.

Typical examples of joints are shown in Figure 31a-b, one clean hairline joint with no visible geological aperture (Figure 31a) and one broken joint with a soft gouge-like infill and mm-scale geological aperture in amphibolite (Figure 31b). The majority of identified joints were logged in geological core logging only (929; 63 %), or in both geological and televiewer logging (400; 27 %).

The remaining 135 joints (9 %) were identified in televiewer logging only. 1388 joints (95 %) were successfully oriented. Figure 32 presents the unweighted and weighted stereonet for all oriented joints. The unweighted dataset emphasizes one pole cluster that defines gently north-northeast to north dipping joints. While no other prominent pole clusters are evident in the unweighted dataset, the majority of the remaining poles indicate that joints are steeply inclined and dip in multiple directions. Pole clusters in the Terzaghi-weighted dataset define near vertical joints that strike northwest, northeast and east-west, as well as steeply inclined joints that dip east-southeast.

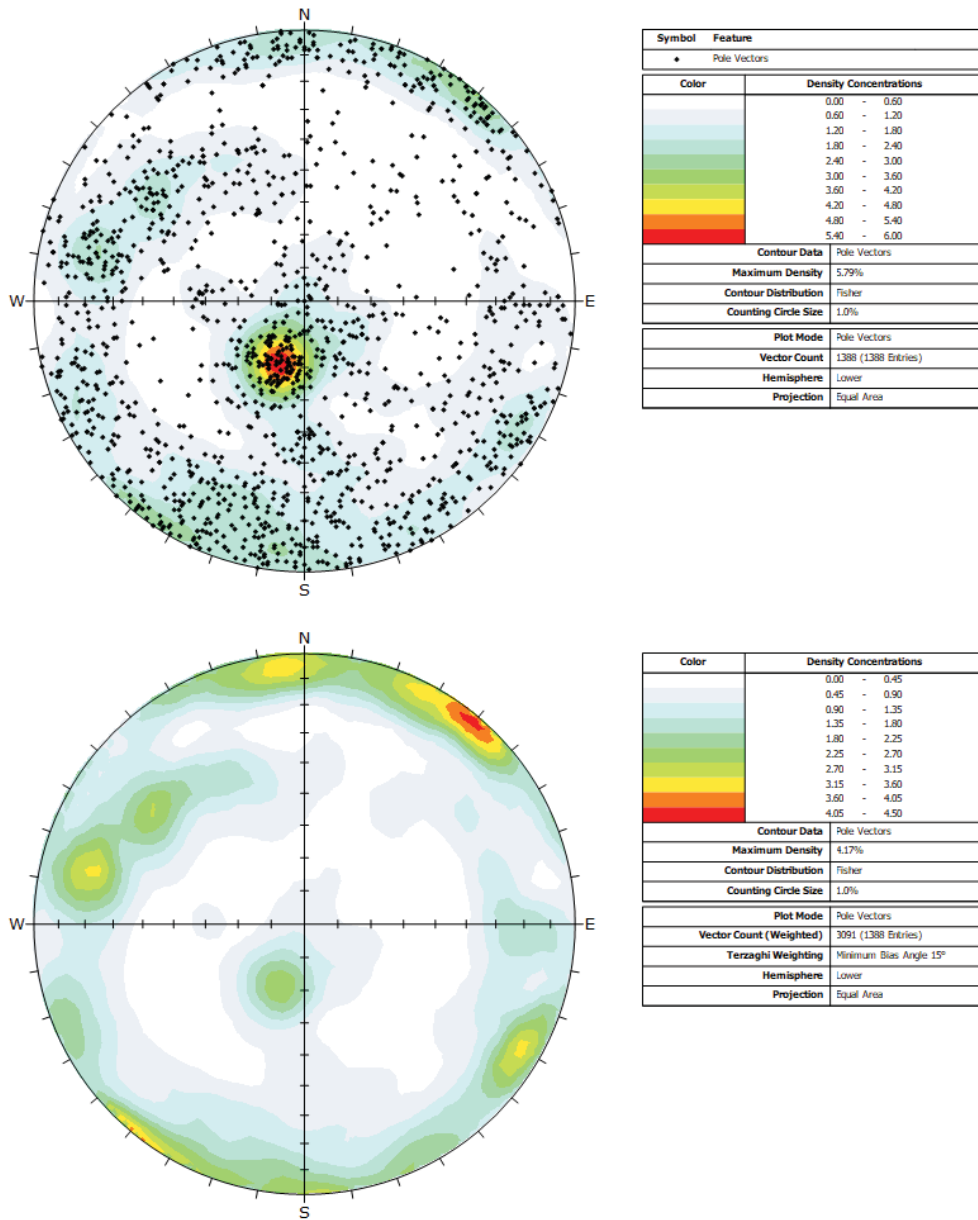


Figure 32: Stereonets showing orientation information for Joints (JN). Top: All data – poles and contours, unweighted (n = 1388). Open symbols identify broken Joints (JN-BR) and filled symbols identify partially intact/intact Joints (JN-PIN/IN). Bottom: All Joint data, Terzaghi-weighted contours (n = 3091).

A total of 413 veins were logged in IG_BH03. The majority of the veins (407; 99 %) were logged as intact or partially intact and the remaining six vein occurrences were logged as broken. The stick plot of vein occurrences highlights the observation that veins are identified along the entire length of the borehole, including higher density intervals between approximately 350 and 700 m and below 850 m (Figure 28). A total of 270 veins (65 %) were identified in geological core logging and another 123 (30 %) were identified in both geological and televiewer logging. In these instances, at least one vein mineral phase or mineral assemblage was identified. A total of 20 veins (5 %) were identified only in the televiewer dataset. In these later occurrences, the infilling mineral could not be determined with certainty. The main mineral infilling phase identified was quartz which was logged in 322 veins (78 %; Figure 31c), followed by epidote in 59 veins (14 %; Figure 31d), calcite in 47 veins (11 %), chlorite in 38 veins (9 %) and a 'granitic' assemblage of alkali feldspar +/- plagioclase

+/- biotite +/- quartz in 22 occurrences (5 %). Logged vein thicknesses range between hairline (sub-mm) and 5 cm. A total of 398 (96 %) veins were successfully oriented. Figure 33 presents the unweighted and weighted stereonet for all oriented veins. Two main pole clusters are evident in the unweighted dataset defining veins that dip gently towards the north or north-northeast and veins that dip moderately towards the southeast. Less prominent pole clusters indicate subvertical veins that strike northwest and steeply and moderately inclined veins that dip towards the east and west-northwest, respectively. The Terzaghi-weighted dataset emphasizes the pole cluster to the moderately inclined veins that dip towards the southeast. The less prominent pole clusters in the weighted vein dataset use in the unweighted vein dataset.

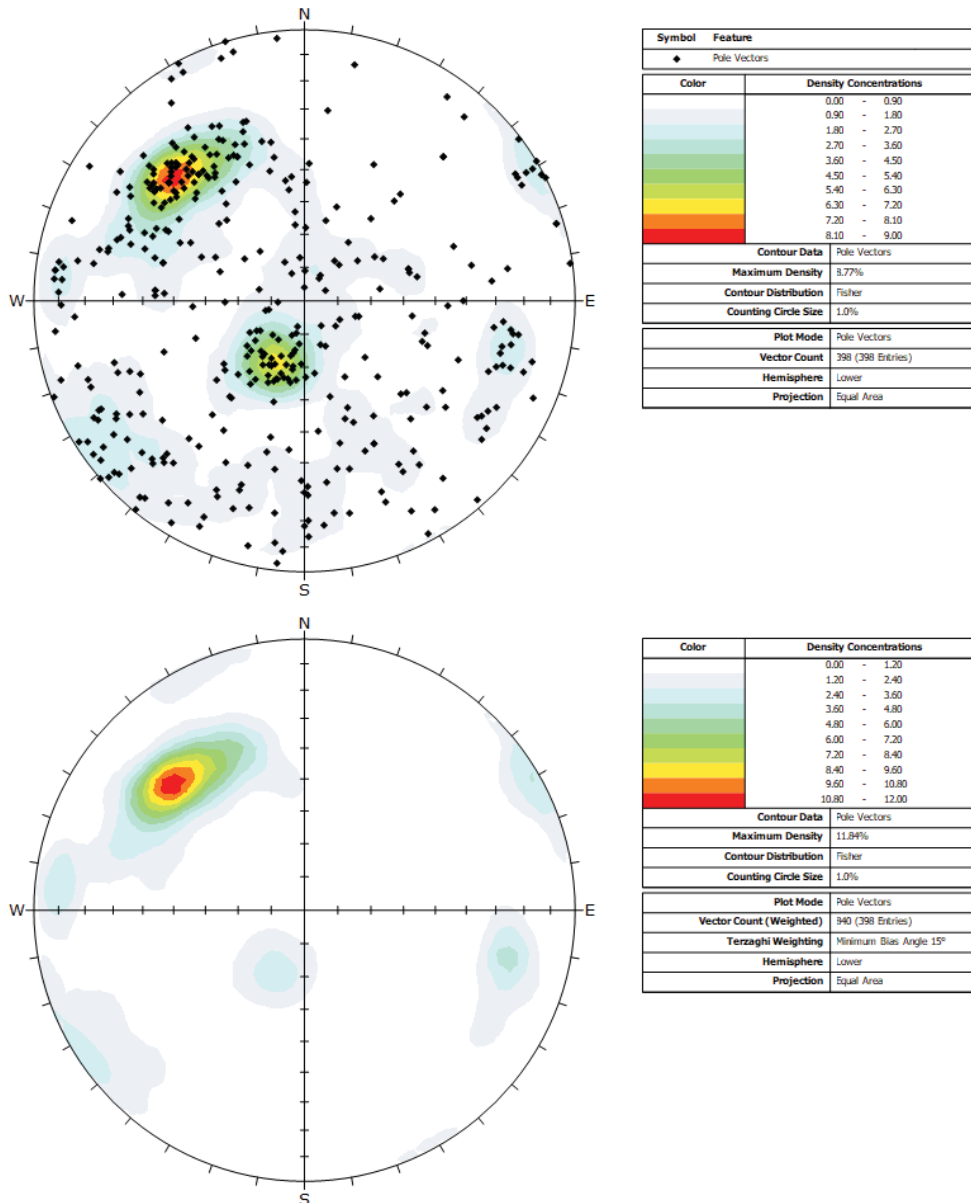


Figure 33: Stereonets showing orientation information for all Veins (VN). Top: All data – poles and contours, unweighted (n = 398). Open symbols identify broken Veins (VN-BR) and filled symbols identify partially intact/intact Veins (VN-PIN/IN). Bottom: All Vein data, Terzaghi-weighted contours (n = 840).

Faults include features interpreted to have resulted from brittle deformation and exhibit some evidence of displacement. A total of 93 faults were logged in IG_BH03. The stick plot highlights the observation that faults are distributed along the entire length of the borehole, with distinct clusters at approximately 400 m along borehole and below 850 m along borehole (Figure 28). The main diagnostic criterion used to identify a fault in the recovered core include the presence of slickenlines on the fault surfaces. In 82 (88 %) of the logged faults, the surface was recorded as a hairline structure with no geological aperture. The largest measured geological aperture across a fault was 16 mm. Common mineral phases identified on fault surfaces were chlorite, quartz, calcite, epidote, iron stain and clay or soft or hard gouge. Some typical examples of a faults are shown in Figure 31e and f, highlighting the observation that the majority of faults in IG_BH03 are very narrow and discrete structures with only slight evidence of damage in the rock surrounding the fault plane (in Figure 31e, a sericitization halo around the fault). Figure 31f shows a fault plane with slickenlines defined by quartz. In this occurrence, the lineation plunges shallowly in the fault plane suggesting near horizontal (transcurrent) movement. Additional information related to the orientation of lineations is included in the next subsection. 59 of the faults were identified in both geological and televiewer logging (63 %), with the remaining 34 faults observed in geological core logging only (37 %). 90 (97 %) of the faults were successfully oriented. Figure 34 presents the unweighted and weighted stereonet for all faults. One main pole cluster is evident in the unweighted dataset defining faults that dip gently towards the north or north-northeast. Less prominent pole clusters indicate subvertical faults that strike northwest or east, steeply inclined faults that dip west or east-southeast and moderately inclined veins that dip north-northeast to northeast and southeast. The Terzaghi-weighted dataset emphasizes the steeply inclined and west-dipping faults. The less prominent pole clusters in the weighted fault dataset overlap with those in the unweighted fault dataset.

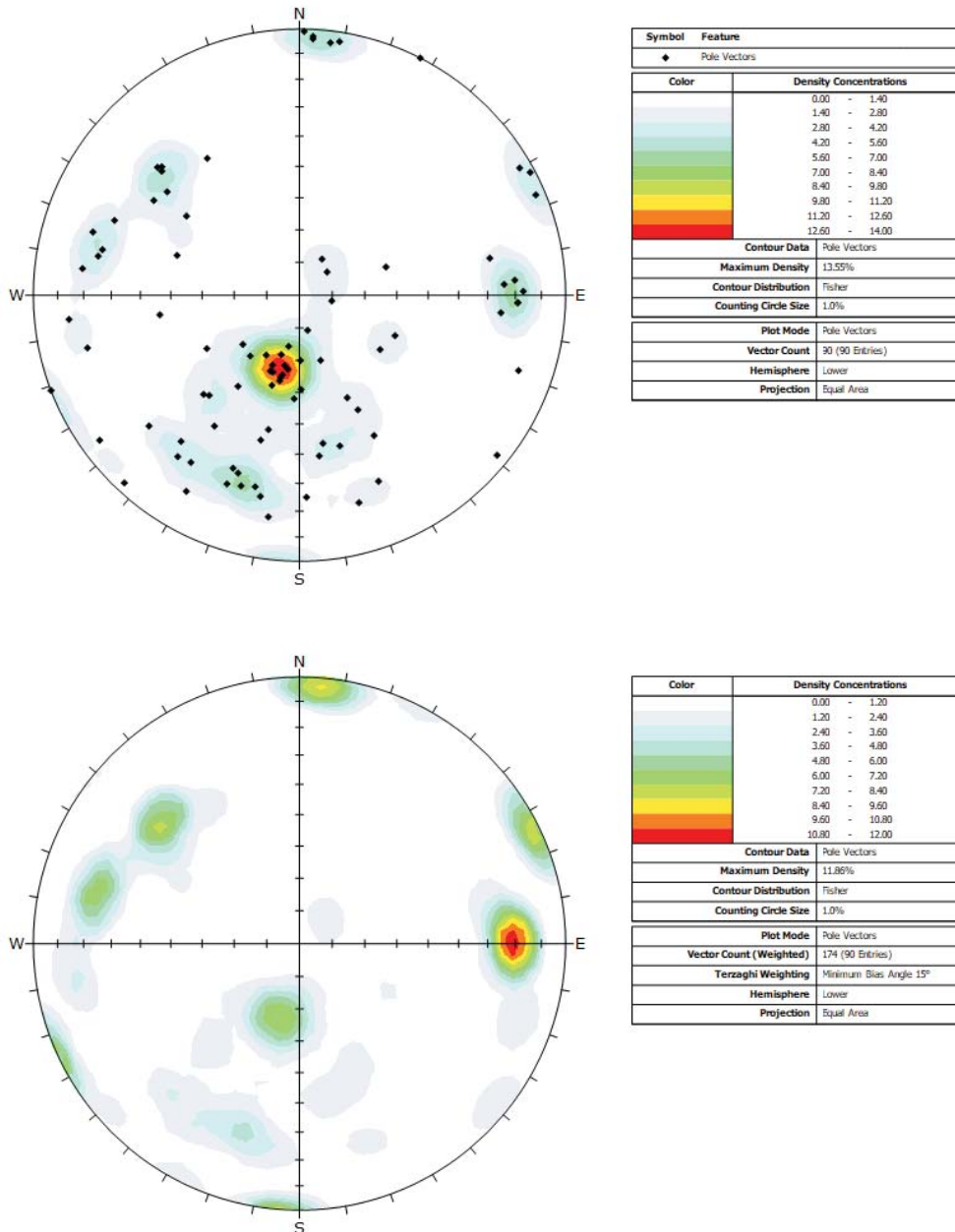


Figure 34: Stereonets showing orientation information for Faults (FLT). Top: All data – poles (n = 90). Bottom: All Fault data, Terzaghi-weighted contours (n = 174).

Lineations

A total of 93 lineations were identified during geological core logging, including 87 occurrences identified on fault planes, five occurrences on shear planes and one additional occurrence identified on a foliation plane (Figure 35). The majority of lineations plunge shallower than 40° and primarily into the northwest quadrant, with two main clusters that plunge shallowly towards the northwest and north. An additional cluster of lineations plunges shallowly towards the east. The cluster of northwest-plunging lineations are identified primarily on planes that dip gently towards the north-northeast or on near-vertical planes that strike northwest. The cluster of north-plunging lineations

are identified primarily on planes that dip shallowly to the north-northeast or dip steeply to the east-southeast. The cluster of east-plunging lineations are identified primarily on planes that dip steeply to the south.

Most lineations identified during visual core logging are characterized as slickenlines. The identified mineral assemblage on the lineated planes includes some combination of quartz, chlorite, epidote with lesser occurrences of muscovite, iron staining and soft fault gouge. The one lineation identified on a foliation plane, with a nearly horizontal plunge towards the southwest, is identified as a hornblende mineral lineation. The lineations identified on the shear planes.

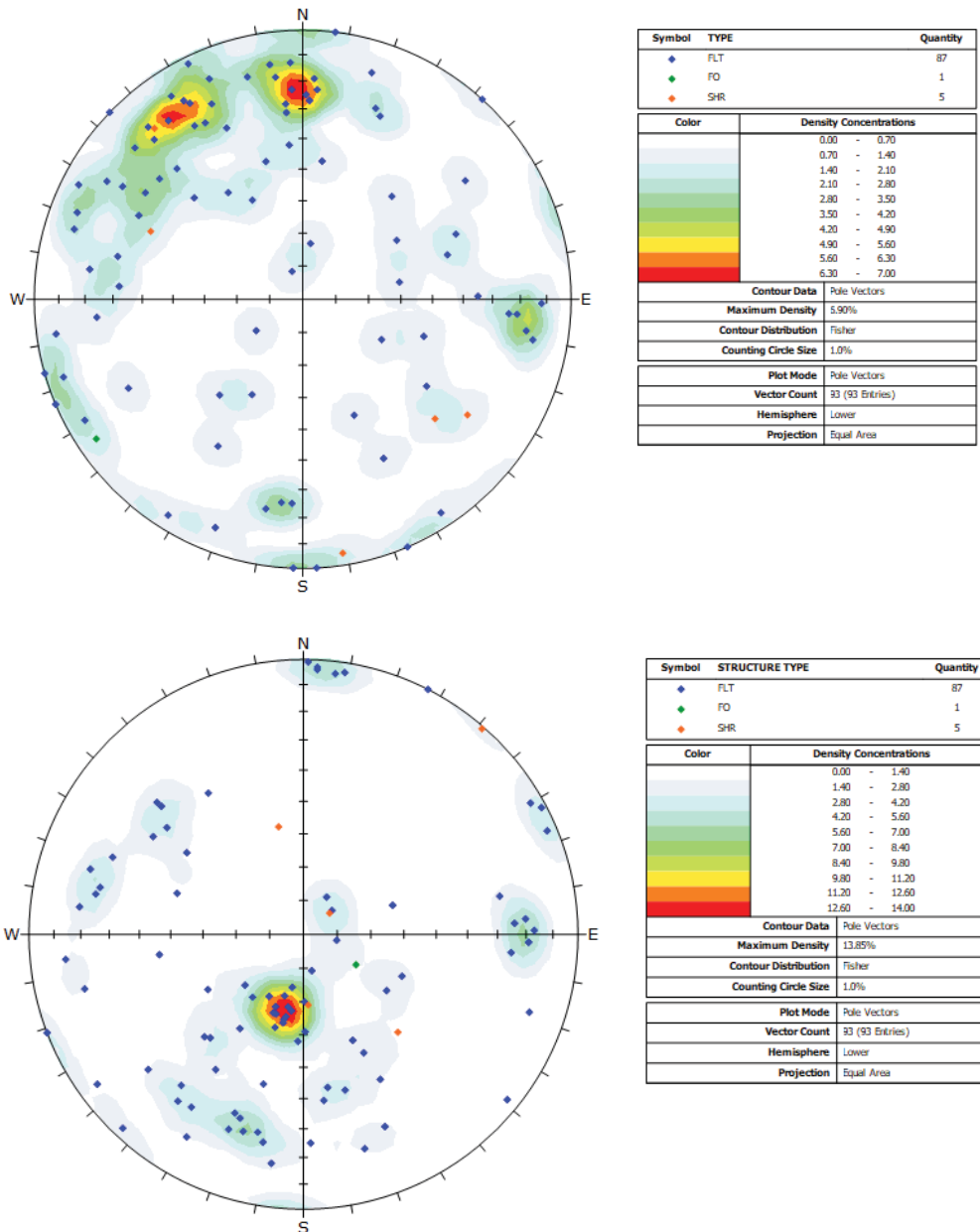


Figure 35: Stereonets showing orientation information for all Lineations. Top: All lineations (n = 93) plotted by associated plane type (Fault – FLT, Foliation – FO, Shear – SHR). Bottom: Poles to all oriented planes with identified lineations (n = 93).

Overall, the lineation dataset provides good indication that dip-slip motion predominates on gently to moderately inclined north to north-northeast dipping planes and nearly-transcurrent motion predominates on steeply inclined planes. Structures identified as faults and shear zones during geological core logging generally exhibit a similar history of motion, most prominently in a northwest-southeast direction.

Broken vs Intact or Partially Intact Structures

During the geological core logging, naturally occurring fractures were categorized as being broken (BR) when the core was physically broken into separate pieces at the location of the logged structure. Otherwise, they were categorized as intact (IN) or partially intact (PIN) where complete or partial cohesion was maintained along the planer logged structure. This categorization is based on a visual assessment of core condition when the core is removed from the barrel and initially examined. As mentioned earlier in the discussion of joints, which includes the majority of broken fractures, most of the adjacent broken fracture planes could be physically fit back together with no visible geological aperture. Therefore, the broken characteristic alone does not imply any direct relationship to the potential for a fracture to be hydraulically conductive. This categorization also does not include any judgement on whether or not the drilling activity itself may have induced the broken character. Of the 1876 oriented fractures, 226 (12 %) were logged as broken (Figure 36) and 1650 (88 %) were logged as intact or partially intact (Figure 37). Both the broken and intact or partially intact data emphasize pole clusters of fractures that dip gently north to north-northeast. The intact or partially intact data also emphasize subvertical to steeply inclined fractures that dip in multiple directions.

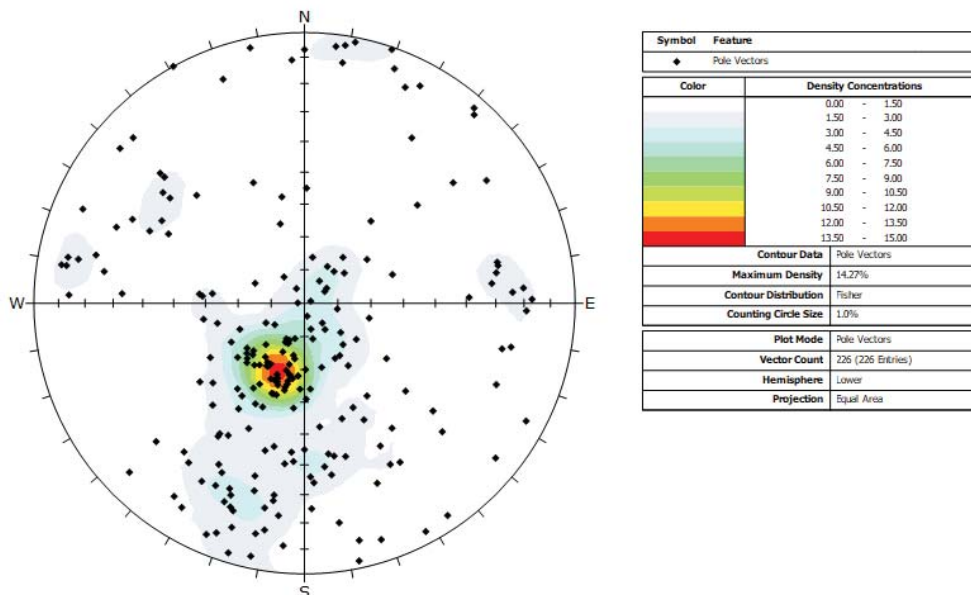


Figure 36: Stereonet plot showing poles to all fracture planes logged as broken (n = 226), with unweighted contours.

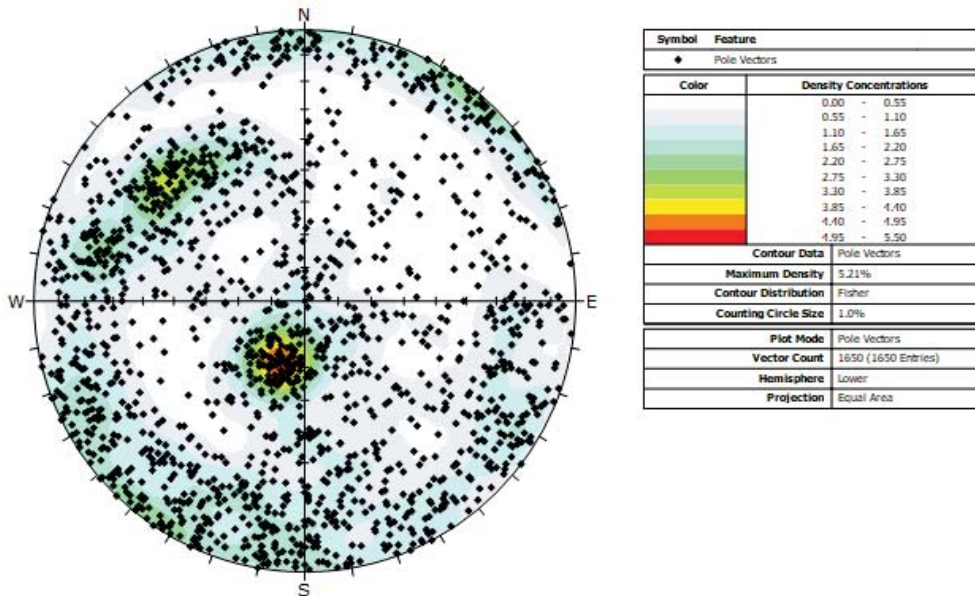


Figure 37: Stereonet plot showing poles to all fracture planes logged as intact or partially intact (n = 1650), with unweighted contours.

3.2.4.2 Interpreted Fracture Sets

Figure 38 presents the distribution of fracture poles and contoured stereographic distribution of poles to all logged fractures (joints, veins, faults, n = 1876) in order to assess for the presence of visible pole clusters that may define fracture sets in IG_BH03. These identified fracture sets can be compared with fracture sets identified in other boreholes, and also with surface mapped fracture and interpreted fracture (lineament) orientations, to provide guidance in developing three-dimensional fracture network models. Shear zones have not been included in this assessment.

Based on visual assessment of pole clusters and using the guiding contour density cut-off of 1 % from the Terzaghi-weighted dataset as a guide, nine cluster labelled (i) to (ix) were initially identified in IG_BH03. Expert judgement was also employed to refine boundaries between pole clusters. These clusters are outlined on the stereonet of unweighted poles to all fractures (upper stereonet plot in Figure 38), and include:

- a pole cluster near the centre of the stereonet that defines a subhorizontally-oriented to moderately inclined fracture set dipping north-northeast to north (cluster i - grey symbols in Figure 38, top stereonet);
- a pole cluster that defines a moderately to steeply inclined fracture set dipping southeast (cluster ii - red symbols in Figure 38, top stereonet);
- a pole cluster that defines a steeply inclined fracture set dipping west- to west-northwest (cluster iii - green symbols in Figure 38, top stereonet);
- a pole cluster that defines a steeply inclined fracture set dipping east-southeast (cluster iv - orange symbols in Figure 38, top stereonet);
- a pole cluster that defines a vertical to steeply inclined fracture set dipping southwest (cluster v - blue symbols in Figure 38, top stereonet);
- a pole cluster that defines a vertical to steeply inclined fracture set dipping northeast (cluster vi - purple symbols in Figure 38, top stereonet);
- a pole cluster that defines a vertical to steeply inclined fracture set dipping south (cluster vii - yellow symbols in Figure 38, top stereonet);

- a pole cluster that defines a vertical to steeply inclined fracture set dipping north (cluster viii - pink symbols in Figure 38, top stereonet); and
- a pole cluster that defines a vertical to steeply inclined fracture set dipping northwest (cluster ix – light blue symbols in Figure 38, top stereonet).

The remaining unclustered poles are not assigned to any particular fracture set and are therefore assigned to an additional random set.

The same nine pole clusters are also outlined on the unweighted and Terzaghi-weighted contour plots (middle and bottom images in Figure 38, respectively). The Terzaghi-weighted plot de-emphasizes the shallower-dipping pole clusters and emphasizes the remaining, more steeply inclined pole clusters (Figure 38). Notably, the Terzaghi-weighted contours, relative to the unweighted contours, extend closer to the perimeter of the stereonet than the unweighted contours, providing some indication that the steeply inclined and oppositely-dipping pole clusters, (v and vi) and (vii and viii), potentially represent members of the same near-vertical to vertically oriented fracture sets.

Given that IG_BH03 plunges south to south-southwest at an approximately 70° inclination, near vertical to vertical fractures, especially those that strike north-south or north-northeast-south-southeast, were poorly sampled during drilling. Therefore, there remains some uncertainty in the interpretation that the two steeply inclined and easterly-dipping pole clusters (ii and iv) are distinct fracture sets rather than components of the same fracture set. Similarly, it is uncertain whether the two steeply inclined and westerly-dipping pole clusters (iii and ix) are distinct fracture sets rather than components of the same fracture set. There also remains some uncertainty in the overall assignment of fracture sets because a large number of poles remains outside of any assigned fracture set region.

As a final interpretation for IG_BH03, pole cluster (i) is assigned to Fracture Set 1 defined by subhorizontally-oriented to moderately inclined, north-northeast to north-dipping fractures, pole cluster (ii) is assigned to Fracture Set 2, define by moderately to steeply inclined, southeast-dipping fractures, pole clusters (iii) and (iv) are assigned to Fracture Set 3, which includes steeply inclined, west- to west-northwest-dipping fractures (subset 3a) and steeply inclined, east-southeast-dipping fractures (subset 3b), pole clusters (v) and (vi) are assigned to Fracture Set 4, which includes steeply inclined, southwest-dipping fractures (subset 4a) and steeply inclined, northeast-dipping fractures (subset 4b), pole clusters (vii) and (viii) are assigned to Fracture Set 5, which includes steeply inclined, south- to south-southeast-dipping fractures (subset 5a) and steeply inclined, north-dipping fractures (subset 5b), and pole cluster (ix) is assigned to Fracture Set 6, which includes steeply inclined, northwest-dipping fractures. These final Fracture Set ID's are labelled on the unweighted and Terzaghi-weighted contour plots in Figure 38 and summarized in Table 9.

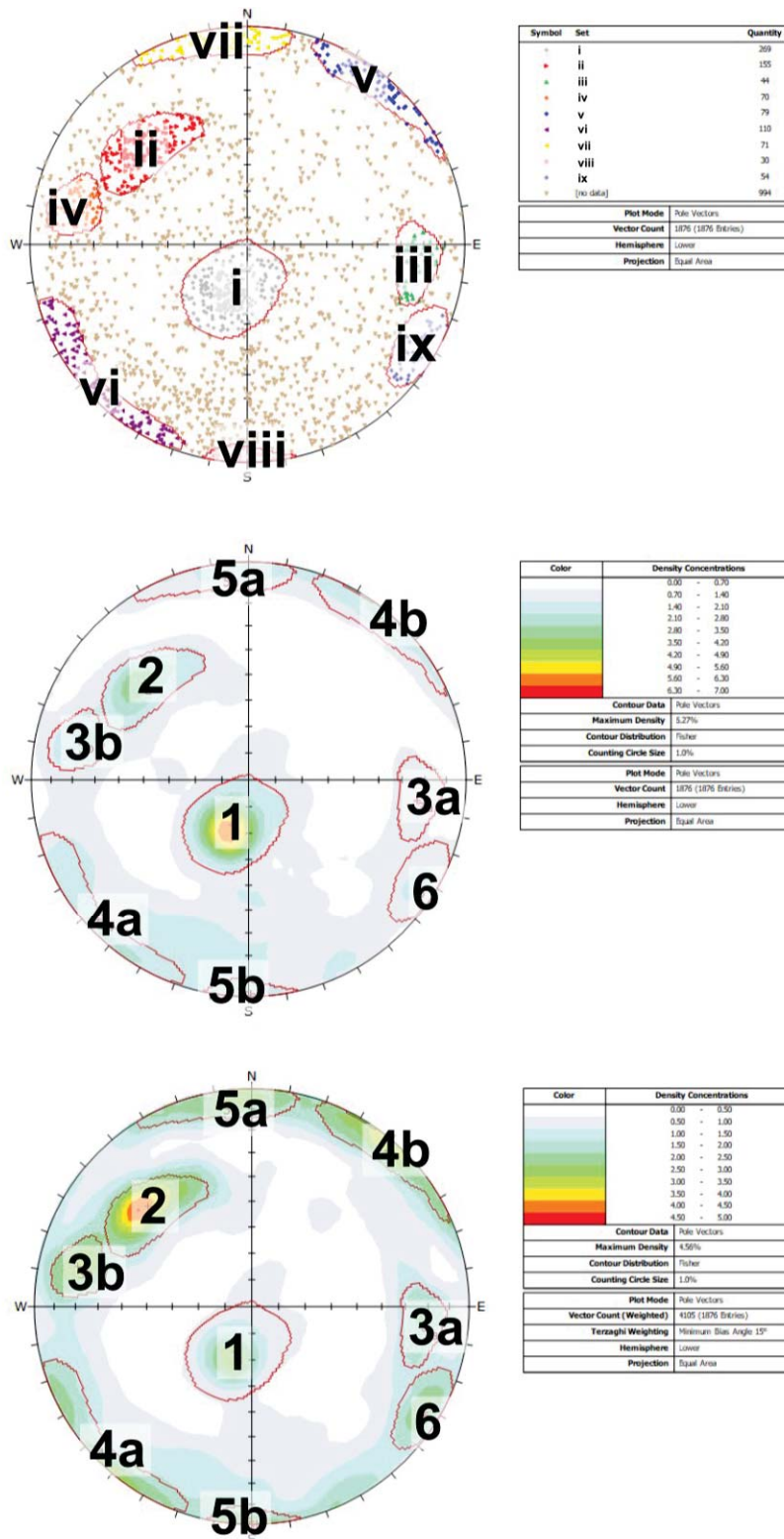


Figure 38: Stereonets of all oriented fractures, including all joints, veins and faults. Top: All fractures – poles, unweighted (n = 1876). Identified pole clusters are colour-coded by initial fracture set designation. Middle: All fractures – contours (n = 1876), unweighted. Bottom: All fractures – contours, Terzaghi-weighted (n = 4105). Middle and bottom stereonet are overlain by final fracture set interpretation. See text and Table 9 for additional summary.

Table 9: Summary of interpreted fracture sets in the borehole. Presents the general description of the orientation with a mean dip and dip direction.

Fracture Set ID	Orientation	Mean Dip / Dip Direction	Fracture Count
1	Subhorizontal to moderately inclined set, dipping north to north-northeast	18 / 020	269
2	Moderately to steeply Inclined, dipping southeast	55 / 133	155
3a	Steeply inclined set, dipping west to west-northwest	67 / 275	44
3b	Steeply inclined set, dipping east-southeast	70 / 101	70
4a	Steeply inclined set, dipping southwest	85 / 222	79
4b	Steeply inclined set, dipping northeast	85 / 047	110
5a	Steeply inclined set, dipping south to south-southeast	85 / 172	71
5b	Steeply inclined set, dipping north	86 / 000	30
6	Steeply inclined set, dipping northwest	81 / 301	54

Regarding the relationship between fracture sets and ductile structures, foliation exhibits a wide scatter with one minor pole cluster defining a moderately north-dipping orientation that overlaps with Fracture Set 1 (Figure 29). With Terzaghi weighting, a second foliation pole cluster overlaps Fracture Set 3b. The majority of shear zones are subhorizontal to inclined, dipping to the north-northeast (Fracture Set 1; Figure 30), while a small number are steeply inclined and dip northeast (Fracture Set 4b), dip south (Fracture Set 5a) and dip southeast (Fracture Set 6). The similarity of orientation between the brittle fracture sets and the ductile structures suggests that pre-existing ductile fabrics exerted some control on the development of brittle structures in the rock mass, in particular Fracture Set 1.

Regarding the relationship between fracture sets and brittle structures, the large number of joints relative to veins and faults is consistent with the presence of joints in all identified fracture sets (Figure 32). Though it can be pointed out that only weak pole clusters in the joint data coincide with Fracture Sets 2 and 3a. Poles to veins cluster prominently in the Fracture Set 1 and Fracture Set 2 orientations, and lesser so in the Fracture Set 3a/3b and Fracture Set 4a/4b orientations (Figure 33). Poles to faults cluster prominently in the Fracture Set 1 and Fracture Set 3a/3b orientations, and lesser so in the Fracture Set 2, 4 and 5 orientations (Figure 34).

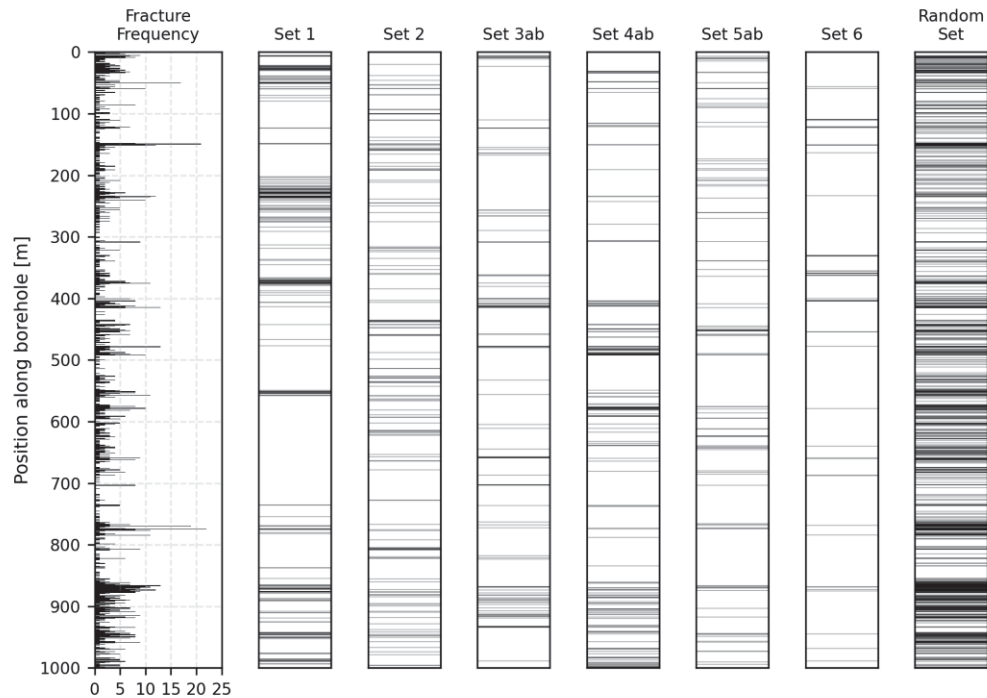


Figure 39: Summary log showing the frequency per metre of all brittle structures (left) in comparison to stick plots that show the distribution of all fractures assigned to defined fracture sets 1, 2, 3a/3b, 4a/4b, 5a/5b and 6, as well as unassigned random fractures.

Stick plots of the distribution of each fracture assigned to a fracture set, as well as unassigned random fractures, are plotted adjacent to the per metre fracture frequency of IG_BH03 in Figure 39. This presentation aids in assessing the degree of clustering evident by fracture set. Fracture set 1 is present in distinct locations along the entire length of the borehole. The tightest cluster of fracture set occurs at approximately 250 m. Occurrences of Fracture Set 1 are generally spatially coincident with peaks in the fracture frequency curve. There is also a notable absence of Fracture Set 1 between approximately 550 and 750 m. Fracture Set 2 is identified along the entire length of the borehole with little variation in density with position along borehole. Combined Fracture Sets 3a and 3b occur most prominently at the top of the borehole, around 400 m, and between 850 and 950 m. Elsewhere, they are sparse to absent. Combined Fracture Sets 4a and 4b exhibit clusters between 400 and 600 m, and below 850 m. Elsewhere, they are sparse to absent. Combined Fracture Sets 5a and 5b are distributed along the length of the borehole, with slightly increased density around 450 m. Fracture Set 6 is generally sparse to absent along the entire length of the borehole. The unassigned random fractures (994/1876; 53 %) are present along the entire length of the borehole with slight increases in frequency in the upper 50 m, at approximately 775 m and between 850 and 950 m.

It is understood that there is some uncertainty in the present assessment, primarily regarding whether Fracture Sets 3a and 3b should be treated as endmembers of the same sub-vertical fracture set. The strike of these two fracture sets is nearly parallel to the trend of the borehole and so they are the least sampled of all sets. In addition, it is acknowledged that the analysis presented above leaves a large portion (< 50 %) of fractures unassigned to any distinct fracture set. The fracture set interpretation will continue to be refined as additional boreholes are drilled in different directions.

3.2.4.3 Fracture Infill Minerals

Fracture infill, or secondary, minerals are observed in association with all fracture types in IG_BH03, including surface staining or hairline infilling in joints, mineral lineations on fault surfaces, and vein infilling. Of the 1876 oriented planar fractures, 1646 (88 %) were identified during geological core logging to host infilling minerals. The most prominent infill mineral phase identified in IG_BH03 is quartz, which occurs both as the sole mineral phase and in association with occurrences of chlorite, iron oxide stain, calcite, and epidote. The discussion below focuses on the orientation and distribution of these mineral phases. Stick plots of the distribution of each of these infill mineral types are plotted adjacent to the per metre fracture frequency of IG_BH03 in Figure 40.

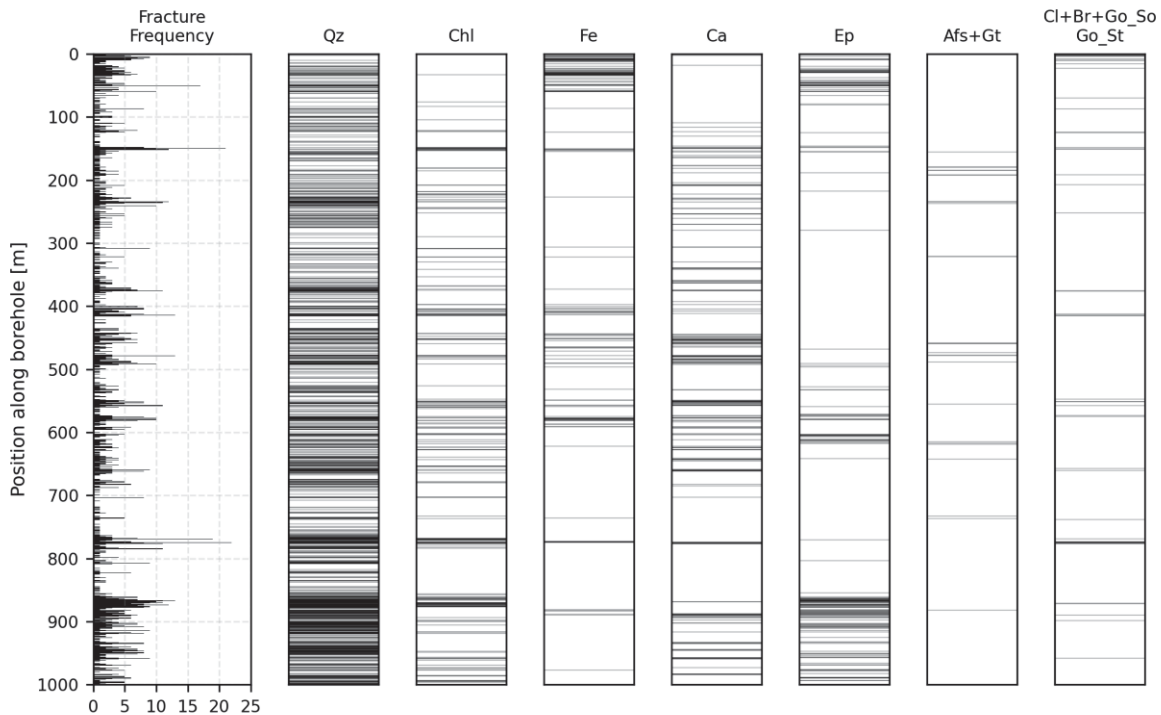


Figure 40: Summary log showing the frequency per metre of all brittle structures (left) in comparison to stick plots that show the distribution of the most common infill mineral phases including quartz (Qz), chlorite (Chl), iron oxide stain (Fe), epidote (Ep), calcite (Ca), a granitic (Gt) assemblage that includes some combination of alkali-feldspar (Afs) with quartz, plagioclase and biotite, and, fractures that exhibit either clay (Cl), broken rock (Br), soft clay gouge (Go_So) or stiff clay gouge (Go_St).

Quartz +/- chlorite, calcite, epidote, biotite, phlogopite, muscovite, iron oxide stain and/or pyrite was logged in 1181 of the 1876 (63 %) oriented fractures. Two prominent pole clusters, as shown in Figure 41, indicate that quartz-filled fractures predominantly dip gently north to north-northeast (fracture set 1) or dip moderately towards the southeast (fracture set 2). Less prominent, broad, pole clusters also define subvertical to steeply inclined quartz-filled fractures that dip north to northeast (fracture sets 4a/b and 5a/b). Fractures with quartz +/- accessory mineral infill are distributed throughout the entire length of the borehole, with slight increases in occurrence at about 750 m and between 850 and 950 m (Figure 40).

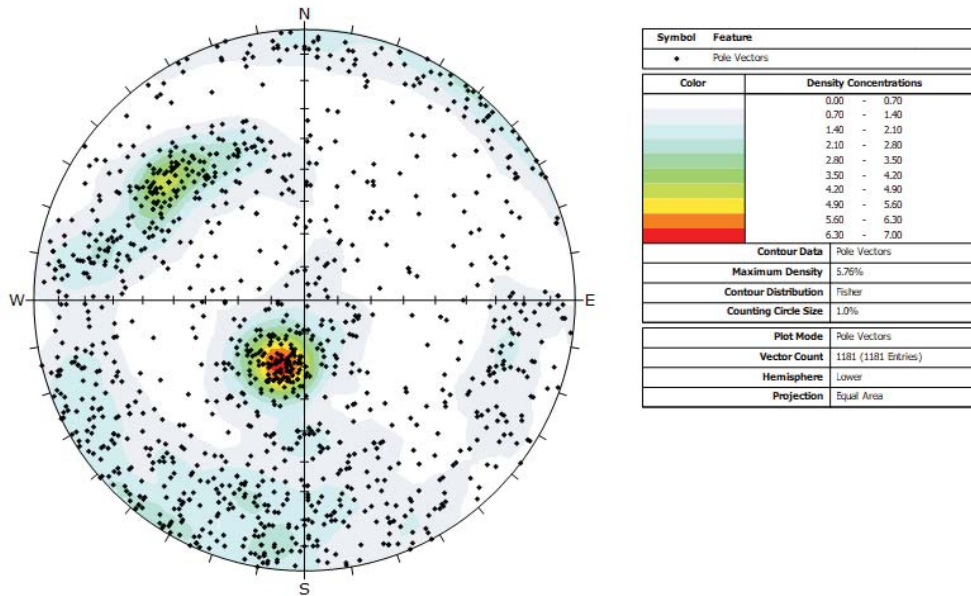


Figure 41: Stereonet plot showing poles to all fracture planes logged with quartz (n = 1181) +/- chlorite, calcite, epidote, biotite, phlogopite, muscovite, iron oxide stain and/or pyrite.

Chlorite is identified as an infill mineral phase in 253 of the 1876 (13 %) oriented fractures. Two prominent pole clusters define gently north to north-northeast dipping (fracture set 1), and moderately northwards dipping, chlorite-filled fractures (Figure 42). Weak pole clusters also define subvertical to steeply inclined chlorite filled fractures that dip in multiple directions, consistent with fracture sets 2, 3a/b, 4a/b, and 5a/b. Chlorite-filled fractures are relatively consistently distributed along the length of the borehole (Figure 40).

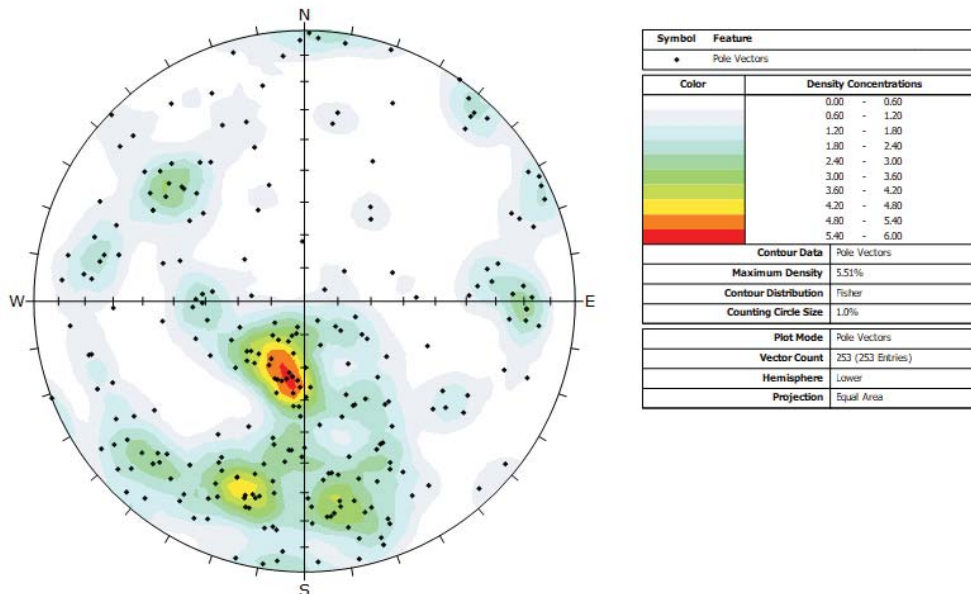


Figure 42: Stereonet plot showing poles to all fracture planes logged with chlorite (n = 253).

Calcite is identified as a mineral infill phase on 233 of the 1876 (12 %) oriented fractures. One prominent pole cluster defines subvertical and northwest striking (fracture set 4), calcite-filled fractures, (Figure 43). Less prominent pole clusters define calcite-filled fractures that are subvertical and east-west striking (fracture set 5). Fracture sets 1, 3a, 3b and 6 are represented by very weak pole clusters of calcite-filled fractures. Calcite-filled fractures are generally distributed along the entire length of the borehole with notable exceptions with few to no occurrences shallower than 100 m, and between 700 and 800 m, along borehole (Figure 40).

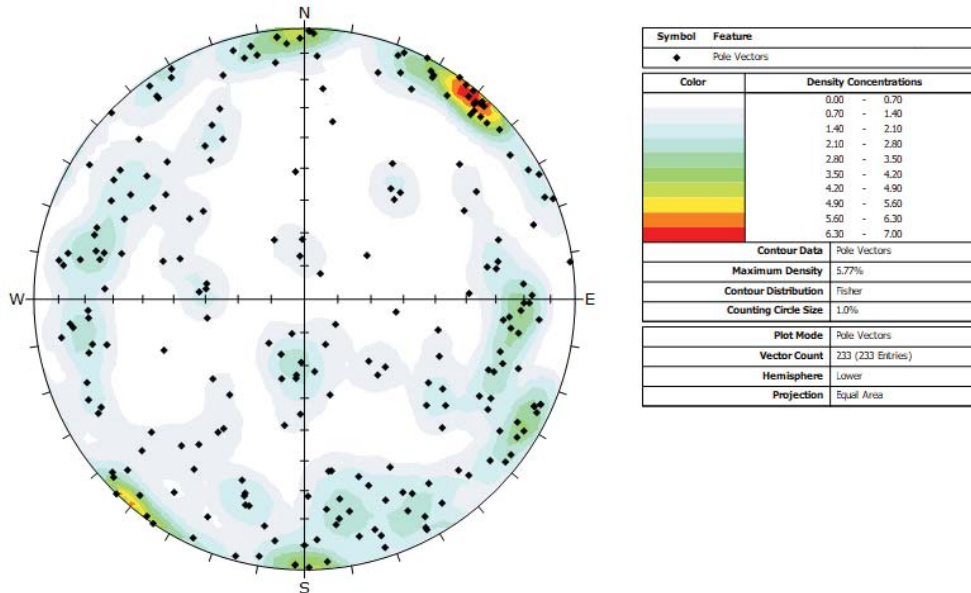


Figure 43: Stereonet plot showing poles to all fracture planes logged with calcite (n = 233).

Epidote is identified as a mineral infill phase on 209 of the 1876 (11 %) oriented fractures. One prominent pole cluster defines gently inclined fractures that dip towards the north-northeast (fracture set 1; Figure 44). Fracture sets 2 and 4 are represented by very weak pole clusters of epidote-filled fractures. Epidote is distributed in three main intervals along the borehole, including, less than 50 m, between 450 and 600 m, and below 850 m (Figure 40).

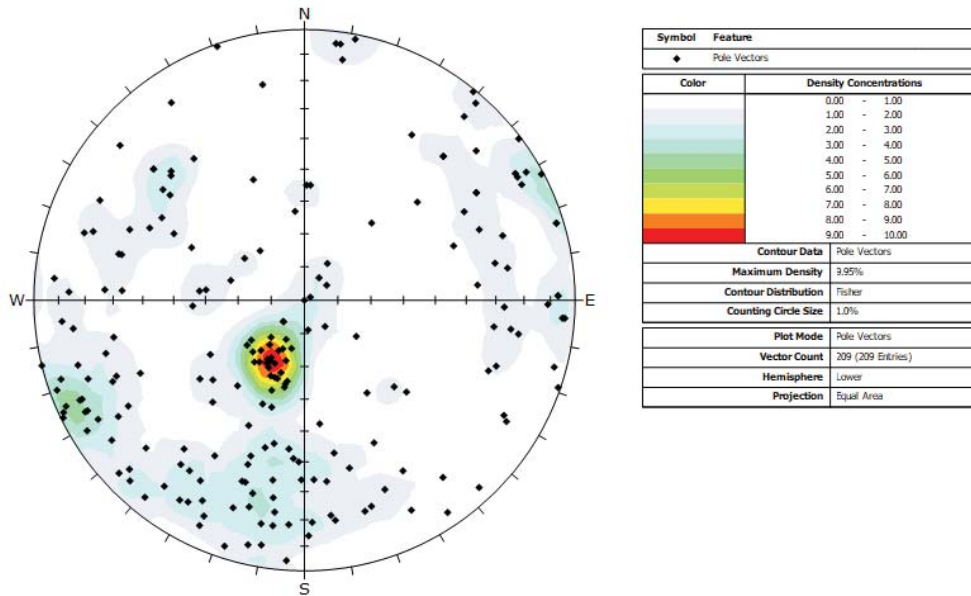


Figure 44: Stereonet plot showing poles to all fracture planes logged with epidote (n = 209).

An iron oxide mineral, potentially hematite, is present primarily as a stain on the surfaces of 156 of the 1876 (8 %) oriented fractures. Two main pole clusters define subvertical fractures that strike east-southeast or south-southeast (fracture set 4; Figure 45). Fracture sets 1, 2, 3a, 3b and 5 are represented by very weak pole clusters of iron oxide-stained fractures. Iron oxide-stained fractures are predominantly logged in the upper 50 m of the borehole and between 400 and 600 m along borehole (Figure 40).

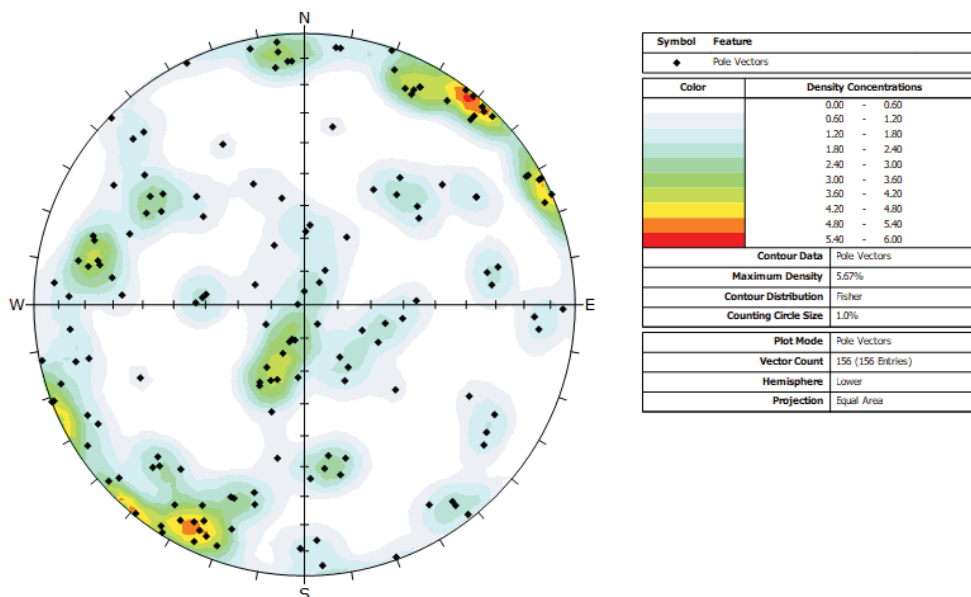


Figure 45: Stereonet plot showing poles to all fracture planes logged with iron oxide stain (n = 156).

Fractures infilled with clay, soft or stiff clay gouge or broken rock were logged in 47 of the 1876 (3 %) oriented fractures. One prominent pole cluster defines moderately inclined fracture planes that dip towards the northwest, which is slightly oblique to, but overlapping, the orientation of fracture set 1 (Figure 46). Fracture sets 2, 3a and 5 are represented by very weak pole clusters of clay, gouge or broken rock-filled fractures.

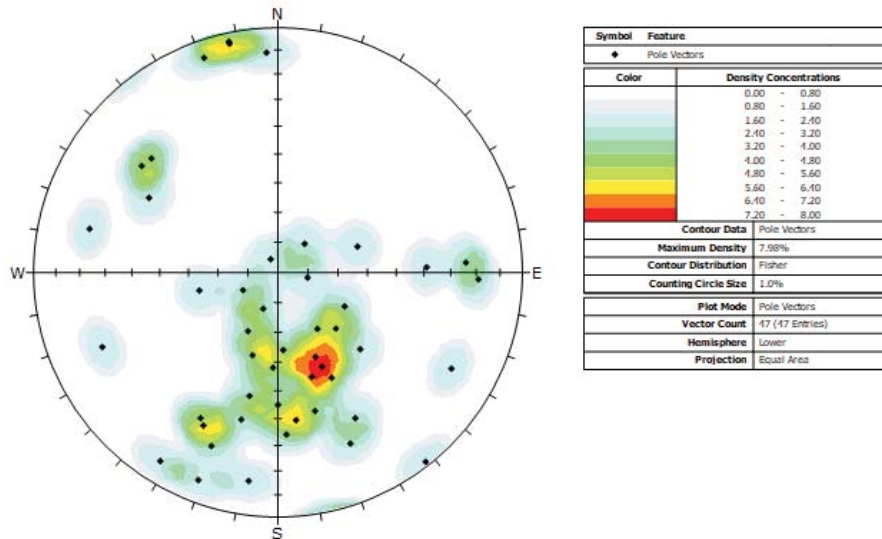


Figure 46: Stereonet plot showing poles to all fracture planes logged with clay, broken rock, or hard or soft gouge (n = 47).

A granitic infill assemblage characterized by alkali-feldspar +/- quartz, plagioclase and biotite, and lesser muscovite +/- phlogopite is identified in 43 of the 1876 (2 %) oriented fractures. The distribution of the poles to these fractures shows a high degree of scatter (Figure 47). However, one slightly more prominent cluster that defines moderately inclined fractures that dip towards the southeast, coincident with fracture set 2. Fracture sets 1, 4 and 5 are represented by very weak pole clusters of fractures with granitic infill.

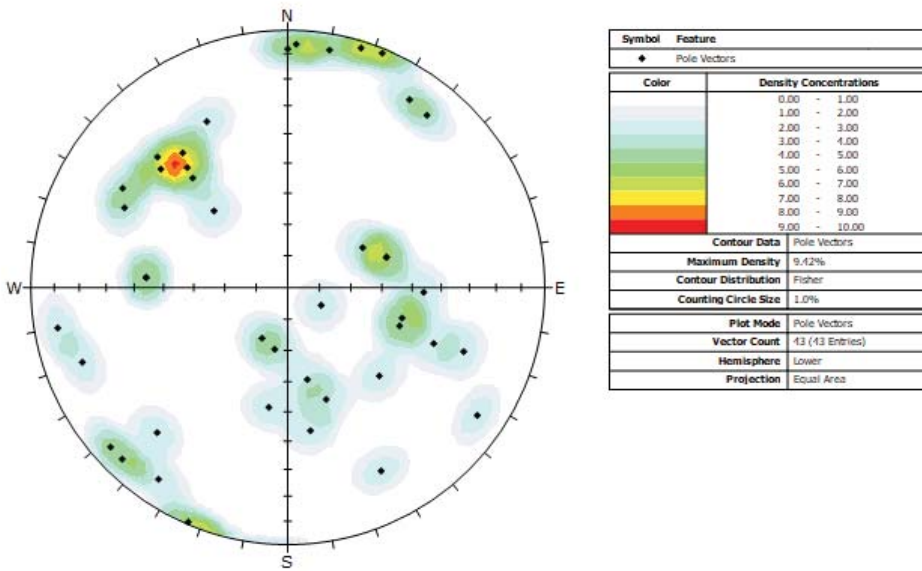


Figure 47: Stereonet plot showing poles to all fracture planes logged with granitic infill (n = 43), including alkali-feldspar +/- quartz, plagioclase and biotite.

A total of 230 fractures (12 %) have no associated infill mineral phase assigned to them. This includes 150 fractures that were only identified in the televiewer datasets and could not confidently be assessed for infill mineral type, even if present (Figure 48). The poles to fractures with no assigned infill minerals exhibit one prominent cluster highlighting the dominance of subvertical and southwest-striking fractures (fracture set 6). Fracture sets 1, 3a and 3b are and 5 are represented by very weak pole clusters of unfilled fractures.

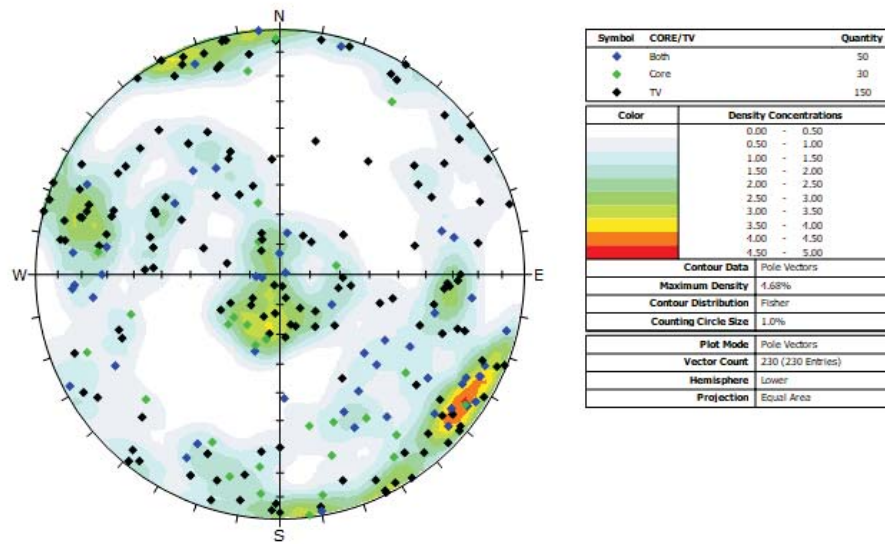


Figure 48: Stereonet showing poles to all fractures logged as having no identifiable mineral infill phase (n = 230). Fractures logged in ‘televiewer’ datasets only, geological ‘core’ logging only, or identified in ‘both’ datasets, are distinguished.

3.2.5 Structural Unit Classification

Structural units (SU) have been defined to capture the general variation in fracture frequency along the length of the borehole, primarily on the basis of broad changes in slope visible in the cumulative fracture frequency curve. This curve was derived using the fracture dataset (i.e., joints, veins, and faults, including broken and intact/partially intact structures) and is presented in Figure 49. The mean fracture frequency per metre, derived using the same dataset, is reported as an additional indicator of these same general trends. A total of three SUs are defined for IG_BH03 (Table 10). Stereonets of fracture orientation data for each defined SU are included in Appendix E:.

Structure Unit 1 (SU1) extends from the ground surface (0 m) to a position along borehole of 51.0 m (Figure 49). This unit exhibits a relatively shallow slope in the cumulative fracture frequency curve corresponding to a relatively higher degree of fracturing of the bedrock than the adjacent, deeper, SU2. The SU has 171 mapped fractures with an average fractures per metre of 3.42, however, fracture frequency is not consistent throughout the unit, and ranges from metre long intervals completely devoid of fractures and intervals up to 17 fractures per metre. The degree of fracturing and the range of positions observed here tends to be consistent with the shallow SU in IG_BH01 (Parmenter et al., 2022). Fractures in this unit cluster in two dominant sets: trending north-northeast and steeply dipping toward the east and trending northwest and dipping shallowly toward the northeast. There are less prominent clusters of near-vertical structures trending northwest-southeast and southwest-northeast. There are 146 oriented fractures in SU1, including 134 joints, 9 veins, and 3 faults (Appendix E:). Poles to these fractures overlap with Fracture Sets 1, 3a and 3b, and to a lesser extent Fracture Sets 5a and 5b.

Structure Unit 2 (SU2) has a thickness of 809.5m ranging from 51.0 m to a position along borehole of 860.50 m. This SU is defined by a relatively steep slope in the cumulative fracture frequency curve corresponding to a lower degree of fracturing of the bedrock compared to the adjacent SU’s above and below (Figure 49). This longer interval has a total of 1307 fractures mapped with an average fracture frequency of 1.61 fractures per metre. This SU exhibits some local variability in counts from zones of unfractured bedrock to discrete intervals with up to 22 fractures per metre.

Despite the localized high fracture counts, this interval is still considered to have an overall low fracture frequency, with narrow discrete fracture zones (see Section 3.2.6 for more discussion on defined fracture zones). Fractures in SU2 display the most variation in orientation due to the relatively large thickness compared to SU1 and SU3. Fractures parallel the dominant sets discussed in Section 3.2.4.2. There are 1255 oriented fractures in SU2, including 921 joints, 276 veins, and 58 faults (Appendix E:). Poles to these fractures overlap with all identified Fracture Sets.

Structure Unit 3 (SU3) extends from 809.5m to the bottom of the borehole at 1000.54 m (Figure 49) and shows a relatively shallow slope (compared to SU2) in the cumulative fracture frequency curve corresponding to a relatively higher degree of fracturing of the bedrock. The slope of the curve corresponds to a total of 495 fractures in the interval with an average fracture frequency of 3.51 fractures per metre with local variability within the unit ranging between 0 and 13 fractures per metre. Fractures in SU3 cluster in three main orientations: near-vertical and striking northwest-southeast, gently inclined and dipping northeast, and steeply inclined and dipping west-northwest. There are 478 oriented fractures in SU3, including 333 joints, 113 veins, and 29 faults (Appendix E:). Poles to these fractures overlap with all identified Fracture Sets, though Fracture Sets 4b, 5b, and 6 are only weakly present.

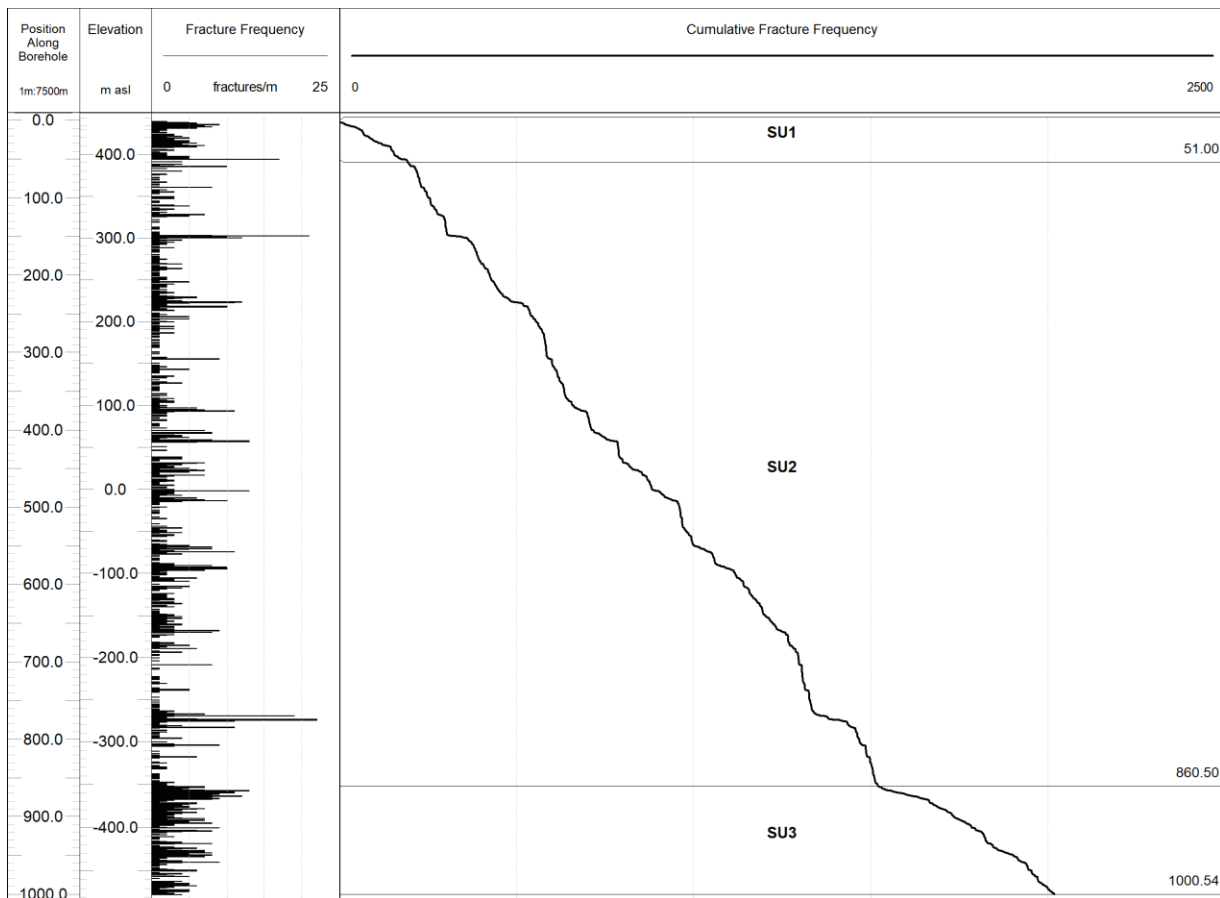


Figure 49: Fracture frequency histogram (left) and cumulative fracture frequency curve (right) showing vertical distribution of all logged joints, faults, and veins along the borehole. The cumulative fracture frequency curve shows the changes in slope where boundaries in structural units (SU) are defined. Structural units and their top and bottom positions along borehole are labelled on the figure.

As with the rock units defined previously, the criteria for defining the integrated structural units for IG_BH03 and other boreholes may be modified once additional fracture data is collected. The framework presented here represents an interpretation based on broad trends in the available data.

Table 10: Ranges of position along borehole and standard statistics for fracture frequencies captured within the defined structural units (SU) within the borehole.

	<i>SU1</i>	<i>SU2</i>	<i>SU3</i>
<i>Position Range (m)</i>	0 – 51	51 – 860.50	860.50– 1000.54
<i>Thickness (m)</i>	51	809.5	140.04
<i>Min (/m)</i>	0.00	0.00	0.00
<i>Max (/m)</i>	17	22	13
<i>Average (/m)</i>	3.42	1.61	3.51
<i>Standard Deviation (/m)</i>	3.01	2.48	2.97

3.2.6 High Fracture Frequency Intervals (HFFI)

Along with the broad changes in fracture frequency that are used to define the SU's described above, additional more discrete intervals of increased fracture frequency were also identified in IG_BH02. These occurrences are referred to as high fracture frequency intervals (HFFI) and are defined as a cluster of fractures (i.e., faults, joints and or veins) that exceeds a minimum relative fracture intensity threshold along a distinct borehole length (see below for details of IG_BH03). The spatial distribution of fractures and their intensity over the length of the borehole provide meaningful justification for defining HFFIs within the subsurface. Within the boreholes, the HFFIs are primarily dominated by fractures that share similar orientations within a single fracture set (i.e., fracture corridor) or by fractures in a range of orientations (i.e., fracture swarm), and locally may also comprise few minor ductile shear zones. Fracture summaries presented in the previous sections provide details on fracture sets, fracture types, and fracture mineral infilling which may contribute to the characterization of the HFFI. At the end of this section, an attempt is made to broadly correlate the identified HFFIs with lineaments trends that were interpreted based on remote sensing data on the ground surface in proximity to IG_BH03.

HFFIs were defined using a semi-automated approach applied to the borehole fracture frequency per metre log. To visualize contiguous zones of increased fracture intensity, the fracture frequency distribution was smoothed with a uniformly weighted moving average filter using the “uniform_filter1d” function from the SciPy processing package in Python (Virtanen et al. 2020). This filter is equivalent to a moving mean and is commonly applied to time-series data to smooth high-frequency data and enable detection of broader responses. This filter preserves the low-frequency components of the input data while high-frequency components are attenuated. The magnitude of the filter is defined by the uniform window size (w), which controls the degree of smoothing applied. In this study, a step size and window size of 1 m and 15 m, respectively, was defined.

The HFFIs are defined using the smoothed fracture frequency curve using two peak detection algorithms, “find_peaks” and “peak_widths” from the SciPy processing package (Virtanen et al. 2020). The peak detection algorithm finds all local maxima by simple comparison of neighboring values. A peak is defined as a local maximum where any sample whose two direct neighbours have a smaller amplitude. The difference in magnitude with the neighbouring values is defined by a threshold value in the algorithm, such as the peak prominence. The prominence of a peak measures the magnitude of the peak relative to the neighbouring values and is defined as the vertical distance between the peak and its lowest neighbouring value. Using the smoothed fracture frequency curve as input data, the peak prominence threshold was set at four for this study.

Once peaks are defined, the peak widths are defined based on the anomaly width at a specified distance between the peak maxima and the lowest neighbouring value (i.e., along the prominence height). In this study, a relative height of 0.5 is used at a threshold to extract the width of the peak.

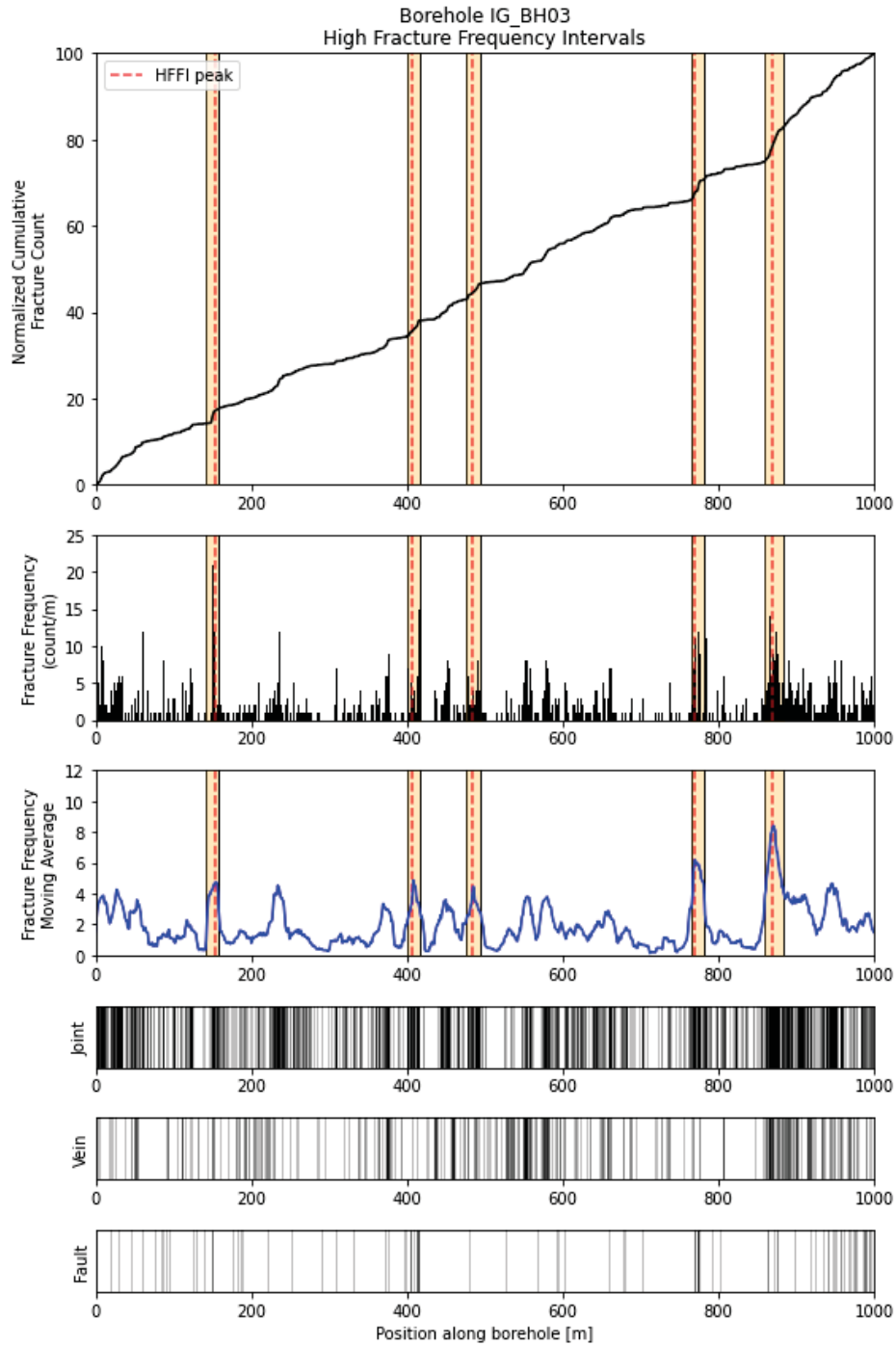


Figure 50. High fracture frequency intervals (HFFI) interpretation based on fracture intensity from borehole fracture frequency log. Five high fracture frequency intervals are outlined by their yellow bands. The red dashed line represents the peak location.

Figure 50 presents the HFFI results from the fracture frequency data in IG_BH03. Based on the smoothed fracture frequency data and the peak detection analysis, from and to position along borehole (in metres) and overall width (in metres along borehole axis) of five HFFIs have been defined. Figure 50 shows the cumulative counts of fractures along the length of the borehole and displays the fracture frequency per metre and the filtered fracture frequency. The cumulative curve, along with these data plots show evidence of discrete intervals of increased fracture intensity. Stick plots of joints, veins and faults display the location of each individual fracture type along the borehole length. A summary of the HFFIs for IG_BH03 are presented in Table 11, including dominant fracture orientation(s), rock type(s) present, fracture set association, alteration, and fracture infill characteristics.

Although the results presented in Figure 50 are visually verified to be ideal candidates for HFFI interpretation, changing the peak detection algorithm input parameters can result in other possible HFFI outcomes. For example, reducing the peak prominence threshold or the applied window size in the smoothing function results in an increase in the number of peaks identified from the data. Conversely, increase these parameters reduces the number of peaks identified. Similarly, adjusting the peak height parameter used in the peak width algorithm works to either increase or decrease the width of the identified interval, however the peak location remains the same. Despite these possible uncertainties, our approach attempted to optimize the peak picking parameters through trial and error in order to visually match the identified peaks to the obvious increases in fracture frequency observed in the data. The application of this approach can then be applied to other boreholes, therefore reducing interpreter bias and subjectivity in the identification of HFFI in the boreholes.

Table 11. High fracture frequency intervals (HFFI)

High fracture frequency intervals (HFFI)	Top Position (m)	Bottom Position (m)	Width (m)	Dominant Fracture Set Orientations* (major; minor (STR TYPE))	Rock Type, Alteration, Infill
IG_BH03_HFFI_1	142.30	157.70	15.40	145/52 (JN, VN); 292/19 (JN, VN, FLT)	Biotite granodiorite-tonalite with one amphibolite lens. Chloritization, bleaching, silicification, potassic alteration. Calcite, quartz, chlorite, and muscovite infill associated with 145/52 orientation (fracture set 2), quartz, muscovite, chlorite, calcite, and gouge associated with 229/19 orientation (fracture set 1). Large variety of infill types.
IG_BH03_HFFI_2	400.83	416.50	15.67	244/90 (JN, FLT); 270/70 (FLT, JN)	Biotite granodiorite-tonalite. Silicification and potassic alteration. Chlorite and quartz infill associated with 244/90 (fracture set 4), chlorite, clay gouge, and quartz infill associated with 270/70 (fracture set 3a). Quartz and chlorite are most common infill types.
IG_BH03_HFFI_3	476.75	494.58	17.83	222/85 (JN)	Biotite granodiorite-tonalite, one aplite dyke and one aphanitic tonalite dyke. Potassic alteration. Joints associated with 222/85 (fracture set 4). Quartz and calcite infill with minor chlorite, iron-oxide, and muscovite. Quartz and calcite are most common infill types.
IG_BH03_HFFI_4	764.33	781.60	17.27	354/50 (JN, FLT); 180/86 (JN)	Biotite granodiorite-tonalite, one feldspar-phyrlic tonalite dyke, and four amphibolite lenses. Sericite, potassic alteration, argillization, and silicification. Quartz, chlorite, muscovite, and minor clay gouge associated with 354/50 orientation (steeper-dipping set 1 fractures). Plagioclase, iron-oxide, muscovite, and quartz infill associated with 180/86 orientation (fracture set 5). Quartz and muscovite are most common infill types.
IG_BH03_HFFI_5	860.00	882.50	22.50	164/82 (JN); 356/70 (JN, VN, FLT); 280/63 (JN, VN)	Biotite granodiorite-tonalite, two feldspar-phyrlic dykes and one amphibolite lens. Silicification, bleaching, chloritization, and potassic alteration. No infill minerals associated with 164/82 orientation (fracture set 5). Quartz, epidote, and chlorite associated with 356/70 orientation. Quartz and muscovite associated with 280/63 orientation (fracture set 3a). Epidote, chlorite, and quartz most common infill types in this interval.

*DipDirection/Dip convention

For each HFFI, fracture (including joints, veins, and faults) orientations can be plotted on stereonet to further evaluate the orientation distributions and define one or more orientations that are characteristic of the interval (e.g., HFFI_1 in Figure 51, see Appendix F: for stereonet of all defined HFFIs). Figure 51 presents a Terzaghi-weighted stereonet for HFFI_1 containing 66 fractures (faults, veins, and dykes) in the interval. Dominant orientations in Table 11 are interpreted manually as the peaks defined by the Terzaghi-weighted pole density maxima. The resulting fracture orientations from within the HFFIs can provide input into modelling such zones as surfaces in deterministic fracture network models.

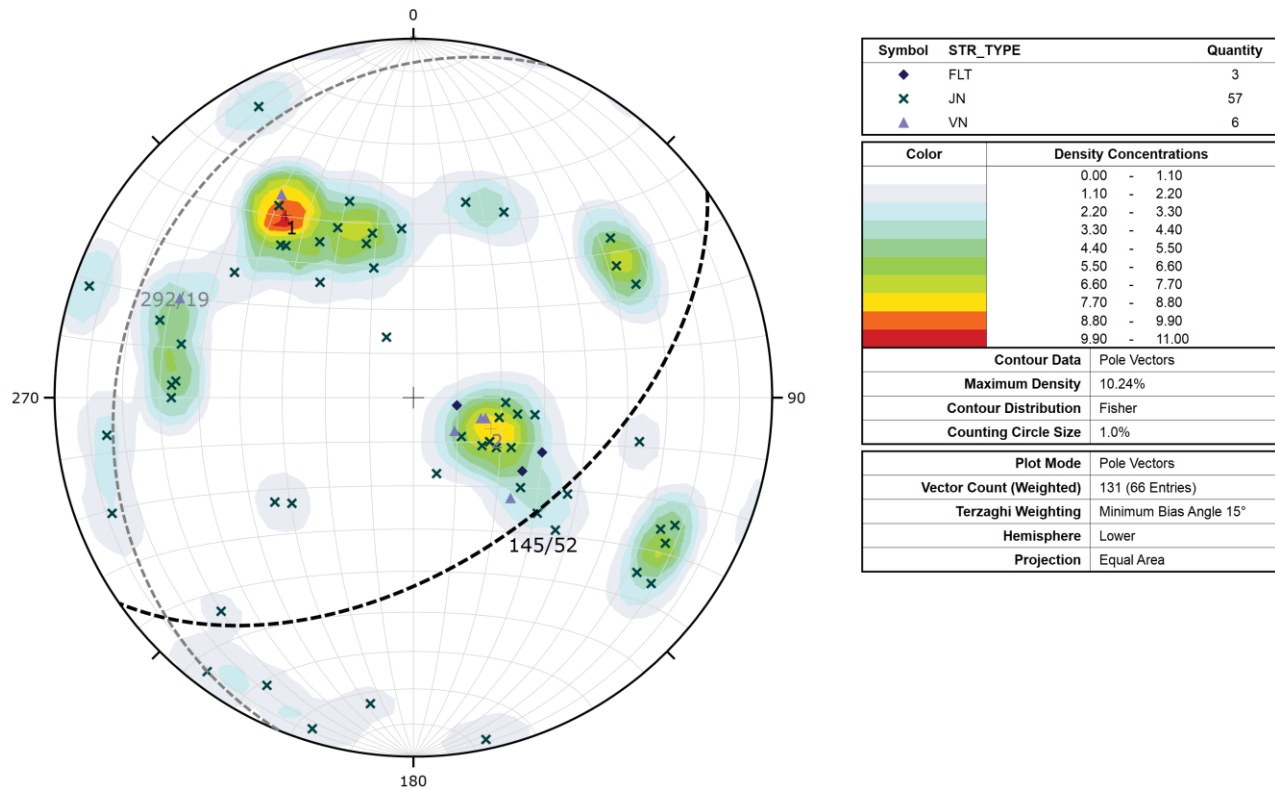


Figure 51. Terzaghi-weighted stereonet plot of fractures (JN, VN, FLT) within high fracture frequency interval 1 (HFFI_1) from 142.3 – 157.7 m. Two peaks are defined, a major peak with a mean orientation of 145/52 (best fit plane shown as black dashed great circle) and a minor peak with a mean orientation of 292/19 (best fit plane shown as grey dashed great circle; DipDirection/Dip convention).

HFFI_1 (142.3 – 157.7 m)

HFFI_1 is predominantly biotite granodiorite-tonalite with a 1.19 m amphibolite unit from 148.65 – 149.84 m. Figure 52 shows an interval of this HFFI from 143.69 – 155.0 m. The amphibolite unit and the contacts between the amphibolite and the host rock exhibit slight to moderate chlorite alteration and the contact orientations cluster with the minor peak that dips 19° toward 292°. At the lower contact between the amphibolite and the biotite granodiorite-tonalite, moderate silicification and minor potassic alteration are logged. The fractures in this interval are concentrated around and within the amphibolite unit; both contacts are intact, and they are in a similar orientation to the minor fracture peak (292/19). Three shear zones are logged in this interval, two ductile shear zones in the amphibolite are aligned with the contacts are oriented with the minor fracture peak (292/19). A variety of infill types are logged in this interval, including one occurrence of stiff gouge in a fault that is oriented with the minor fracture peak (292/19), suggesting this fault is a geologically younger feature or was reactivated. Most of the fractures are at a high angle to the core, indicating a relatively shallow dip. The intersection of these shallow-dipping fractures and steeper, high-angle fractures create intervals of broken core in the amphibolite and just below the bottom contact (Figure 52). The biotite granodiorite-tonalite above and below the amphibolite is characterized by well spaced, mostly shallow-dipping fractures (Figure 52).



Figure 52. Core from an interval of HFFI_1 (143.69 – 155.0 m). Biotite granodiorite-tonalite above and below the amphibolite unit is characterized by well spaced, fairly shallow-dipping fractures. Fracture intensity increases around and within the amphibolite, including a fault logged with stiff gouge infill at 148.75 m. Intersections of shallow and steeply dipping fractures create intervals of broken core.

HFFI_2 (400.83 – 416.5 m)

HFFI_2 is entirely biotite granodiorite-tonalite with minor potassic alteration and silicification for the first 8 m. There are intervals of pervasive, moderate to strong silicification associated with fractures starting at 406.75 m and continuing to the end of the zone (Figure 53). The fractures throughout this HFFI are well spaced but dominantly sub-vertical, in contrast to HFFI_1. There are 11 faults logged in this interval, eight of which are oriented with the major (n=4) and minor (n=4) fracture peaks identified on the stereonet (244/90 and 270/70, respectively; Appendix F:). Two shear zones are logged in this interval; neither are associated with the interpreted fracture peak orientations. Chlorite and quartz are the most common infill types logged in this interval and the most common infill types associated with the identified fracture peaks. There is one occurrence of soft gouge logged at 414.51 m in a fault that is oriented with the minor fracture peak (270/70).



Figure 53. Core from an interval of HFFI_2 (401.59 – 413.14 m). Biotite granodiorite-tonalite with moderate to strong silicification associated with well-spaced, steeply dipping fractures.

HFFI_3 (476.75 – 494.58 m)

HFFI_3 is biotite granodiorite-tonalite with two dykes: one 0.36 m aplite dyke at 477.78 m and one 1.67 m aphanitic tonalite dyke at 489.91 m. The contacts of the aphanitic tonalite dyke cluster with the major peak dipping 85° toward 222° , while the aplite dyke does not have any association to the cluster defined in this PDZ. Moderate to highly pervasive potassic alteration is logged throughout this zone. Fractures are well-spaced and predominantly steeply-dipping; there does not appear to be an increase in fracture intensity around either of the intrusions (Figure 54). This interval is almost entirely defined by joints, with one fault and 10 veins that do not share an orientation with the main fracture peak ($222/85$). Calcite and quartz are the dominant infill types logged in this interval and the dominant infill types associated with the major fracture peak orientation.



Figure 54. Core from an interval of HFFI_3 (483.62 – 495.25 m). Biotite granodiorite-tonalite with moderately pervasive potassic alteration logged. An aphanitic tonalite dyke with steeply dipping contacts is visible at 489.91 m and is not associated with an increase in fracture frequency.

HFFI_4 (764.33 – 781.60 m)

HFFI_4 is part of RU2 and has several small amphibolite units. The zone starts in biotite granodiorite-tonalite and has one 1.07 m feldspar-phyric tonalite dyke at 765.8 m followed by a 2.86 m interval of biotite granodiorite-tonalite with four amphibolite units that are 0.43, 0.7, 0.13, and 0.63 m wide, respectively (Figure 55). The amphibolite contacts all cluster with the dominant fracture peak in this zone, dipping 50° toward 354°. The feldspar-phyric tonalite dyke contacts are steeper dipping (ca. 70°) to the northeast, outside of the defined peak. Moderate potassic alteration is logged in the host biotite granodiorite-tonalite and minor to moderate sericitization, argillization, and silicification are logged in the four amphibolite units. Alteration and fracture intensity increase around the contacts and through the amphibolites; fractures in the biotite granodiorite-tonalite and feldspar-phyric tonalite dyke are well spaced (Figure 55). There is a greater spread in the orientation of fractures in this interval compared to HFFI 1-3 (see stereonet in Appendix F:). Seven of 10 logged faults and all three logged shear zones are oriented with the identified fracture peak (354/50). Dominant logged infill types are quartz, muscovite, and calcite, all of which have a significant spread in orientations. Chlorite and quartz are the most common infill types associated with the identified fracture peak, along with four occurrences of soft gouge and one occurrence of clay infill. Three of the logged soft gouge infill and the clay infill are associated with faults and one soft gouge infill is associated with a joint; the presence of these infill types suggests geologically younger features or reactivation of older structures and all five are logged in amphibolite.



Figure 55. Core from an interval of HFFI_4 (765.86 – 777.08 m). There is a feldspar-phyric dyke at the top of the zone and then biotite granodiorite-tonalite, with increasing alteration and fracture intensity approaching the amphibolite units starting at 773.65 m.

HFFI_5 (860 – 882.5 m)

HFFI_5 is part of RU2 and has one 0.48 m feldspar-phyric tonalite dyke at 869.76 m, and a 0.35 m amphibolite unit at 870.92 m that is in contact with a 0.34 m feldspar-phyric tonalite dyke, followed by biotite granodiorite-tonalite until the bottom of the zone (Figure 56). Minor silicification is logged around fractures at the top of the zone, increasing to moderate to strong silicification approaching the top contact of the upper feldspar-phyric tonalite dyke and continuing through the dyke. Minor to moderate chloritization is logged in association with the dykes and amphibolite unit, and minor silicification, potassic alteration, and chloritization are logged in the lower biotite granodiorite-tonalite host rock.

There is a mechanical broken core zone at the top of this interval, from 861.57 – 862.46 m that was not included in the fracture frequency and identification of this HFFI. Fractures at the top of the zone are well spaced. There is an increase in fracture and alteration intensity, joints, and shear zones around 867 m that continues through the subordinate rock types to about 875 m where the zone transitions back into “regular” biotite granodiorite-tonalite with minor alteration and well-spaced joints (Figure 56). The orientation of fractures in this interval are widely spread on a stereonet (see Appendix F:). One major peak (164/82) and two minor peaks (356/70 and 280/63) were identified, but there are many structures not associated with these three dominant orientations, including three of five faults that are shallowly dipping towards the north northwest. The other two logged faults are associated with the fracture peak dipping 70° towards 356°.

HFFI_5 has 17 logged shear zones, significantly higher than any other HFFI in IG_BH03. Four of the shear zones are associated with the fracture peak dipping 70° towards 356°. The other 13 shear zones are not associated with any identified peak or other cluster; two are subvertical and trend northwest-southeast, one dips steeply towards the south southwest, and the other 10 dip steeply to shallowly toward the north, northeast, or northwest.

The dominant logged infill type in this interval is quartz, followed by epidote and chlorite. Quartz infill is logged in structures associated with the two minor fracture peaks, chlorite and epidote are also logged in structures associated with the cluster dipping steeply north (356/70). The dominant

fracture peak (164/82) is solely defined by joints and the joints do not have any logged infill. This may suggest these joints are geologically young compared to the fractures with logged mineral infill; these unfilled structures will be investigated further as site characterization continues.



Figure 56. Core from HFFI_5 (a: 859.1 – 870.19 m; b: 870.19 – 881.51 m). Biotite granodiorite-tonalite at the top of the interval with well-spaced fractures. Increasing fracture and alteration (silicification) intensity approaching the top contact of a feldspar-phyrlic tonalite dyke at 869.76 m (bottom of a). Increased alteration and fracture intensity continue through to ca. 875 m (b) where the biotite granodiorite-tonalite is less altered and fracture intensity decreases to the bottom of the interval.

Comparison of Fracture Orientations to Local Lineament Network

Fracture orientations in the borehole display some correlation to the dominant lineament trends that were interpreted using remote sensing data (DesRoches et al., 2018). Figure 57 displays the interpreted structural lineaments in proximity to IG_BH03. Northwest and northeast trends are most prominent in the rose diagram of lineament orientations (Figure 58). The northwest trend exhibits one well-defined, broad, peak. The northeast trend is characterized by multiple narrow, distinct, peaks. One distinct, east-trending lineament occurs to the southeast of the surface collar location of IG_BH03. Rose diagrams for both unweighted and Terzaghi-weighted borehole-logged fractures, with a minimum dip angle of 45°, are shown in Figure 59. Notwithstanding the broad spread in orientations, the same northwest and northeast peaks are evident in the borehole dataset.

Comparing the interpreted lineament trends with those of the interpreted fracture sets, and main structural orientations in the HFFIs, highlights further the similarity in orientations. The northeast-trending lineaments are consistent with the strike of fracture sets 2 and 6, the dominant structural orientation in HFFI 1, and one peak orientation of shear zones. The northwest-trending lineaments are consistent with the strike of fracture set 4, the dominant structural orientation in HFFI 3, and one peak orientation of shear zones. The east-trending lineament is consistent with the orientation of fracture set 5, the dominant structural orientation of HFFI 4 and HFFI 5, and one peak orientation of shear zones. These correlative borehole-interpreted fracture sets, and peak HFFI orientations, are subvertical to moderately inclined.

It is worth noting that the northeast trending lineaments parallel the dominant direction of glacial advance and retreat across the region. It is uncertain therefore whether all northeast trending interpreted lineaments reflect structurally significant features of the bedrock or if some are instead a product of glacial erosion. However, the understanding that the moderately to steeply inclined and northeast striking fracture sets 2 and 6 are present along the length of the borehole suggests that at least some of these lineaments do represent real bedrock structures.

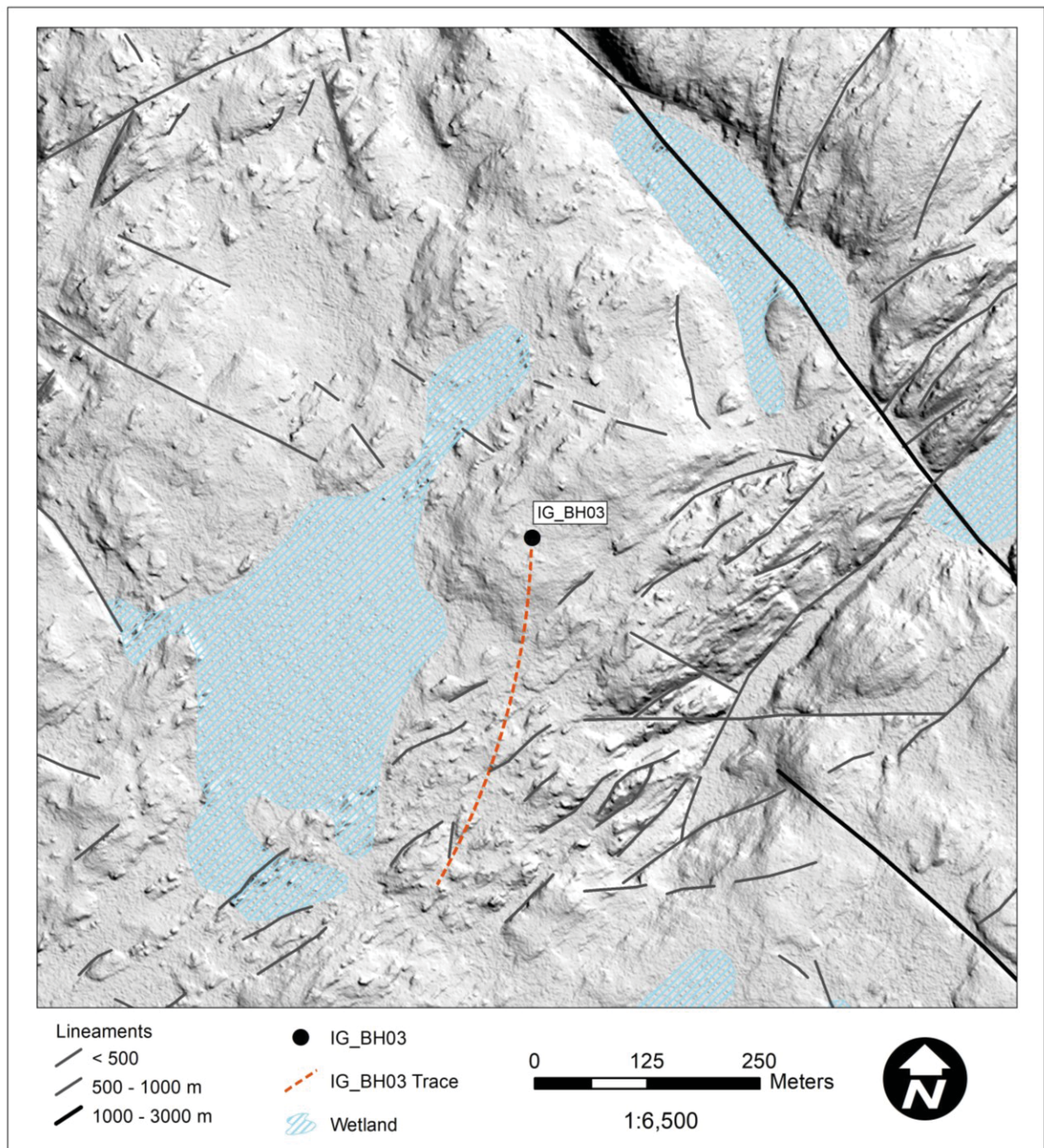


Figure 57: Lineament traces near IG_BH03 interpreted from LiDAR DEM and airborne geophysics data (DesRoches et al., 2018). Lineament traces are dominated by short length NE trending structures and fewer long NW trending structures.

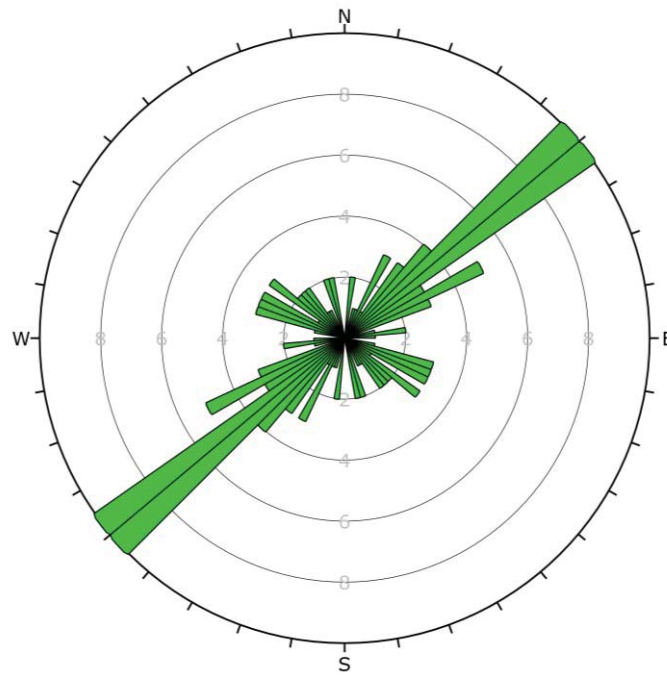


Figure 58: Rose diagram of the lineaments (N = 76) around IG_BH03 (see Figure 57) interpreted from LiDAR DEM and airborne geophysics data (DesRoches et al., 2018). Lineament orientations are plotted using a bin size of 5 degrees.

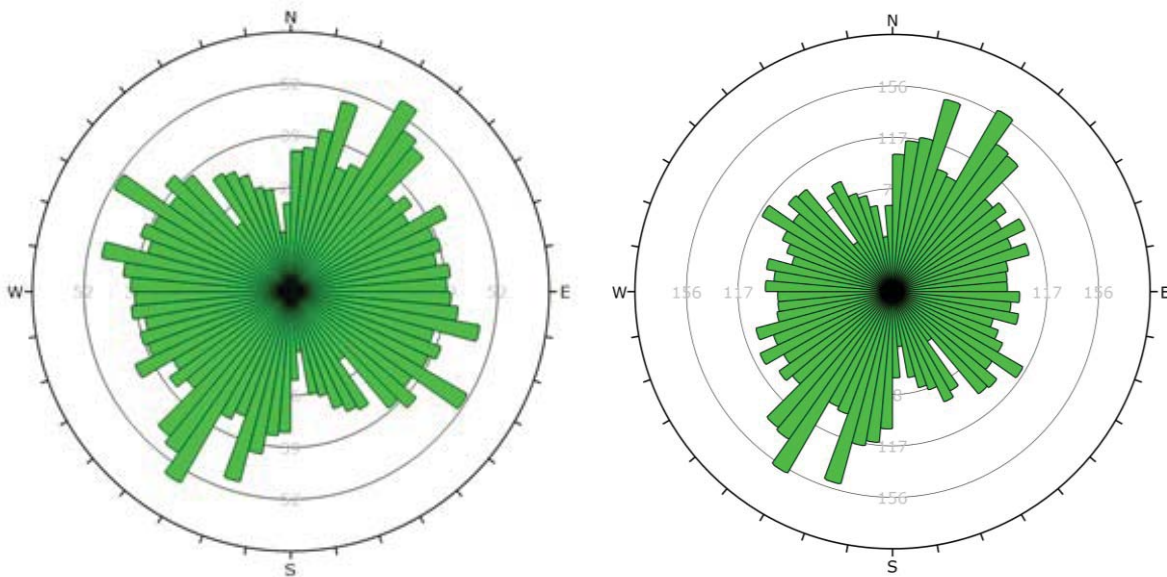


Figure 59: Rose diagrams of the borehole logged fracture orientations using a minimum dip angle of 45 degrees, and bin size of 5 degrees. Left: Unweighted (N = 1342). Right: Terzaghi-weighted to account for directional bias of the borehole path (weighted N = 2701).

4 SUMMARY OF FINDINGS AND UNCERTAINTIES

4.1 Findings

The geological findings are based on the geological information available to date, which are summarized in this report. One primary consideration is the understanding that the available information *is from a single borehole*. Whether or not the characteristics of the bedrock described throughout this report will transfer to other boreholes remains uncertain. However, the level of uncertainty related to the overall understanding of the bedrock across the study area will decrease as information from multiple boreholes are acquired and integrated together. A simplified summary of the geological model for IG_BH03 is presented below showing the final lithology log, rock units, per metre fracture frequency and structural units (Figure 60).

The bedrock intersected by IG_BH03 is homogeneous. IG_BH03 is dominated by a medium-grained rock of tonalitic to granodioritic composition, representing a total of 97.5 % of the recovered core. Optical and acoustic televiwer, natural and spectral gamma, gamma-gamma density and neutron geophysical logs provided additional evidence to distinguish subordinate rock types from the main rock types in this crystalline rock environment. The integration of visual core logging and geophysical logging was useful for developing the final interpretation of logged rock types and alteration and was critical for assigning true orientations to the logged structures.

The lithochemical and petrographic datasets provided mineral and rock chemistry information used to distinguish subtle variations between the felsic igneous rocks encountered in the borehole. Some of these distinctions were not evident based the geological and geophysical core logging alone. The majority of the felsic igneous rocks encountered share a similar mineralogy, ranging in composition between tonalite and granodiorite, except for a suite of dykes of granitic composition, (including aplite dykes).

Amphibolite was the most common subordinate rock type identified during borehole drilling. Amphibolite occurrences were predominantly observed within the lower half of the borehole as narrow (m-scale) units. Contact orientations for the amphibolite occurrences within this zone dip gently or moderately towards the north or dip steeply towards the northeast. Their distinct character and orientation, and overall distribution, suggests that similar zones of increased amphibolite occurrences may be traceable to other boreholes.

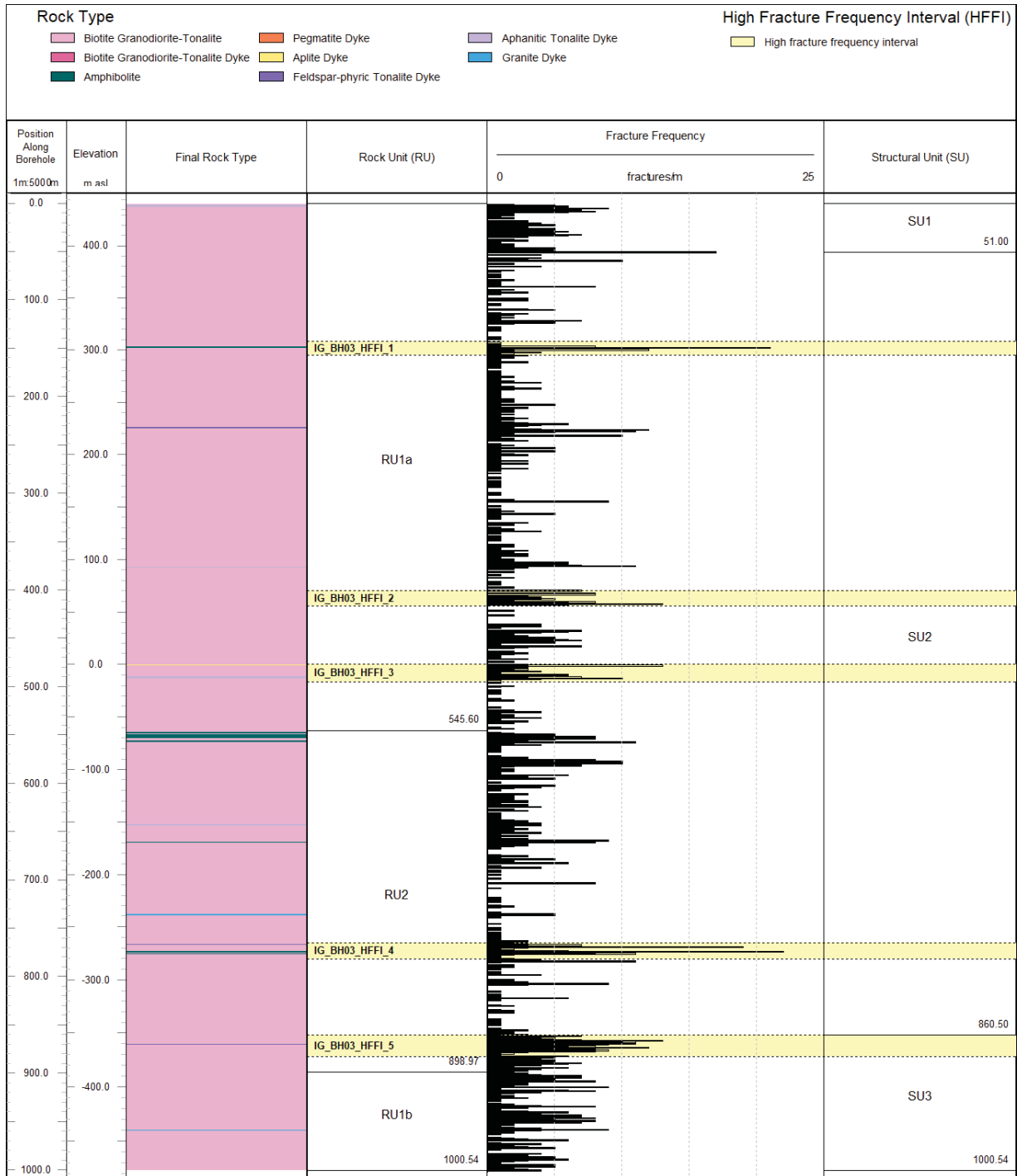


Figure 60: Summary log presenting final logged rock type, classification of rock units, fracture frequency per metre, and structural units. Data is plotted as position along borehole and elevation. This log represents the 1-dimensional geological model for IG_BH03.

Seven alteration types were logged in IG_BH03 over a total length of 623.35 m (62.3 %). The alteration types logged, in order of prevalence, were: potassic alteration, hematization, silicification, chloritization, bleaching, sericitization, and argillization. 478.46 m (47.8 %) of the recovered core was assigned as slightly altered (A2), where the alteration is generally confined to fractures with little or no penetration beyond the fracture plane. 133.8 m (13.4 %) was assigned as moderately

altered (A3), where alteration may penetrate into the wall rock and create an envelope or halo of alteration around a fracture plane. 11.09 m (1.1 %) was assigned as highly altered (A4), where alteration is pervasive causing a significant decrease in rock strength. At this point, it seems that the majority of the alteration observed in IG_BH03 is relatively weak and does not significantly impact the primary chemistry of the bedrock.

Based on broad changes in rock type along the length of the borehole three rock units were defined. The overall weak intensity of the identified alteration was not considered to be a useful characteristic for distinguishing the rock units. The majority of the borehole has a massive texture, with some subordinate rock types dominantly hosting ductile or brittle-ductile structure (foliation and shear zones). The presence or absence of ductile or brittle-ductile fabric was not considered to be a useful characteristic for defining rock units.

The structures identified in the borehole included features associated with ductile and brittle deformation processes. Ductile structure occurrences, including foliation and shear zones, are distributed along the entire length of the borehole. A foliation, defined by biotite, is predominantly weak and exhibits one prominent pole cluster that overlaps in orientation with the shear zones. Shear zones exhibit characteristics of both brittle and ductile deformation processes, including the local presence of fractures, primarily in association with amphibolite, and aphanitic or feldspar-phyric dyke, occurrences. The deformation manifests as cm- to dm-scale localized shear zones that are developed along, and sub-parallel to, their contacts. Overall an increased degree of ductile to brittle structural complexity is commonly associated with aphanitic and feldspar-phyric tonalite dyke, and amphibolite, occurrences suggesting that the presence of these subordinate rock types has served to focus fluid flow at some point in the geological past.

The complete fracture dataset appears to indicate the presence of six fracture sets:

- a subhorizontal to moderately inclined set, dipping north to north-northwest (fracture set 1);
- a moderately to steeply inclined set, dipping southeast (fracture set 2);
- a steeply inclined set, dipping west to west-northwest (fracture set 3a) and dipping east-southeast (fracture set 3b)
- a steeply inclined set, dipping southwest (fracture set 4a) and dipping northeast (fracture set 4b)
- a steeply inclined set, dipping south to south-southwest (fracture set 5a) and dipping north (fracture set 5b); and
- a steeply inclined set, dipping northwest (fracture set 6).

Joints are overwhelmingly the most common fracture type identified in the borehole, followed by veins and faults. Faults are consistently very narrow and exhibit only slight evidence of damage in the rock surrounding the fault plane.

Overall, the lineation dataset provides good indication that dip-slip motion predominates on gently to moderately inclined north to north-northeast dipping planes and nearly-transcurrent motion predominates on steeply inclined planes. Structures identified as faults and shear zones during geological core logging generally exhibit a similar history of motion, most prominently in a northwest-southeast direction. It remains unknown at this point what the shortening and extension directions were, and whether the observed planes and lineations formed contemporaneously under the same stress regime or at different times under different orientations of applied stress. Future boreholes and surface mapping campaigns will attempt to clarify these outstanding questions.

The borehole was subdivided into three structural units based on variation in fracture frequency log and slope of the cumulative fracture frequency curve resulting in average fracture frequencies for the structural units ranging between 1.61 and 3.51 fractures per metre.

Five high fracture frequency intervals (HFFIs) were defined along the borehole using a semi-automated approach applied to the borehole fracture frequency per metre log. The intervals range in width from just over 15 m to 22.5 m. The shallowest HFFI occurs at around 150 m, the next two occur between 400 and 500 m and the deepest two occur between 750 and 900 m. All HFFIs, except the one at around 400 m, include at least one subordinate rock type occurrence. The most common subordinate rock types represented are the aphanitic or feldspar-phyric tonalite dykes, and amphibolite.

Logged structures, defined fracture sets, and HFFIs, in the borehole display some correlation to the dominant lineament trends in proximity to the borehole. The northeast-trending lineaments are consistent with the strike of fracture sets 2 and 6, the dominant structural orientation in HFFI 1, and one peak orientation of shear zones. The northwest-trending lineaments are consistent with the strike of fracture set 4, the dominant structural orientation in HFFI 3, and one peak orientation of shear zones. The east-trending lineament is consistent with the orientation of fracture set 5, the dominant structural orientation of HFFI 4 and HFFI 5, and one peak orientation of shear zones. These correlative borehole-interpreted fracture sets, and peak HFFI orientations, are subvertical to moderately inclined. Therefore, it is possible that some interpreted lineaments currently interpreted to represent vertically oriented fracture zones, in particular northeast and east trending lineaments, could instead have steep to moderate dips.

Considering all of the geological observations described throughout the report, several key summary points are highlighted below. These observations align with a developing understanding that, while the rock is homogeneous overall, there are distinct regions along the borehole that have relatively distinct character, including that:

- there is a cluster of fractures and shear zones below approximately 850 m,
- aphanitic and feldspar-phyric tonalite dykes, and amphibolite, cluster in the lower half of the borehole,
- both aphanitic and feldspar-phyric tonalite dykes, and amphibolite, shows evidence of ductile strain and brittle deformation internally and along their contacts, as well as evidence of hematization and chloritization, and
- there is relatively broad consistency in fracture frequency along the entire length of the borehole.

The significance of the geological relationships identified here, will continue to be explored as additional information is gathered from future surface and subsurface investigations, including the drilling of additional boreholes and two-dimensional and vertical seismic profiling.

4.2 Uncertainties

With subsurface information available from only one borehole, many geological uncertainties remain. With respect to the distribution of distinct rock types, a key uncertainty relates to the nature of the amphibolite occurrences. Are these deformed mafic dykes or vestiges of greenstone belt material? Contact relationships are unclear due to localization of strain at the amphibolite margins, and litho-geochemistry results are so far inconclusive. The distribution of the amphibolite and the other subordinate rock types in three-dimensions is also a remaining uncertainty. Regarding the significance of the logged alteration, it is acknowledged that some uncertainty remains regarding the significance of the few intervals of higher intensity alteration to the overall character of the bedrock.

With respect to structure, there is uncertainty in the true density and mean orientation of steeply dipping structures. Although a Terzaghi-weighting was applied to correct for borehole orientation bias, it is understood that there are other techniques available. Further exploration of the best approach to take to remove the borehole orientation bias will be investigated as additional data becomes available, including from differently oriented angled boreholes. Whether or not the drilling

activity itself, or stress relief, may have induced the broken character of logged fractures remains an uncertainty. The true nature of logged televiewer-only and core-only structures also remains uncertain. There is uncertainty as to whether the steeply dipping fracture sets 3a and 3b, which strike nearly parallel to the trend of the borehole, represent shallower dipping members of an under-represented sub-vertical fracture set. In addition, the timing and number of stages of fracture development (and re-activation), mineral infilling and alteration, and the resulting implications for the geological history of the area remain uncertain.

The subset of identified fractures that are likely to be hydraulically conductive also remains uncertain. This is especially important in understanding the significance of logged geological apertures. As mentioned above, geological apertures are estimated values only because there are multiple possible sources of uncertainty in how a reported aperture value relates to the true aperture of a fracture identified as broken. There are uncertainties related to measurement inaccuracy, including where the opening is very small, where the opposing fracture planes are not parallel or fit poorly together, or due to limits in televiewer resolution. In addition, effects due to drilling or decompression may create or enhance the visible open space identified as aperture. Finally, aperture measured in core or on a borehole wall is only a local aperture that is not necessarily representative over the entire fracture length. There are also cases where fractures are logged as broken but exhibit no measurable geological aperture. Additional analysis of the observed structures in the acoustic and optical televiewer datasets, including fractures and their characteristics (e.g., broken vs intact nature, mineral infilling, orientation), will aim to reduce these uncertainties.

The absolute dimensions of the rock units (RU) and structural units (SU) presented above were defined based on a subjective and non-unique approach. With the same data inputs, alternative approaches may have defined more or less units and ultimately produced a different geological model for the borehole. Finally, a statistically robust method was used to define the high fracture frequency intervals (HFFI) along the borehole. However, the approach is still non-unique. Different analytical approaches may produce a different result. Furthermore, the broader geological significance of these intervals, identified along a single borehole, remains uncertain.

5 REFERENCES

- American Petroleum Institute (API), 1985. Directional Drilling Survey Calculation Methods and Terminology (Bulletin No. D20). Dallas, TX.
- Blackburn, C.E., Hinz, P., 1996. Kenora Resident Geologist's District (Open File Report No. 5958), Report of Activities 1996, Resident Geologists. Ontario Geological Survey.
- Daniels, J.J., Olhoeft, G.R., Scott, J.H., 1984. Interpretation of core and well log physical property data from drill hole UPH-3, Stephenson County, Illinois (USGS Numbered Series No. 82-941). United States Geological Survey.
- Davy, P., Darcel, C., Bour, O., Munier, R., De Dreuzy, J.-R., 2006. A note on the angular correction applied to fracture intensity profiles along drill core. *Journal of Geophysical Research: Solid Earth* 111, B11408. <https://doi.org/10.1029/2005JB004121>
- DesRoches, A., Sykes, M., Parmenter, A., Sykes, E., 2018. Lineament Interpretation of the Revell Batholith and Surrounding Greenstone Belts (No. NWMO-TR-2018-19). Nuclear Waste Management Organization.
- Debon, F., Le Fort, P., 1983. A chemical and mineralogical classification of common plutonic rocks and associations. *Earth and Environmental Science Transactions of the Royal Society of Edinburgh* 73, 135-149.
- Golder Associates Ltd., 2015. Phase 2 Geoscientific Preliminary Assessment, Findings from Initial Field Studies: Township of Ignace, Ontario (No. APM-REP-06145-0001). Nuclear Waste Management Organization.
- Golder Associates Ltd., 2017. Phase 2 Initial Borehole Drilling and Testing, Ignace Area: Initial Borehole Characterization Plan for IG_BH01 (No. APM-PLAN-01332-0242). Nuclear Waste Management Organization.
- Golder Associates Ltd., 2020a. Phase 2 Initial Borehole Drilling and Testing, Ignace Area. WP02 Data Report - Borehole Drilling and Coring for IG_BH303 (No. APM-REP-01332-0241). Nuclear Waste Management Organization.
- Golder Associates Ltd., 2020b. Phase 2 Initial Borehole Drilling and Testing, Ignace Area. WP05 Data Report - Geophysical Well Logging for IG_BH03 (No. APM-REP-01332-0248). Nuclear Waste Management Organization.
- Golder Associates Ltd., 2020c. Phase 2 Initial Borehole Drilling and Testing, Ignace Area. WP03 Data Report - Geological and Geotechnical Core Logging, Photography and Sampling for IG_BH03 (No. APM-REP-01332-0250). Nuclear Waste Management Organization.
- Golder Associates Ltd., 2021a. Phase 2 Initial Borehole Drilling and Testing, Ignace Area. WP04C Data Report - Porewater Extraction and Analysis and Petrographic Analysis for IG_BH03 (No. APM-REP-01332-0246). Nuclear Waste Management Organization.
- Golder Associates Ltd., 2021b. Phase 2 Initial Borehole Drilling and Testing, Ignace Area. WP06 Data Report - Hydraulic Testing for IG_BH03 (No. APM-REP-01332-0255). Nuclear Waste Management Organization.
- Golder Associates Ltd., 2021c. Phase 2 Initial Borehole Drilling and Testing, Ignace Area. WP07 Data Report - Opportunistic Groundwater Sampling for IG_BH03 (No. APM-REP-01332-0253). Nuclear Waste Management Organization.
- Golder Associates Ltd., 2021d. Phase 2 Initial Borehole Drilling and Testing, Ignace Area. WP09 Data Report - Westbay MP38 Casing Completion for IG_BH03 (No. APM-REP-01332-0259). Nuclear Waste Management Organization.

- Golder Associates Ltd., 2022. Phase 2 Initial Borehole Drilling and Testing, Ignace Area. WP04B Data Report - Geomechanical Testing of Core for IG_BH03 (No. APM-REP-01332-0252). Nuclear Waste Management Organization.
- Golder Associates Ltd., Patterson Grant and Watson, Ltd., 2017. Phase 2 Geoscientific Preliminary Assessment: Geological Mapping, Township of Ignace and Area, Ontario (No. APM-REP-01332-0225). Nuclear Waste Management Organization.
- Halla, J., 2018. Highlights on Geochemical Changes in Archaean Granitoids and Their Implications for Early Earth Geodynamics. *Geosciences* 8, 353. <https://doi.org/10.3390/geosciences8090353>
- Halla, J., van Hunen, J., Heilimo, E., Hölttä, P., 2009. Geochemical and numerical constraints on Neoproterozoic plate tectonics. *Precambrian Research* 174, 155–162. <https://doi.org/10.1016/j.precamres.2009.07.008>
- Hewitt, D.F., 1967. Pegmatite Mineral Resources of Ontario. Industrial Mineral Report 21. Ontario Department of Mines, pg. 83.
- Holm, P.E., 1982. Non-recognition of continental tholeiites using the Ti-Y-Zr diagram: Contributions to Mineralogy and Petrology 79, 308-310.
- Keys, W.S., 1997. A Practical Guide to Borehole Geophysics in Environmental Investigations. CRC Press.
- Large, R.R., Gemmell, J.B., Paulick, H., Huston, D.L., 2001. The alteration box plot: A simple approach to understanding the relationship between alteration mineralogy and lithogeochemistry associated with volcanic-hosted massive sulfide deposits. *Economic Geology* 96, 957-972.
- Le Bas, M.J., Streckeisen, A.L., 1991. The IUGS systematics of igneous rocks. *Journal of the Geological Society* 148, 825–833. <https://doi.org/10.1144/gsjgs.148.5.0825>
- Parmenter, A., Waffle, L., DesRoches, A., Carvalho, J., Neufeld, A. 2022. Phase 2 Initial Borehole Drilling and Testing, Ignace Area. WP10 – Geological Integration Report for IG_BH01 (No. APM-REP-01332-0260). Nuclear Waste Management Organization.
- Parmenter, A., DesRoches, A., Sykes, M., Sykes, E., 2020. Bedrock geology of the Revell batholith and surrounding greenstone belts (No. NWMO-TR-2020-08). Nuclear Waste Management Organization.
- Pearce, J.A., 1996. A User's Guide to Basalt Discrimination, in: Trace Element Geochemistry of Volcanic Rocks: Applications for Massive Sulphide Exploration. Geological Association of Canada: Short Course Notes 12, 79-113.
- Raymond, L.A., 2002. Chapter 6: Basalt and Ultramafic Rocks, in: Petrology: The Study of Igneous, Sedimentary, and Metamorphic Rocks. McGraw-Hill Science, Engineering & Mathematics.
- Sander Geophysics Limited (SGL), 2015. Phase 2 Geoscientific Preliminary Assessment, Acquisition, Processing and Interpretation of High-Resolution Airborne Geophysical Data (No. APM-REP-06145-0002). Nuclear Waste Management Organization.
- SRK Consulting, Inc., Golder Associates Ltd., 2015. Phase 2 Geoscientific Preliminary Assessment, Observation of General Geological Features, Township of Ignace, Ontario (No. APM-REP-06145-0004). Nuclear Waste Management Organization.
- Stone, D., 2010a. Geology of the Stormy Lake Area, Northwestern Ontario, Project Unit 09-003 (Open File Report No. 6260), Summary of Field Work and Other Activities 2010. Ontario Geological Survey, Sudbury, Canada.
- Stone, D., 2010b. Precambrian geology of the central Wabigoon Subprovince area, northwestern Ontario (Open File Report No. 5422). Ontario Geological Survey.
- Stone, D., 2009. Geology of the Bending Lake Area, Northwestern Ontario (Open File Report No. 6240), Summary of Field Work and Other Activities 2009. Ontario Geological Survey, Sudbury, Canada.

- Stone, D., Davis, D.W., Hamilton, M.A., Falcon, A., 2010. Interpretation of 2009 Geochronology in the Central Wabigoon Subprovince and Bending Lake Areas, Northwestern Ontario, Project Unit 09-003 (Open File Report No. 6260), Summary of Field Work and Other Activities 2010. Ontario Geological Survey.
- Stone, D., Halle, J., Chaloux, E., 1998. Geology of the Ignace and Pekagoning Lake Areas, Central Wabigoon Subprovince (Misc. Paper No. 169), Summary of Field Work and Other Activities 1998. Ontario Geological Survey.
- Taylor, S.R., McLennan, S.M., 1985. The continental crust: Its composition and evolution. United States.
- Terzaghi, R.D., 1965. Sources of Error in Joint Surveys. *Géotechnique* 15, 287–304.
<https://doi.org/10.1680/geot.1965.15.3.287>
- Virtanen, P. et al. 2020. SciPy 1.0--Fundamental Algorithms for Scientific Computing in Python. *Nature Methods*, 17, 261–272.
- Williams, N.C., and Davidson, G.J., 2004. Possible submarine advanced argillic alteration at the Basin Lake prospect, Western Tasmania, Australia. *Economic Geology* 99, 987-1002.
- Winchester, J.A., Floyd, P.A., 1976. Geochemical discrimination of different magma series and their differentiation products using immobile elements. *Chemical Geology* 20, 325-343.

**Appendix A: Summary List of Work
Packages Completed for IG_BH03**

WP Number	WP Name	Report Reference
WP01	Site Infrastructure and Access Road Construction	No report
WP02	Borehole Drilling and Coring	Golder, 2020a
WP03	Geological and Geotechnical Core Logging, Photography and Sampling	Golder, 2020c
WP04a2	Effective Diffusion Coefficients – Crystalline Rock	Golder, in prep.
WP04b	Geomechanical Testing of Core	Golder, 2022
WP04c	Porewater Extraction and Analysis and Petrographic Analysis	Golder, 2021a
WP05	Geophysical Well Logging and Interpretation	Golder, 2020b
WP06	Hydraulic Testing	Golder, 2021b
WP07	Opportunistic Groundwater Sampling and Testing	Golder, 2021c
WP08	Temporary Well Sealing	No report
WP09	Westbay MP38 Multi-Level Groundwater Monitoring System Installation	Golder, 2021d

**Appendix B: Petrography and
lithogeochemistry data**

Petrography

Semi-quantitative optical petrography was completed by Activation Laboratories in Thunder Bay, Ontario (LGXXX). Modal mineralogy was determined using a known scale grid and visually determining area coverage of minerals in the sample. Note that only rock types plotted on the QAP diagram (Figure 8) are listed.

Modal mineralogy (original and normalized) presented as percentages, determined semi-quantitatively using polished thin sections.

Sample ID	From (position along borehole; m)	To (position along borehole; m)	Point-count %			Total	Normalized %			Total	Final Rock Type
			PLA	QTZ	AFS		PLA	QTZ	AFS		
IG_BH03_LG004	184.72	184.83	39	41	8.5	88.5	44.1	46.3	9.6	100	Aplite dyke
IG_BH03_LG005	231.97	232.16	21.5	39	0	60.5	35.5	64.5	0	100	Feldspar-phyric tonalite dyke
IG_BH03_LG006	363.51	363.73	45	36	13	94	47.9	38.3	13.8	100	Biotite granodiorite-tonalite
IG_BH03_LG007	477.80	477.98	39	34	27	100	39	34	27	100	Aplite dyke
IG_BH03_LG008	489.97	490.15	37	22	0	59	62.7	37.3	0	100	Feldspar-phyric tonalite dyke
IG_BH03_LG009	546.75	546.94	56	46	0	102	54.9	45.1	0	100	Biotite granodiorite-tonalite
IG_BH03_LG011	553.20	553.49	49	45	6	100	49	45	6	100	Biotite granodiorite-tonalite
IG_BH03_LG013	642.75	642.89	56	17.5	0	73.5	76.2	23.8	0	100	Aphanitic tonalite dyke
IG_BH03_LG015	735.49	735.70	41	38	22.5	101.5	40.4	37.4	22.2	100	Granite dyke
IG_BH03_LG016	765.90	766.05	72.5	15	0	87.5	82.9	17.1	0	100	Feldspar-phyric tonalite dyke
IG_BH03_LG017	774.08	774.25	69	28	0	97	71.1	28.9	0	100	Biotite granodiorite-tonalite
IG_BH03_LG019	867.73	867.90	55	41	3	99	55.6	41.4	3.0	100	Biotite granodiorite-tonalite
IG_BH03_LG020	889.70	889.90	41	36	4.5	81.5	50.3	44.2	5.5	100	Biotite granodiorite-tonalite
IG_BH03_LG021	957.50	957.70	61	17.5	0	78.5	77.7	22.3	0	100	Feldspar-phyric tonalite dyke
IG_BH03_LG022	958.37	958.58	48	41	12.5	101.5	47.3	40.4	12.3	100	Granite dyke

Litho geochemistry

All analyses performed by Activation Laboratories Ltd. in Thunder Bay or Ancaster, Ontario. In addition to the results included below, 63 certified reference materials (to measure accuracy), 7 duplicates (to measure precision), and 18 method blanks (to monitor contamination) were analysed by Actlabs to ensure overall quality control in the litho geochemical analyses. Certified reference material (CRM) measurements averaged within 0.1 % of certified values (>99 % accuracy). There were a few CRM samples that were >10% off their certified values in one element, but other elements in the material were within an acceptable range of > 90% accuracy so these discrepancies were deemed insignificant. Duplicate sample measurements averaged within 7 % of original measured values (>93% precision), and the method blanks all returned measurements below, or within an acceptable range of, detection limit (no discernable contamination).

Litho geochemical results of various tests carried out by Activation Laboratories. For details on each analysis performed, see section 3.2.1.

Report Number: A20-05149																								
Report Date: 18/6/2020																								
Analyte Symbol	From (position along borehole; m)	To (position along borehole; m)	Au	As	Br	Cr	Ir	Sc	Se	Sb	Mass	SiO ₂	Al ₂ O ₃	Fe ₂ O ₃ (T)	MnO	MgO	CaO	Na ₂ O	K ₂ O	TiO ₂	P ₂ O ₅	LOI	Total	
Unit Symbol			ppb	ppm	ppm	ppm	ppb	ppm	ppm	ppm	ppm	g	%	%	%	%	%	%	%	%	%	%	%	%
Detection Limit			2	0.5	0.5	5	5	0.1	3	0.2		0.01	0.01	0.01	0.001	0.01	0.01	0.01	0.01	0.01	0.001	0.01		0.01
Analysis Method			INAA	INAA	INAA	INAA	INAA	INAA	INAA	INAA	INAA	INAA	FUS-ICP	FUS-ICP	FUS-ICP	FUS-ICP	FUS-ICP	FUS-ICP	FUS-ICP	FUS-ICP	FUS-ICP	FUS-ICP	GRAV	FUS-ICP
IG_BH03_LG001	74.00	74.30	< 2	< 0.5	< 0.5	27	< 5	2	< 3	< 0.2	1.06	73.39	14.24	1.77	0.03	0.39	1.99	4.52	2.46	0.189	0.06	0.6	99.64	
IG_BH03_LG002	131.01	131.25	< 2	< 0.5	< 0.5	28	< 5	2.1	< 3	< 0.2	1.04	72.92	13.84	1.77	0.032	0.38	1.99	4.54	2.21	0.183	0.05	0.59	98.51	
IG_BH03_LG003	149.48	149.64	< 2	0.9	< 0.5	369	< 5	16.6	< 3	< 0.2	34	53.93	13.46	8.28	0.125	7.9	8.18	3.24	2.12	0.728	0.2	2.08	100.2	
IG_BH03_LG004	184.72	184.83	< 2	0.9	< 0.5	18	< 5	1.2	< 3	< 0.2	32.7	77.01	12.83	0.9	0.022	0.17	0.5	4.14	4.61	0.077	0.01	0.27	100.5	
IG_BH03_LG005	231.97	232.16	< 2	0.6	< 0.5	21	< 5	4	< 3	< 0.2	36.4	71.09	14.53	3.22	0.04	0.81	3.17	4.26	1.86	0.447	0.12	0.5	100.1	
IG_BH03_LG006	363.51	363.73	< 2	< 0.5	6.5	17	< 5	2.2	< 3	< 0.2	34	72.26	14.69	1.67	0.023	0.37	1.31	4.27	3.33	0.164	0.05	1.27	99.4	
IG_BH03_LG007	477.80	477.98	< 2	< 0.5	1.7	20	< 5	0.7	< 3	< 0.2	32.5	75.89	12.9	0.59	0.014	0.06	0.51	4.42	4.28	0.036	<0.01	0.33	99.04	
IG_BH03_LG008	489.97	490.15	< 2	< 0.5	< 0.5	46	< 5	4.1	< 3	< 0.2	34.2	71.43	14.98	3.01	0.041	0.85	3.32	4.41	1.64	0.331	0.1	0.54	100.6	
IG_BH03_LG009	546.75	546.94	3	< 0.5	< 0.5	26	< 5	2	< 3	< 0.2	34.4	74.22	14.14	1.76	0.029	0.4	1.92	4.36	2.36	0.184	0.05	0.87	100.3	
IG_BH03_LG010	547.37	547.55	< 2	< 0.5	< 0.5	949	< 5	20.2	< 3	< 0.2	35.6	51.35	12.14	8.67	0.144	10.19	8.32	2.67	2.63	0.629	0.18	3.32	100.3	
IG_BH03_LG011	553.20	553.49	< 2	< 0.5	< 0.5	18	< 5	2	< 3	< 0.2	33.3	74.49	14.17	1.85	0.032	0.41	2.1	4.45	2.38	0.195	0.05	0.67	100.8	
IG_BH03_LG012	569.01	569.17	< 2	1.3	< 0.5	21	< 5	2	< 3	0.2	1.06	73.41	13.76	1.8	0.03	0.39	2.05	4.36	2.54	0.192	0.05	0.52	99.1	
IG_BH03_LG013	642.75	642.89	< 2	< 0.5	< 0.5	31	< 5	4	< 3	< 0.2	35.8	70.92	14.61	2.95	0.04	0.84	3.38	4.31	1.62	0.328	0.09	0.62	99.7	
IG_BH03_LG014	655.00	655.28	< 2	< 0.5	< 0.5	15	< 5	2	< 3	< 0.2	1.06	73.85	13.92	1.85	0.032	0.39	2.11	4.52	2.37	0.196	0.06	0.46	99.75	

IG_BH03_LG015	735.49	735.70	< 2	< 0.5	17.6	20	< 5	1.2	< 3	< 0.2	34.8	77.24	12.93	0.6	0.022	0.05	0.41	4.47	4.47	0.034	0.01	0.28	100.5
IG_BH03_LG016	765.90	766.05	< 2	1.5	< 0.5	30	< 5	2.3	< 3	< 0.2	34.9	73.14	14.64	2.01	0.03	0.44	2.59	4.55	1.89	0.213	0.06	0.42	99.98
IG_BH03_LG017	774.08	774.25	< 2	1	< 0.5	27	< 5	2	< 3	< 0.2	34.7	73.91	14.32	1.87	0.032	0.45	2.14	6.01	0.74	0.2	0.05	0.85	100.6
IG_BH03_LG018	774.53	774.69	< 2	< 0.5	< 0.5	650	< 5	28.6	< 3	< 0.2	39.7	44.69	10.31	10.71	0.172	15.61	10.16	0.69	2.66	0.895	0.45	3.8	100.2
IG_BH03_LG019	867.73	867.90	< 2	< 0.5	12.2	30	< 5	2.2	< 3	< 0.2	33.9	73.7	14.16	1.91	0.028	0.47	2.03	4.84	1.79	0.209	0.05	1.57	100.8
IG_BH03_LG020	889.70	889.90	< 2	< 0.5	12	16	< 5	2.1	< 3	< 0.2	32.9	73.5	14.31	1.9	0.03	0.42	2.28	4.55	2.4	0.209	0.06	0.98	100.7
IG_BH03_LG021	957.50	957.70	< 2	< 0.5	< 0.5	23	< 5	3.5	< 3	< 0.2	36.8	70.13	14.33	3.02	0.037	0.79	3.08	4.65	1.52	0.407	0.1	1.52	99.58
IG_BH03_LG022	958.37	958.58	< 2	< 0.5	5.5	21	< 5	0.6	< 3	< 0.2	33.2	76.99	12.8	0.58	0.013	0.05	0.62	4.53	3.5	0.036	<0.01	0.6	99.73

Analyte Symbol	Sc	Be	V	Cr	Co	Ni	Cu	Zn	Cd	S	Ga	Ge	As	Rb	Sr	Y	Zr	Nb	Mo	Ag	In	Sn	Sb	Cs	Ba
Unit Symbol	ppm	ppm	ppm	ppm	ppm	ppm	ppm	ppm	ppm	%	ppm	ppm	ppm	ppm	ppm	ppm	ppm	ppm	ppm	ppm	ppm	ppm	ppm	ppm	ppm
Detection Limit	1	1	5	20	1	1	1	1	0.5	0.001	1	0.5	5	1	2	0.5	1	0.2	2	0.3	0.1	1	0.2	0.1	2
Analysis Method	FUS-ICP	FUS-ICP	FUS-ICP	FUS-MS	FUS-MS	TD-ICP	TD-ICP	TD-ICP	TD-ICP	TD-ICP	FUS-MS	FUS-MS	FUS-MS	FUS-MS	FUS-ICP	FUS-MS	FUS-ICP	FUS-MS	FUS-MS	TD-ICP	FUS-MS	FUS-MS	FUS-MS	FUS-MS	FUS-ICP
IG_BH03_LG001	2	1	14	20	2	3	10	52	< 0.5	0.002	18	1	< 5	81	219	4.3	109	4.4	< 2	0.4	< 0.1	1	< 0.2	3	493
IG_BH03_LG002	2	1	13	20	2	2	10	51	< 0.5	0.004	18	1	< 5	76	208	5.2	111	4.7	< 2	< 0.3	< 0.1	1	< 0.2	2.8	453
IG_BH03_LG003	19	1	175	430	33	228	15	101	< 0.5	0.003	17	1.2	< 5	78	575	13.5	104	4.1	< 2	< 0.3	< 0.1	1	< 0.2	9	417
IG_BH03_LG004	1	2	< 5	< 20	1	1	11	27	< 0.5	0.002	19	1.8	< 5	172	21	8.5	22	4.2	< 2	< 0.3	< 0.1	1	< 0.2	3.9	46
IG_BH03_LG005	4	1	34	20	6	7	17	70	< 0.5	0.006	19	0.9	< 5	57	250	6.5	165	6.4	< 2	0.3	< 0.1	1	< 0.2	1.5	447
IG_BH03_LG006	2	1	18	< 20	2	2	18	38	< 0.5	0.003	20	0.9	< 5	109	171	3.6	101	4.9	< 2	< 0.3	< 0.1	1	< 0.2	1.8	930
IG_BH03_LG007	< 1	1	< 5	< 20	< 1	< 1	8	20	< 0.5	0.004	17	1.4	< 5	162	15	7.7	14	2.5	< 2	< 0.3	< 0.1	< 1	< 0.2	2.3	16
IG_BH03_LG008	4	< 1	36	50	6	7	16	66	< 0.5	0.005	18	0.8	< 5	49	253	4.9	140	4.2	< 2	0.4	< 0.1	1	< 0.2	1.3	400
IG_BH03_LG009	2	< 1	13	30	2	1	9	48	< 0.5	0.003	18	0.9	< 5	73	224	4.2	99	3.7	< 2	0.4	< 0.1	1	< 0.2	1.5	636
IG_BH03_LG010	23	1	179	1110	42	229	20	77	< 0.5	0.006	14	1.3	< 5	82	519	13.8	91	5.2	< 2	< 0.3	< 0.1	1	< 0.2	4.8	656
IG_BH03_LG011	2	1	16	20	3	3	27	53	< 0.5	0.003	18	0.9	< 5	76	220	4.2	106	4.3	2	0.4	< 0.1	1	< 0.2	2.2	509
IG_BH03_LG012	2	< 1	14	20	2	3	8	50	< 0.5	0.002	18	0.9	< 5	78	218	4.1	106	4	< 2	0.3	< 0.1	1	< 0.2	2	605
IG_BH03_LG013	4	< 1	35	40	6	5	19	67	< 0.5	0.008	18	0.8	< 5	48	250	4.8	145	4.1	< 2	0.4	< 0.1	1	< 0.2	1.2	400
IG_BH03_LG014	2	1	15	< 20	3	3	8	51	< 0.5	0.003	18	0.9	< 5	83	222	4.2	109	4.6	< 2	< 0.3	< 0.1	1	< 0.2	2.6	500
IG_BH03_LG015	1	< 1	< 5	20	< 1	< 1	3	13	< 0.5	0.01	18	1.8	< 5	200	8	16.2	31	3.4	< 2	< 0.3	< 0.1	< 1	0.2	2.2	7
IG_BH03_LG016	2	< 1	18	20	3	2	31	59	< 0.5	0.006	17	0.8	< 5	69	245	3.5	111	3.3	< 2	0.4	< 0.1	1	< 0.2	1.9	513
IG_BH03_LG017	2	1	15	30	3	3	48	39	< 0.5	0.007	18	0.8	< 5	24	339	4.3	115	4.7	< 2	0.6	< 0.1	1	< 0.2	0.8	623
IG_BH03_LG018	31	1	206	720	62	535	13	86	< 0.5	0.02	12	1.4	< 5	73	416	17.7	118	6.2	< 2	< 0.3	< 0.1	1	< 0.2	4.5	629
IG_BH03_LG019	2	1	15	20	3	4	25	34	< 0.5	0.006	18	0.9	< 5	58	243	4.2	120	4.5	< 2	< 0.3	< 0.1	1	< 0.2	1	390
IG_BH03_LG020	2	1	16	20	3	1	11	37	< 0.5	0.004	18	0.9	< 5	69	242	3.9	122	4.5	< 2	0.4	< 0.1	1	< 0.2	1.1	574
IG_BH03_LG021	4	1	32	30	6	7	23	68	< 0.5	0.015	18	0.8	< 5	50	264	5.8	163	6.1	< 2	< 0.3	< 0.1	1	< 0.2	2.6	452
IG_BH03_LG022	< 1	< 1	< 5	30	< 1	2	6	12	< 0.5	0.054	16	1.3	< 5	99	49	5.1	23	2.8	< 2	< 0.3	< 0.1	< 1	< 0.2	1.1	62

Analyte Symbol	La	Ce	Pr	Nd	Sm	Eu	Gd	Tb	Dy	Ho	Er	Tm	Yb	Lu	Hf	Ta	W	Tl	Pb	Li	Bi	Th	U
Unit Symbol	ppm																						
Detection Limit	0.05	0.05	0.01	0.05	0.01	0.005	0.01	0.01	0.01	0.01	0.01	0.005	0.01	0.002	0.1	0.01	0.5	0.05	5	1	0.1	0.05	0.01
Analysis Method	FUS-MS	TD-ICP	TD-ICP	FUS-MS	FUS-MS	FUS-MS																	
IG_BH03_LG001	20.2	34.8	3.39	11.5	2.03	0.501	1.5	0.18	0.87	0.14	0.37	0.049	0.3	0.044	3.2	0.71	0.9	0.39	8	71	< 0.1	5.75	1.71
IG_BH03_LG002	19.4	34.1	3.4	11.5	1.99	0.44	1.54	0.19	1.01	0.16	0.44	0.062	0.36	0.05	3.2	0.84	< 0.5	0.34	6	66	< 0.1	6.2	2.63
IG_BH03_LG003	30.7	65.7	7.63	29.8	5.53	1.45	4.05	0.51	2.55	0.44	1.26	0.169	1.08	0.161	2.9	0.26	< 0.5	0.34	19	143	0.1	4.06	1.09
IG_BH03_LG004	2.83	6.25	0.68	2.53	0.87	0.114	0.95	0.2	1.35	0.24	0.68	0.1	0.64	0.09	1.8	1.05	0.5	0.62	17	30	0.2	1.72	6.38
IG_BH03_LG005	22.8	41.8	4.29	15.4	2.77	0.819	2.03	0.25	1.31	0.23	0.58	0.079	0.51	0.072	4.2	0.63	< 0.5	0.32	8	91	< 0.1	4.97	1.29
IG_BH03_LG006	15.1	27.9	2.7	8.96	1.61	0.323	1.13	0.15	0.72	0.13	0.31	0.041	0.23	0.033	3.4	0.71	< 0.5	0.43	9	86	< 0.1	4.73	1.54
IG_BH03_LG007	5.52	10.7	1.11	3.63	0.9	0.123	0.98	0.19	1.31	0.25	0.73	0.1	0.61	0.085	1	0.74	< 0.5	0.65	18	10	< 0.1	2.01	1.57
IG_BH03_LG008	19.3	34.2	3.51	12.7	2.14	0.621	1.52	0.19	0.94	0.16	0.42	0.059	0.38	0.055	3.6	0.49	< 0.5	0.28	< 5	77	< 0.1	4.35	1.09
IG_BH03_LG009	18.1	31.5	3.17	10.4	1.82	0.504	1.27	0.17	0.84	0.14	0.32	0.044	0.29	0.046	2.7	0.62	< 0.5	0.28	7	35	< 0.1	5.31	1.28
IG_BH03_LG010	25	52.4	6.21	25	4.77	1.3	3.7	0.49	2.62	0.47	1.33	0.179	1.21	0.187	2.4	0.28	< 0.5	0.38	7	138	0.1	4.12	0.92
IG_BH03_LG011	17.3	30	2.99	10.3	1.75	0.476	1.32	0.17	0.82	0.14	0.36	0.05	0.33	0.048	2.9	0.67	< 0.5	0.33	8	34	< 0.1	5.15	1.14
IG_BH03_LG012	19.7	33.9	3.36	11.2	1.84	0.446	1.37	0.16	0.86	0.13	0.36	0.046	0.33	0.044	2.8	0.6	< 0.5	0.33	9	58	< 0.1	5.51	1.68
IG_BH03_LG013	19.8	34.7	3.5	12.2	2.08	0.627	1.43	0.19	0.99	0.16	0.43	0.063	0.4	0.057	3.7	0.45	< 0.5	0.23	6	73	< 0.1	4.3	1.15
IG_BH03_LG014	19.7	33.8	3.31	11.4	1.92	0.456	1.33	0.17	0.85	0.13	0.37	0.053	0.33	0.05	3.2	1.21	< 0.5	0.35	7	53	< 0.1	5.6	2.43
IG_BH03_LG015	4.42	9.85	1.14	4	1.32	0.065	1.83	0.4	2.58	0.49	1.41	0.203	1.28	0.177	2.8	1.97	< 0.5	0.81	16	7	< 0.1	2.55	12.9
IG_BH03_LG016	17.1	29.1	2.79	9.29	1.5	0.432	1.12	0.14	0.68	0.11	0.3	0.039	0.26	0.036	2.9	0.45	< 0.5	0.36	6	53	0.1	4.24	1.32
IG_BH03_LG017	18.4	33.8	3.27	11.5	2.02	0.545	1.39	0.18	0.85	0.13	0.33	0.043	0.3	0.049	3.2	0.74	< 0.5	0.11	< 5	22	< 0.1	5.96	1.61
IG_BH03_LG018	46	102	12.2	49.1	8.62	2.2	6.37	0.74	3.66	0.62	1.69	0.212	1.43	0.222	2.8	0.34	< 0.5	0.27	< 5	188	< 0.1	5.44	1.14
IG_BH03_LG019	20.9	36	3.54	12	1.93	0.491	1.46	0.17	0.83	0.14	0.4	0.052	0.32	0.046	3.3	0.77	< 0.5	0.19	< 5	41	< 0.1	5.39	1.84
IG_BH03_LG020	20	34.5	3.34	11.3	1.88	0.521	1.29	0.16	0.74	0.12	0.36	0.052	0.34	0.053	3.3	0.66	< 0.5	0.27	7	42	< 0.1	5.11	2.28
IG_BH03_LG021	22.7	41.5	4.24	15	2.59	0.806	2.02	0.25	1.19	0.2	0.52	0.07	0.41	0.065	4.2	0.67	1	0.18	< 5	63	< 0.1	5.13	1.29
IG_BH03_LG022	5.85	11.1	1.17	4.06	0.96	0.168	0.92	0.15	0.87	0.16	0.45	0.064	0.44	0.072	1.7	1.28	< 0.5	0.33	14	7	0.2	2.57	4.19

**Appendix C: Geophysical Near and Far
Density Log Correction**

The correction was determined by averaging the difference between each laboratory measurement and the field measurement at the corresponding Position, for the near and far density data sets. Eighteen laboratory core wet density measurements were considered. This correction was applied to the near and far density logs in WellCAD and the updated logs are exported from WellCAD and updated as .LAS files in the NWMO Acquire database.

Position along borehole	Near Density (ND)	Far Density (FD)	Lab Wet Density	Difference ND-Lab	Difference FD-lab	NDCorrection	FDCorrection
m	g/cm ³	g/cm ³	g/cm ³	g/cm ³	g/cm ³		
238.76	2.79	2.77	2.64	0.15	0.13	1.06	1.05
346	2.80	2.75	2.64	0.16	0.11	1.06	1.04
415.99	2.80	2.78	2.67	0.13	0.11	1.05	1.04
416.2	2.80	2.78	2.67	0.13	0.11	1.05	1.04
455.15	2.80	2.78	2.68	0.12	0.10	1.04	1.04
455.42	2.78	2.76	2.67	0.11	0.09	1.04	1.03
460.07	2.77	2.75	2.66	0.11	0.09	1.04	1.03
494.5	2.78	2.77	2.67	0.11	0.10	1.04	1.04
494.73	2.78	2.75	2.67	0.11	0.08	1.04	1.03
504.2	2.80	2.76	2.63	0.17	0.13	1.06	1.05
540.19	2.78	2.77	2.67	0.11	0.10	1.04	1.04
540.42	2.80	2.78	2.68	0.12	0.10	1.04	1.04
551.8	3.02	2.95	2.97	0.05	-0.02	1.02	0.99
552.67	2.98	2.90	2.99	-0.01	-0.09	1.00	0.97
554.71	2.80	2.78	2.64	0.16	0.14	1.06	1.05
582.55	2.80	2.75	2.68	0.12	0.07	1.05	1.03
582.82	2.80	2.77	2.68	0.12	0.09	1.04	1.04
608.59	2.77	2.77	2.66	0.11	0.11	1.04	1.04
662.59	2.79	2.78	2.68	0.11	0.10	1.04	1.04
662.81	2.79	2.73	2.68	0.11	0.05	1.04	1.02
665.85	2.82	2.78	2.65	0.17	0.13	1.06	1.05
771.84	2.79	2.81	2.65	0.14	0.16	1.05	1.06
880.09	2.79	2.77	2.66	0.13	0.11	1.05	1.04
984.96	2.77	2.75	2.66	0.11	0.09	1.04	1.03
				0.12	0.09	1.04	1.03

**Appendix D: Structure log integration
methodology**

Borehole IG_BH03 - Structure type and position-along-borehole verification, and the integration activity to define the azimuth of the arbitrary reference line.

Introduction

The orientation of all structures measured during core logging, as described in the WP03 Data Reports, are initially defined based on alpha and beta angles relative to (1) the core axis, and (2) an arbitrary reference line drawn along the length of each core run. Since the core was not oriented, these relative orientation angles (alpha/beta for planes; gamma/delta for lineations on planes), for each logged structure need to be corrected to a true orientation in order to produce the final structural log for IG_BH03.

A final structural log was produced by comparing the core logged structures and the televiewer logged structures. This appendix describes the methodology used to compare the structures from core and televiewer logging to (1) assess the nature of the structure type, (2) determine a correct location of the structure, and (3) identify the angle of each arbitrary reference line traced on each core run relative to low side (reference line correction factor, $\beta_{\text{correction}}$).

The process described in this appendix were the steps taken to develop a *final structure log* that included the final assignment of structure locations, positional discrepancies, structure type (e.g., vein, foliation, etc.), structure dip and dip direction and/or alpha and beta, and structure aperture.

Correction and verification Methodology

The following sections describe the steps to *correct* or *verify* individual structures recorded in core logging and televiewer logging activities, which were ultimately used to form the final structural log.

Structure Type and Positional Verification

Based on the integration between the two datasets, the structures were classified as being observed in 'both' datasets, in 'core logging only', or in 'televiewer only'. When a structure was observed in both datasets, the position along borehole and structure type recorded from core logging were used as the final structure position and final structure type. For structures only seen in the televiewer survey, a positional correction was applied based on the position-along-borehole offset calculated from the structures observed in both datasets. Positional corrections were applied to these structures in a way as to preserve structure order. Additional detail relating to the positional corrections applied to structures identified from the televiewer surveys is discussed in WP05 Data Report (Golder, 2020b).

At this stage, each individual structure that was common to both data sets was evaluated, and an integrated structure was carried forward to the *final structure log*. The integration of common structures was as follows:

- a) Location of the final structure was based on the position along borehole of the core logged structure;
- b) Dip and Dip direction of the final structure was based on the orientation of the televiewer logged structure (relative to *low side*);
- c) Structure type was assigned, based on the core logging;
- d) Other characteristics, such as mineral infilling, etc. was assigned based on core logging.

If a structure was identified only in the televiewer logs, core run photographs acquired during core logging were reviewed to aid in evaluating if this structure was present in the core. If it is determined that this is a real structure and not a drill feature, it was included in the final

structural log, along with its interpreted structure type, dip and dip direction, and corrected position along borehole.

If a structure was identified only in core logging, this structure was carried forward to the final structural log, along with its structure type, alpha and beta angles, and position along borehole.

Structure Orientation

For each core run logged in WP03, an arbitrary reference line was drawn along the length of the core, where the location is initially unknown. Orientations of all structures identified during core logging were described relative to this reference line (beta angles) in each run. The purpose of this section is to describe the process used to define the *true* location, from the 'low side' of the borehole, of this reference line (between 0 – 360°) by integrating the oriented televiewer images.

When a structure was observed in both datasets, the alpha and beta angles from the televiewer survey were used as the final structure orientation.

For structures only observed in core logging, a reference line correction factor was applied to the beta angles in order to locate the arbitrary reference line relative to the bottom of the borehole ('low-side'). The reference line correction factor relies on structures seen in both datasets within the same continuously referenced interval. The correction factor takes an average of the beta angle correction(s), which is the angle from the borehole 'low-side' (identified from the televiewer survey) to the arbitrary reference from core logging, calculated for each structure ($\beta_{\text{correction}} = \beta_{\text{televiewer}} - \beta_{\text{core logging}}$). Figure 1 shows how the beta angle correction relates to the arbitrary reference line and the borehole 'low-side'.

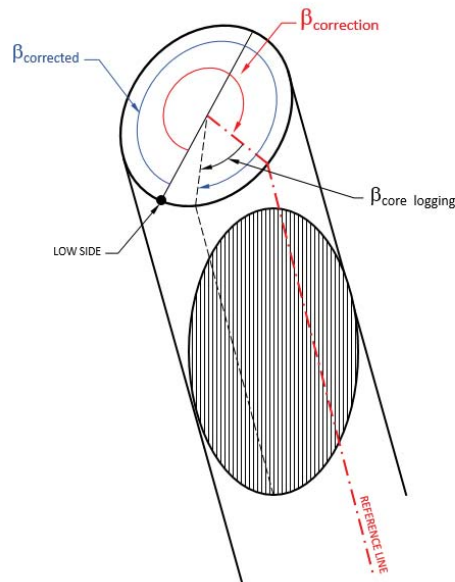


Figure 1: Schematic Showing Beta Angle Correction

$$\beta_{\text{core logging}} + \text{Reference Line Correction Factor(Average)} = \beta_{\text{corrected}}$$

(if $\beta_{\text{corrected}} > 360^\circ$, subtract 360°)

If no core logged structure within a continuously referenced interval was identified in the televiewer logs, then no reference line correction could be developed and orientation of the structure(s) within that interval was not possible.

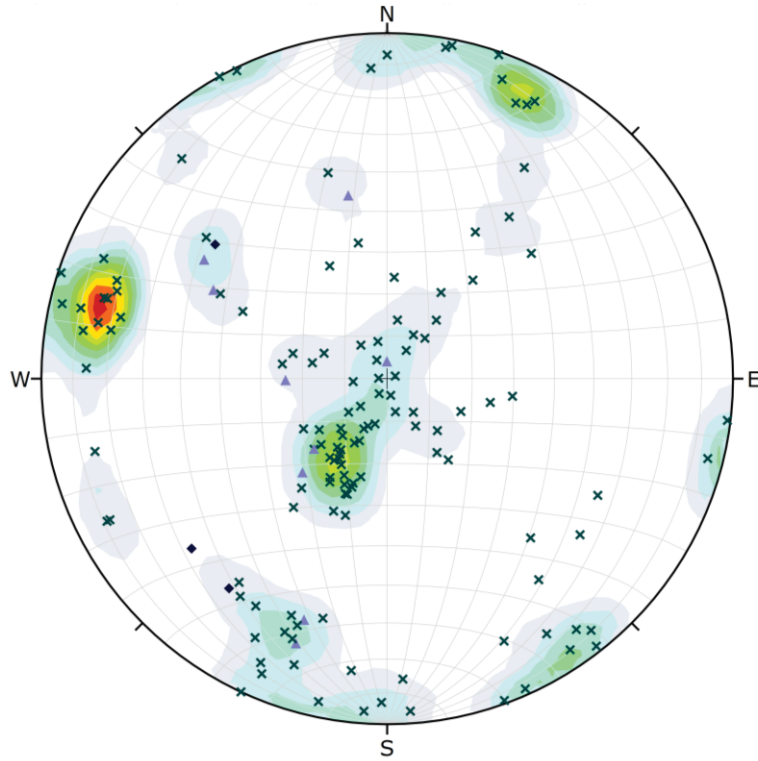
Dip and dip direction of the structures were calculated using the software DIPS© (Version 7), by Rocscience, which processes the data by using stereographic projections based on the alpha and corrected beta measurements and to the borehole deviation survey. The borehole survey file generated from the average of six separate televiewer probe runs using 1 m intervals between survey points was used for the projection of the final structure orientations.

Final Structural Log

The integration of core logged structures and televiewer logged structures resulted in a final structural log. The result of the final structural log includes a table that captures a complete set of attributes of each structure recorded either from core logging, televiewer logging, or a combination of both. Where certain attributes are duplicated between the two logging approaches (i.e., structure type, or position along borehole) decisions were made to carry forward the most accurate value to the final structure log. For example, positional values and structure type were obtained from the core logging structures.

**Appendix E: Stereonets of Fractures by
Structural Unit**

SU1 (0 – 51.0 m)



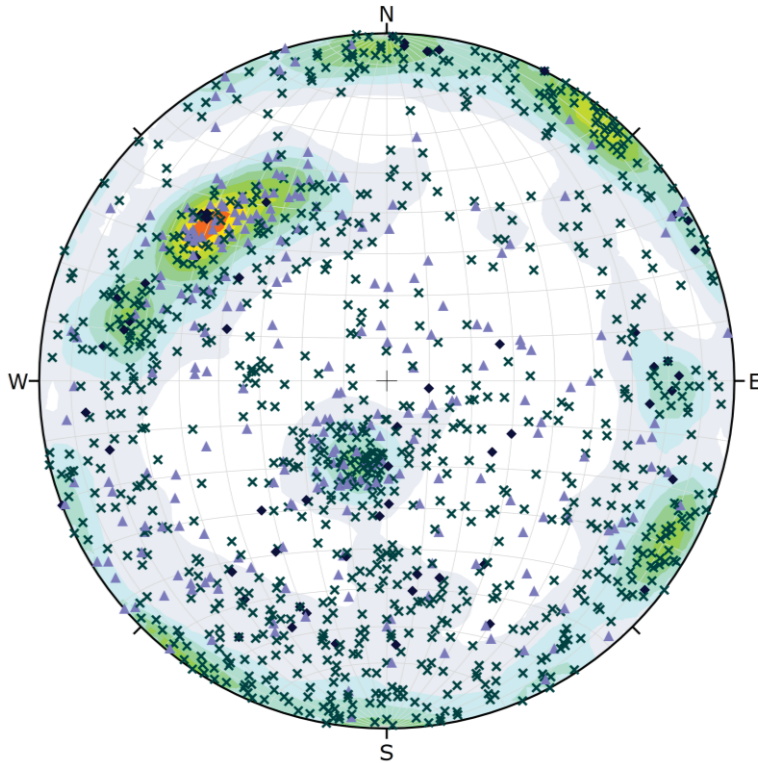
Symbol	STR_TYPE	Quantity
◆	FLT	3
×	JN	134
▲	VN	9

Color	Density Concentrations
	0.00 - 1.10
	1.10 - 2.20
	2.20 - 3.30
	3.30 - 4.40
	4.40 - 5.50
	5.50 - 6.60
	6.60 - 7.70
	7.70 - 8.80
	8.80 - 9.90
	9.90 - 11.00

Contour Data	Pole Vectors
Maximum Density	10.55%
Contour Distribution	Fisher
Counting Circle Size	1.0%

Plot Mode	Pole Vectors
Vector Count (Weighted)	284 (146 Entries)
Terzaghi Weighting	Minimum Bias Angle 15°
Hemisphere	Lower
Projection	Equal Area

SU2 (51.0 – 860.5 m)



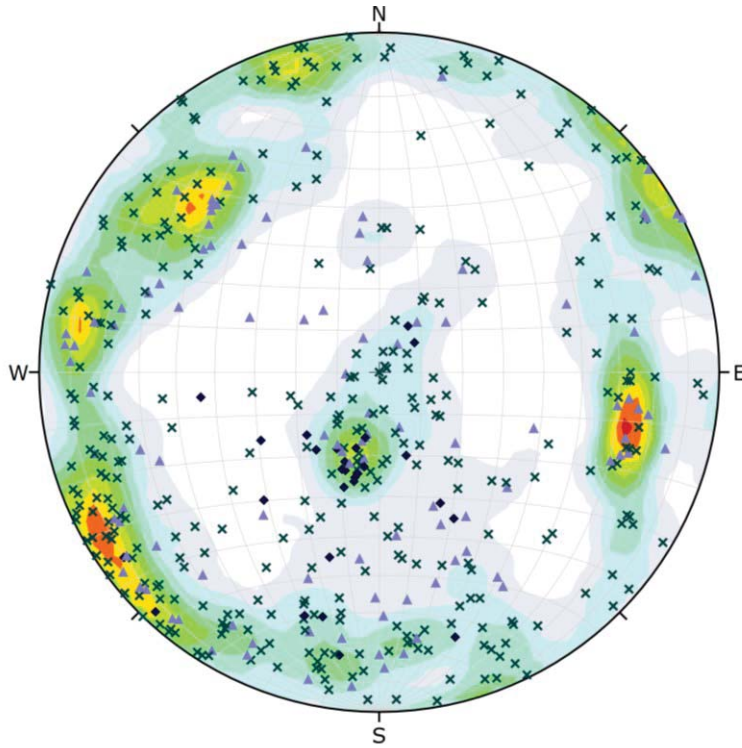
Symbol	STR_TYPE	Quantity
◆	FLT	58
×	JN	921
▲	VN	276

Color	Density Concentrations
	0.00 - 0.60
	0.60 - 1.20
	1.20 - 1.80
	1.80 - 2.40
	2.40 - 3.00
	3.00 - 3.60
	3.60 - 4.20
	4.20 - 4.80
	4.80 - 5.40
	5.40 - 6.00

Contour Data	Pole Vectors
Maximum Density	5.32%
Contour Distribution	Fisher
Counting Circle Size	1.0%

Plot Mode	Pole Vectors
Vector Count (Weighted)	2823 (1255 Entries)
Terzaghi Weighting	Minimum Bias Angle 15°
Hemisphere	Lower
Projection	Equal Area

SU3 (860.5 – 1000.54 m)



Symbol	STR_TYPE	Quantity
◆	FLT	29
×	JN	333
▲	VN	113

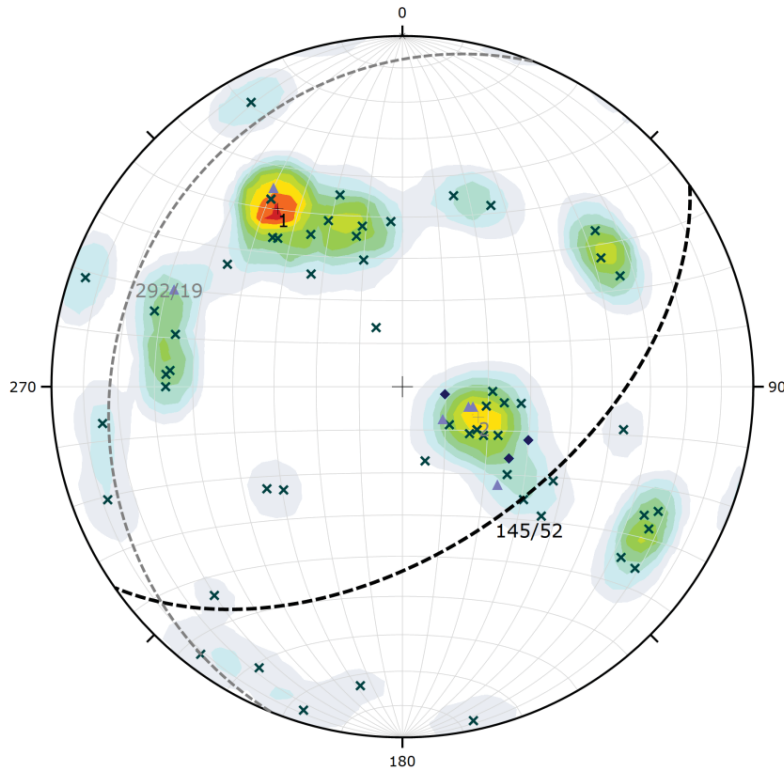
Color	Density Concentrations
	0.00 - 0.45
	0.45 - 0.90
	0.90 - 1.35
	1.35 - 1.80
	1.80 - 2.25
	2.25 - 2.70
	2.70 - 3.15
	3.15 - 3.60
	3.60 - 4.05
	4.05 - 4.50

Contour Data	Pole Vectors
Maximum Density	4.26%
Contour Distribution	Fisher
Counting Circle Size	1.0%

Plot Mode	Pole Vectors
Vector Count (Weighted)	999 (475 Entries)
Terzaghi Weighting	Minimum Bias Angle 15°
Hemisphere	Lower
Projection	Equal Area

**Appendix F: Stereonets of IG_BH03
High Fracture Frequency Intervals
(HFFI)**

IG_BH03 HFFI_1 (142.3 – 157.7 m):



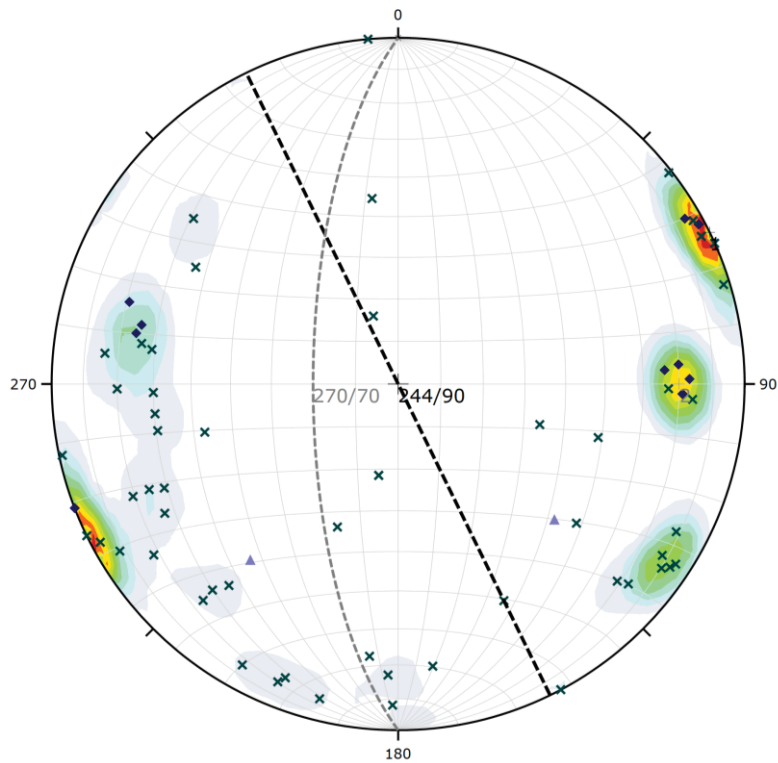
Symbol	STR_TYPE	Quantity
◆	FLT	3
×	JN	57
▲	VN	6

Color	Density Concentrations
	0.00 - 1.10
	1.10 - 2.20
	2.20 - 3.30
	3.30 - 4.40
	4.40 - 5.50
	5.50 - 6.60
	6.60 - 7.70
	7.70 - 8.80
	8.80 - 9.90
	9.90 - 11.00

Contour Data	Pole Vectors
Maximum Density	10.24%
Contour Distribution	Fisher
Counting Circle Size	1.0%

Plot Mode	Pole Vectors
Vector Count (Weighted)	131 (66 Entries)
Terzaghi Weighting	Minimum Bias Angle 15°
Hemisphere	Lower
Projection	Equal Area

IG_BH03 HFFI_2 (400.83 – 416.5 m):



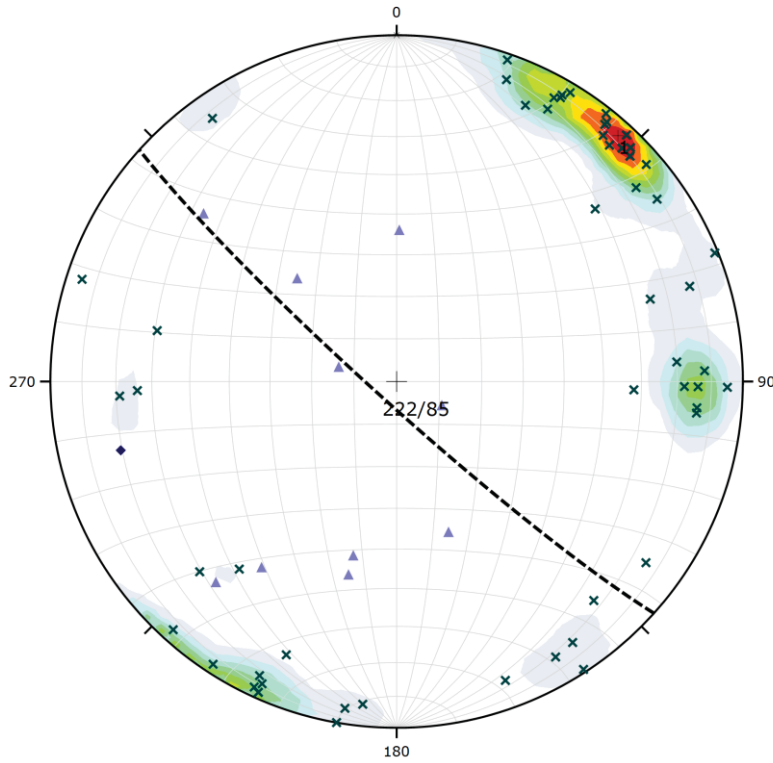
Symbol	STR_TYPE	Quantity
◆	FLT	11
×	JN	55
▲	VN	2

Color	Density Concentrations
	0.00 - 1.80
	1.80 - 3.60
	3.60 - 5.40
	5.40 - 7.20
	7.20 - 9.00
	9.00 - 10.80
	10.80 - 12.60
	12.60 - 14.40
	14.40 - 16.20
	16.20 - 18.00

Contour Data	Pole Vectors
Maximum Density	17.07%
Contour Distribution	Fisher
Counting Circle Size	1.0%

Plot Mode	Pole Vectors
Vector Count (Weighted)	175 (68 Entries)
Terzaghi Weighting	Minimum Bias Angle 15°
Hemisphere	Lower
Projection	Equal Area

IG_BH03 HFFI_3 (476.75 – 494.58 m):



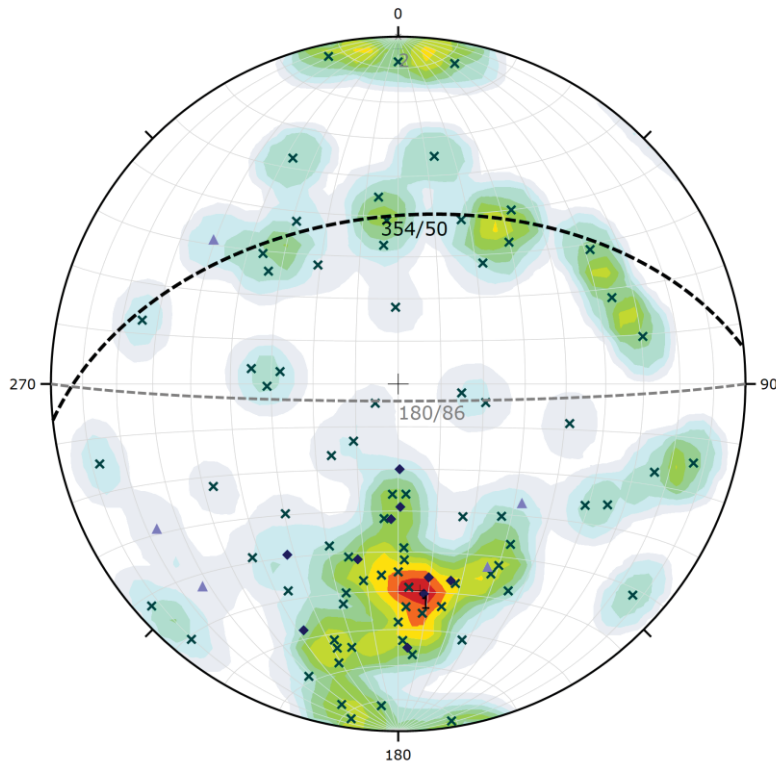
Symbol	STR_TYPE	Quantity
◆	FLT	1
×	JN	58
▲	VN	10

Color	Density Concentrations
	0.00 - 2.00
	2.00 - 4.00
	4.00 - 6.00
	6.00 - 8.00
	8.00 - 10.00
	10.00 - 12.00
	12.00 - 14.00
	14.00 - 16.00
	16.00 - 18.00
	18.00 - 20.00

Contour Data	Pole Vectors
Maximum Density	19.59%
Contour Distribution	Fisher
Counting Circle Size	1.0%

Plot Mode	Pole Vectors
Vector Count (Weighted)	199 (69 Entries)
Terzaghi Weighting	Minimum Bias Angle 15°
Hemisphere	Lower
Projection	Equal Area

IG_BH03 HFFI_4 (764.33 – 781.6 m):



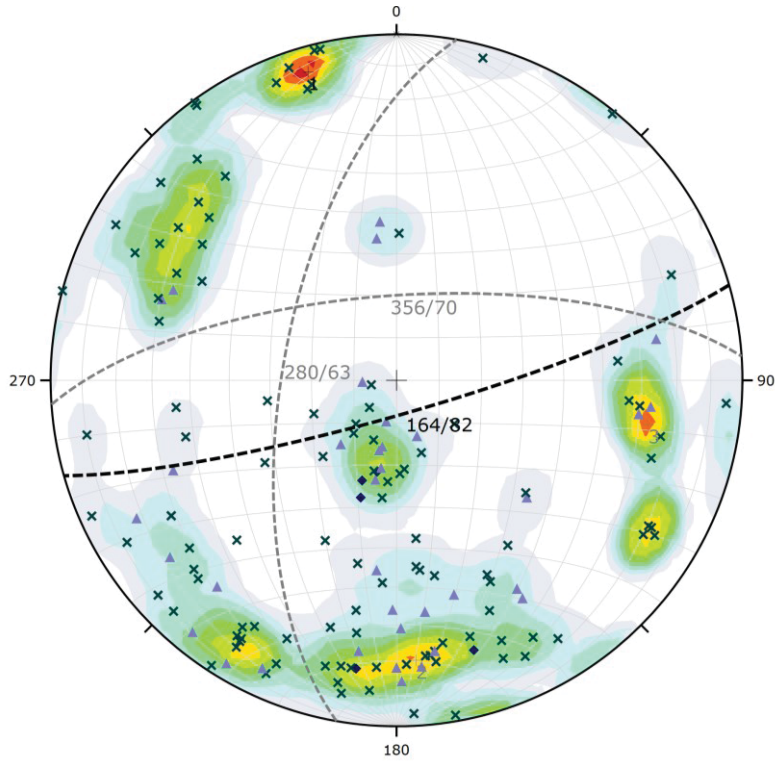
Symbol	STR_TYPE	Quantity
◆	FLT	10
×	JN	78
▲	VN	5

Color	Density Concentrations
	0.00 - 0.60
	0.60 - 1.20
	1.20 - 1.80
	1.80 - 2.40
	2.40 - 3.00
	3.00 - 3.60
	3.60 - 4.20
	4.20 - 4.80
	4.80 - 5.40
	5.40 - 6.00

Contour Data	Pole Vectors
Maximum Density	5.90%
Contour Distribution	Fisher
Counting Circle Size	1.0%

Plot Mode	Pole Vectors
Vector Count (Weighted)	161 (93 Entries)
Terzaghi Weighting	Minimum Bias Angle 15°
Hemisphere	Lower
Projection	Equal Area

IG_BH03 HFFI_5 (860 – 882.5 m):



Symbol	STR_TYPE	Quantity
◆	FLT	5
×	JN	112
▲	VN	35

Color	Density Concentrations
	0.00 - 0.65
	0.65 - 1.30
	1.30 - 1.95
	1.95 - 2.60
	2.60 - 3.25
	3.25 - 3.90
	3.90 - 4.55
	4.55 - 5.20
	5.20 - 5.85
	5.85 - 6.50

Contour Data	Pole Vectors
Maximum Density	6.16%
Contour Distribution	Fisher
Counting Circle Size	1.0%

Plot Mode	Pole Vectors
Vector Count (Weighted)	293 (152 Entries)
Terzaghi Weighting	Minimum Bias Angle 15°
Hemisphere	Lower
Projection	Equal Area

**Appendix G: Summary of borehole logs
at 1:1,000 scale**

